EXTRACTION OF THE SECOND-ORDER NONLINEAR RESPONSE FROM MODEL TEST DATA IN RANDOM SEAS AND COMPARISON OF THE GAUSSIAN AND NON-GAUSSIAN MODELS

A Dissertation

by

NUNGSOO KIM

Submitted to the Office of Graduate Studies of
Texas A&M University
in partial fulfillment of the requirements for the degree of

DOCTOR OF PHILOSOPHY

December 2004

Major Subject: Ocean Engineering

EXTRACTION OF THE SECOND-ORDER NONLINEAR RESPONSE FROM MODEL TEST DATA IN RANDOM SEAS AND COMPARISON OF THE GAUSSIAN AND NON-GAUSSIAN MODELS

A Dissertation

by

NUNGSOO KIM

Submitted to Texas A&M University
in partial fulfillment of the requirements
for the degree of

DOCTOR OF PHILOSOPHY

Approved as to style and content by:

Cheung Hun Kim
(Chair of Committee)

Edward J. Powers
(Member)

H. Joseph Newton
(Member)

Moo-Hyun Kim
(Member)

Paul N. Roschke
(Head of Department)

December 2004

Major Subject: Ocean Engineering

ABSTRACT

Extraction of the Second-Order Nonlinear Response
from Model Test Data in Random Seas and
Comparison of the Gaussian and non-Gaussian Models.
(December 2004)

Nungsoo Kim, B.S., Inha University, Korea;
M.S., Inha University
Chair of Advisory Committee: Dr. Cheung Hun Kim

This study presents the results of an extraction of the 2nd-order nonlinear responses from model test data. Emphasis is given on the effects of assumptions made for the Gaussian and non-Gaussian input on the estimation of the 2nd-order response, employing the quadratic Volterra model.

The effects of sea severity and data length on the estimation of response are also investigated at the same time. The data sets used in this study are surge forces on a fixed barge, a surge motion of a compliant mini TLP (Tension Leg Platform), and surge forces on a fixed and truncated column. Sea states are used from rough sea (Hs=3m) to high sea (Hs=9m) for a barge case, very rough sea (Hs=3.9m) for a mini TLP, and phenomenal sea (Hs=15m) for a truncated column.

After the estimation of the response functions, the outputs are reconstructed and the 2nd order nonlinear responses are extracted with all the QTF distributed in the entire bi-frequency domain. The reconstituted time series are compared with the experiment in both the time and frequency domains.

For the effects of data length on the estimation of the response functions, 3, 15, and 40-hour data were investigated for a barge, but 3-hour data was used for a mini TLP and a fixed and truncated column due to lack of long data.

The effects of sea severity on the estimation of the response functions are found in both methods. The non-Gaussian method for estimation is more affected by data length than the Gaussian method.

In memory of my grandparents

Pyungkook Kim and Oksun Kim

ACKNOWLEDGMENTS

I would like to express special thanks to my advisor Dr. Cheung Hun Kim for the guidance, inspiration, assistance and supervision he has shown during my whole study. I also would like to thank Dr. Edward J. Powers, Dr. Moo-Hyun Kim, and Dr. H. Joseph Newton for their helpful advice and willingness to serve on my advisory committee. I am grateful to Dr. Yngve Birkelund for invaluable comments. I offer my thanks to all the other faculty members and students in the ocean engineering program for being good friends. I also would like to acknowledge the sharing of data from the Offshore Technology Research Center and MARINTEK.

I would like to express my appreciation to my parents, Kwang-Ho Kim and Jungsook Moon for their love, sacrifice, and constant support throughout my life. I also would like to thank my brother, Nung-yil Kim and my sister, Ae-Jin Kim.

TABLE OF CONTENTS

CHAPTER Page

LIST OF FIGURES

FIGURE Page

LIST OF TABLES

TABLE Page

CHAPTER I

INTRODUCTION

1. 1 Background

Until now, regular waves have been applied to many researches on the response of offshore structure both in experiment and numerical simulation. The numerical wave tank (NWT) is usually limited to use regular waves of single or sum of two frequencies based on the linear potential theory.

It has been realized that more advanced studies are needed to simulate the realistic ocean waves, and that the physical modeling of a random sea in an experimental wave tank and measuring the random responses of offshore systems are required. Thus, the modeling technique to analyze experimental data with the input-output concept will be employed in this study. This technique is also called the system identification which makes it possible to deal with many effective frequencies.

The conventional approach is to estimate only the linear transfer function from the measured random waves and responses. However, researches have been carried out to investigate the nonlinear effects on the response of offshore structures. Among these effects, the 2^{nd}-order effects are known to be significant in designing offshore structures today. The nonlinear system is usually approximated to the 2^{nd}-order. Prior to the experimental works, a lot of theoretical studies on the 2^{nd}-order effects are usually carried out, while experimental verifications of the 2^{nd}-order theory are rarely conducted though the experimental work is essential to improve theory. This may be due to difficulties in securing the accuracy in the experiment and in estimating of the quadratic transfer function from the experimental work.

In this experimental work, the quadratic Volterra model (**Fig. 1.1** and **Fig. 1.2**) will be considered for the entire marine system. It represents the 2^{nd}-order marine systems; the 2^{nd}-order wave, the 2^{nd}-order wave force as well as the 2^{nd}-order response motion. The use of the model makes it possible to determine the 2^{nd}-order transfer functions. For the estimation of the quadratic transfer function, the Volterra quadratic model will be employed with two different methods: the Gaussian and the non-Gaussian input methods.

This dissertation follows the style and format of *International Journal of Offshore and Polar Engineering*.

In addition, the effects of sea severity and data length are included.

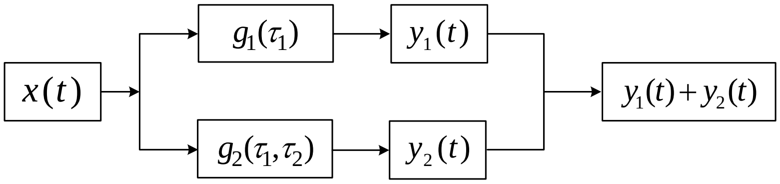

Fig. 1.1 Quadratic Volterra model in time domain

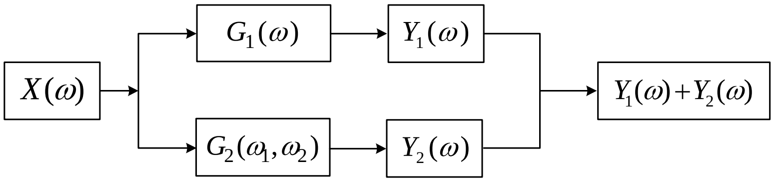

Fig. 1.2 Quadratic Volterra model in frequency domain

1.2 Literature review

The quadratic nonlinear system was mathematically described by the Volterra functional polynomial, the application of which was first suggested by Tick (1961). The Volterra functional series approach to nonlinear system analysis is very general. The broad and leading idea for the investigation of QTF for the offshore structures was done by Hasselmann (1966). He proposed a quadratic input-output model for determining QTF characterizing the nonlinear response of ship motion in short-crested random seas and suggested the need of conducting the experimental (full-scale measurements) and theoretical works (the coefficients, QTF) for the lateral drift motion of the ship in random seaways. In the same period, Vassilopoulos (1966) outlined essentially the same approach to quadratic random processes and demonstrated that the added resistance problem may be treated as a quadratic process.

One of the leading researchers in the field is Dalzell, whose works on the problem span over his entire life. He modified the cross-bispectrum by Tick (1961) and developed the algorithm for the estimation of the quadratic frequency response function of added resistance for a ship in long-crested random seas (Dalzell, 1972). Dalzell (1974) did a detailed analysis with experimental data and concluded that the mean added resistance operator could be identified from irregular wave data but the data length should have to be 10-12 times longer than those required in linear sea-keeping problems in order to obtain comparable accuracy. Dalzell (1976) also extensively demonstrated the applicability of time domain drift force simulation using quadratic impulse response function. Dalzell and Kim (1979) hydrodynamically computed the modified cross-bispectrum (CBS) and QTF for the 2^{nd}-order added ship resistance and found that analytical and experimental estimates of the cross- bispectrum were in fair agreement. However, the estimated cross-bispectrum for more severe sea (Hs=11m) behaves inconsistently compared with the hydrodynamic computation. Krafft and Kim (1990, 1992) investigated the bi-frequency quadratic frequency response functions for the slow drift motion of a soft moored barge in dual waves and compared numerical predictions based on the Volterra quadratic model and linear diffraction theory.

The above works are based on the assumption that the input random wave is Gaussian. The Gaussian assumption is acceptable if the sea severity is low, (Hs=4m), but it will be beyond the 2^{nd}-order nonlinearity, if the sea is high such as Hs=11 m, according to Kumar et al. (2002).

Kim and Powers (1988) found that Gaussian assumption of the input leads to highly biased erroneous estimates. They investigated the Volterra quadratic model with the assumption of the non-Gaussian input and validated the model using a mathematical and strong non-Gaussian input. Kim and Powers (1992, 1995) developed a new orthogonal approach for the estimation of the Volterra kernel which removes nonlinear interference terms associated with the non-Gaussian waves. The above research was further studied, and the recent contribution by Birkelund et al. (2003) improved the original algorithm by applying the combined use of the multi-taper and principal component analysis (PCA).

Stansberg (2001) developed a procedure for determining the reconstructed 2^{nd}-order nonlinear low frequency response by comparing with theoretical values. Kim and Kim (2002), in order to investigate the extraction of QTF, used the theoretical 2^{nd}-order long-crested sea wave (Dean and Sharma, 1981) as input and simulated the corresponding 2^{nd}-order random force time series on a barge fixed in the waves as the output. In the foregoing study, they estimated the modified CBS with the various sea severity (Hs=3m to 12 m). However, the effects of sea severity were not clearly detected, and they found that this was attributed to the fact that the simulated 2^{nd}-order waves were theoretical waves, which are less severe than the real waves in a wave tank. This finding motivated them to realize the importance of experiments for real 2^{nd}-order or higher waves. Kim and Kim (2003) further studied the same work by extending the previous study to conducting a model test in a wave tank and investigating the effect of data length on the estimation of CBS as Dalzell (1976) mentioned the data length.

So far, some researches have dealt with nonlinear waves and their corresponding responses in conjunction with statistical views. Concerning the effect of the data length, Kim and Boo (1990) numerically investigated the behavior of the mean lateral drift force on the ship in beam seas as a function of duration. They found that it takes about 15 hours to converge. In the simulation, they apply the un-repeating random sea digital data obtained from the linear filtering of white noise. Stansberg (1992, 2001) discussed the statistical behavior of slow drift and mooring line tension and concluded that an 18-hour storm simulation gives better results than a statistically scattered 3-hour simulation. The effect of data length is also considered to be important for the region outside the low frequency. Matsui (1992) compared the simulated 2nd-order diffraction forces on floating bodies with experiments in the limited number of frequencies.

Statistics of structure response are also important in the examination of the effect of sea severity. Hineno (1984) calculated the distribution of the extreme relative motion of a semi-submersible platform and compared the results with experimental results by applying a frequency domain method proposed by Vinje (1976). Naess (1985) developed a theoretical and asymptotic method for estimating the response statistics of an ocean structure assuming the 2nd-order dynamic system subjected to a stationary Gaussian sea and a quadratic Volterra model. Particularly, the prediction of extreme response was emphasized by using the concept of mean zero-upcrossing frequency.

Recently, Kim and Kim (2004) applied the Gaussian and non-Gaussian method for the QTF of the wave forces on a barge fixed in random waves, investigating the effects of the method on the sea severity and record length.

Table 1.1 presents additional details in chronological order about the technical papers referenced in this literature review of major contribution.

Table 1.1 Literature review of major contribution

Author(s)	Date	Title	Summary
Tick	1961	The Estimation of Transfer Functions of Quadratic Systems	This paper outlined a model for a quadratic random process and a simplified bispectrum analysis technique, which appeared to be bear directly on the added resistance problem. The spectral techniques of transfer function estimation of linear systems were extended to time invariant quadratic systems when a stationary Gaussian process is used as a driving function.
Hasselmann	1966	On Non-Linear ship Motions in Irregular Waves	It is shown that the transfer functions characterizing the nonlinear response of ships of ships in irregular seas can be obtained form high order moments of the ship motions by an extension of standard spectral analysis techniques. This paper recommended full-scale measurements can be used to determine, for example, the coefficients (QTF) of added ship wave resistance and lateral drift of ship.
Vassilopouos	1966	The Application of Statistical theory of Non-Linear Systems to Ship Motion Performance in Random Seas	This paper approached to random processes with a quadratic input-output model and demonstrated that the added resistance problem may be treated as a quadratic process
Dalzell	1976	Application of the Functional Polynomial Model to the Ship Added Resistance Problem	Cross-bispectral analysis methods were developed and applied to the derivation of or ”identification” of the “added resistance operator” from data obtained in irregular waves.
Dalzell and C.H.Kim	1979	An Analysis of the Quadratic Frequency Response for Added Resistance	This paper computed hydrodynamically the cross-bi-spectrum for the 2nd order added ship resistance on the basis of the assumption of the Gaussian input and demonstrated that analytical and experimental estimates of the cross-bi-spectrum are in good qualitative agreement, and in fairly quantitative agreement.
K. I. Kim and Powers	1988	A Digital Method of Modeling Quadratically Nonlinear Systems with a General Random Input	This research developed a matrix approach to estimate linear and quadratic frequency domain Volterra Kernels which is valid for general (i.e. non-Gaussian as well as Gaussian) random inputs.
C.H. Kim and S.Y. Boo	1990	Statistical Analysis of Slow Drift Forces in Random Seas	Numerical simulation was conducted to investigate the variation of mean drift force in time pseudo-random sea. It appears that the mean force converges to constant value after 15 hours.
Krafft, M.J. and Kim C.H.	1990	Experimental investigation of quadratic frequency response function for slow drift motion in bi-frequency domain	The results of experimental measurements of the slowly varying surge motion of a soft moored rectangular barge in the bi-frequency domain are compared to numerical predictions based on a Volterra model and linear diffraction theory.

Table 1.1 Continued

Author(s)	Date	Title	Summary
Krafft, M.J. and Kim C.H.	1992	Surge Drift Motion of a Moored Vessel in Random Waves	Experimental measurements of the surge drift motion of a soft moored barge in random waves are compared to a numerical simulation employing a complete quadratic frequency response function for surge motion, based on a Volterra theory and experimentally determined bi-frequency wave drift damping coefficients.
S. B. Kim and Powers	1992	Identification of Quadratic Drift Response of TLP's Using Conditioned Orthogonal QFRF's	This paper presented a new orthogonal approach for the estimation of nonlinear FRF's which is valid for general random waves (i.e. non-Gaussian as well as Gaussian), while at the same time removing the presence of the interference terms associated with non-Gaussian waves. This approach is applied to quantify the linear and dynamic quadratic nonlinear response of TLP's to non-Gaussian sea wave excitation.
Stansberg	1992	On the Estimation of Extreme Mooring Line Forces	The statistical behavior of slow drift and the mooring line tension was discussed, and it was conclude that an 18-hour storm simulation gives better results than a statistically scattered 3-hour simulation.
Stansberg	2001	Data Interpretation and System Identification in Hydrodynamic Model Testing	The cross-bispectral analysis for the estimation of quadratic transfer functions was employed to analyze the laboratory data sets, and the 2nd-order low frequency response was reconstructed and compared with theory values. This work also mentioned the statistical uncertainty of a 3-hour random realization.
N.S. Kim and C.H. Kim	2002	Cross Bi Spectral Estimate of Nonlinear Force on Fixed Structure in Nonlinear Waves	The 2nd order random waves and surge forces on the fixed barge were simulated to be used as input and output (Hs=3m to 12m). These data were used for the cross spectral and cross bi spectral estimates form which the system characteristics LTF and QTF were determined. They found that the effect of sea severity was not clearly detected because of limitation on the simulated 2dn order random waves.
Birkelund et al	2003	On the Estimation of Nonlinear Volterra Models in Offshore Engineering	They further improved original algorithm applying the combined use of multi-taper and PCA and applied this method to a compliant Mini TLP to compute higher order spectral estimators for surge response motion.
N.S Kim and C.H. Kim	2003	The Effect of Sea Severity on the Cross Bi Spectral Estimate of Quadratic Response Function for Surge Exciting Forces	This paper investigated the effect of sea severity Hs=3m to 9m using measured data in the wave tank by previous way (2002). They reconstructed the wave forces time series as a system identification tool and compared with measured wave forces, It is found that the effect of the sea severity on the cross and cross-bi-spectral estimates.
N.S Kim and C.H. Kim	2004	Gaussian- and Non-Gaussian Input Method for Extraction of QTFs from Test Data of Offshore Structures	The Gaussian and non-Gaussian methods were applied for the QTF of the wave forces on a barge fixed in random waves. The effects of sea severity and data length on the estimation of response were also investigated together with the study of effects of Gaussian and non-Gaussian assumptions.

CHAPTER II

OBJECTIVE

The objective of this research is to extract the 2nd-order nonlinear responses from model test data and to represent the extracted responses in the time domain, employing the quadratic Volterra model with the Gaussian and non-Gaussian input assumption.

The second objective is to investigate the effects of the sea severity on the estimation of the response function. It was envisioned that the accuracy in the estimation of quadratic transfer function may be improved by using lower sea severity.

The third objective is to examine the effects of the data length on the estimation of the response function. Usually, most data measured in wave basins are 3-hour long. Much longer record length was suggested by researches in the area.

2.1. Effects of data length on estimation of system

An adequate record length necessary to evaluate the statistics in conducting the model test in a wave tank has been questioned for quite sometime. The proposed length of time is 6 hours (Dalzell, 1976) and 3 hours in other literature. Dalzell (1976) found a couple of factors which affect the cross-bispectrum (CBS) of the added wave resistance. He suggested the data length to be long enough to estimate CBS of the added wave resistance. Kim and Boo (1990) simulated the numerical lateral drift force of a series-60 ship model in the random beam seas of Hs=5.5m by using the quadratic impulse response function, converting the low-difference frequency in the QTF and the random (unrepeating) sea digital data obtained from the linear filtering of white noise. They investigated the behavior of the mean lateral drift force on a ship as a function of time duration. This research found that the convergence was tested by applying the accumulative moving average to the drift force time series that is shown in **Fig. 2.1**. The mean drift force starts to converge after a 15-hour lapse, which is much longer than the proposed record lengths in literature.

Stansberg (1992, 2001) discussed the statistical behavior of slow drift and mooring line tension and concluded that an 18-hour storm simulation gives better result than a statistically scattered 3-hour simulation. He proposed that quite long recording data lengths may be necessary for accurate estimation. The effect of data length is also considered to be important for the region outside the low frequency.

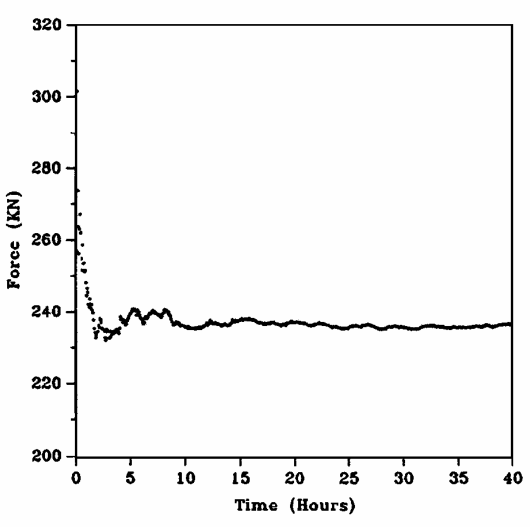

Fig. 2.1 The variation of mean drift force as function of time.

2.2. Effects of sea severity on estimation of system

2.2.1. Classification of sea state

Waves generated by a local wind or storms are called wind-generated seas. The wind-generated sea state is usually classified by code 0 to 9, (Tupper, 1996) as listed in **Table 2.1**, which represents the sea state or sea severity in terms of the significant wave height.

Table 2.1 Classification of different sea-states based on the significant wave height

Code	Description of Sea	Hs (m)
0	Calm (glassy)	0.00
1	Calm (rippled)	0.00 – 0.10
2	Smooth (wavelets)	0.10 – 0.50
3	Slight	0.50 – 1.25
4	Moderate	1.25 – 2.50
5	Rough	2.50 – 4.00
6	Very Rough	4.00 – 6.00
7	High	6.00 – 9.00
8	Very High	9.00 –14.00
9	Phenomenal	Over 14.00

2.2.2. Gaussian and non-Gaussian waves

A long-crested linear random wave, or Gaussian wave of about zero mean is represented in Eq. (2.1)

$$\eta(t) = \sum_{i=1}^{\infty} A_i \cos(k_i x - \omega_i t + \varepsilon_i) \qquad (2.1)$$

The linear-random wave profile is statistically symmetric about the mean water level (MWL) of the sea surface. If the measured or theoretical wave profile is statistically "asymmetric," it is nonlinear random waves, or non-Gaussian waves. One may digitally simulate a Gaussian wave from a target energy density spectrum. However, the real waves generated in the wave tank using the same target spectrum are most likely non-Gaussian if the sea state is more than the rough sea. It should be noted that the digitally simulated random wave from the wave energy density spectrum is always Gaussian, regardless of the size of the significant wave height.

The laboratory random wave is always nonlinear and non-Gaussian. The degree of nonlinearity depends on the sea severity, Hs, of the target spectrum used for the generation of the wave. The laboratory random waves may be regarded approximately Gaussian if the Hs is less than 4 m, or approximately 2nd-order when the Hs is less than 9 m. If Hs is higher than 9 m, the nonlinearity will be higher than the 2nd-order as discussed in Kumar and Kim (2002).

2.2.3. Effects of sea severity on LTF and QTF

Given input and output data, one can estimate the LTF and QTF of the system by estimating the cross-spectrum and cross-bispectrum, which may use either the Gaussian or non-Gaussian-input method motioned in Dalzell (1976) and Kim and Powers (1987), respectively. Kim and Kim, (2003, 2004) conducted a model test by measuring the forces on a barge fixed in random waves. Kim and Kim (2004) applied the Gaussian and non-Gaussian method for the QTF of the wave forces to find out the effects of the method on the sea severity and record length.

In chapter 4, we will examine the effect of data length and sea severity on the system characteristics (LTF and QTF) at various sea states with different systems (a fixed barge, a compliant Mini TLP, a fixed and truncated column) by employing the Gaussian and non-Gaussian methods.

CHAPTER III

MATHEMATICAL FORMULATION

There are two kinds of estimations; the Gaussian assumption (Dalzell, 1976) and non-Gaussian input assumptions (Kim and Powers, 1988). The general Volterra model and Volterra quadratic model will be reviewed, and the two different methods will be introduced in this chapter.

3.1. Volterra model

3.1.1. Volterra Functional polynomial in time domain

The Volterra functional polynomial Eq. (3.1) may be interpreted as mathematical model to interlink the relation between the input and output. The Volterra model is essentially a functional series in that the nonlinear output is expressed by sum of the linear, quadratic, and higher order response.

For present purpose it is reasonable to assume that the input, *x*(*t*) is a zero mean function whether it is random or deterministic. It is assumed that *y*(*t*) is a sufficiently regular function that it may at least be expanded in an infinite functional series (Barrett, 1963):

$$\begin{aligned} y(t) &= \sum_{n=0}^{\infty} \int \cdots \int g_n(t_1, t_2, \cdots, t_n)\, x(t-t_1) \cdots x(t-t_2)\, dt_1 \cdots dt_n \\ &= g_0 + \int g_1(t_1)\, x(t-t_1)\, dt_1 + \int \cdots \int g_n(t_1, t_2, \cdots, t_n)\, x(t-t_1) \cdots x(t-t_2)\, dt_1 \cdots dt_n \end{aligned} \tag{3.1}$$

(Omission of limits on integral hereafter signify of $-\infty$ and $+\infty$)

$x(t) =$ input
$y(t) =$ output
$g_0 =$ a static value not related to input
$g_1(t_1) =$ linear impulse response function
$g_2(t_1,t_2) =$ quadratic impulse response function
$g_3(t_1,t_2,t_3) =$ cubic impulse response function
: :
$g_n(t_1,t_2,\cdots,t_n) =$ n^{th} impulse response function

Each term in the series Eq. (3.1) is a homogeneous functional of degree n. the terms are said to be homogeneous because a change in $x(t)$ to $Cx(t)$ results in multiplication of the term of degree n by c^n.

The kernel, $g_n(t_1,t_2,\cdots,t_n)$, is time invariant, since it is considered to be functional only of time differences. In the present application, the input to system varies with time, but not the system of interest. Consequently, the prosperities of the system are contained wholly within the kernels. Barrett (1963) indicates that the series expansion is unique if all kernels are completely symmetrical in the variables; that is

$$g_n\left(t_1,t_2,t_3,\cdots,t_n\right)=g_n\left(t_2,t_3,\cdots,t_n,t_1\right) \tag{3.2}$$

for any rearrangement of the variables t_j without loss of generality from this restriction.

3.1.2. Volterra Functional polynomial in frequency domain

If Eq. (3.1) is Fourier transformed term by term, an equivalent frequency domain model is obtained by

$$\begin{aligned} Y(f)=&G_0+\int G_1(f_1)X(f-f_1)df_1+\cdots \\ &+\int\cdots\int G_n(f_1,f_2,\cdots,f_n)X(f-f_1)\cdots X(f-f_2)df_1\cdots df_n \end{aligned} \tag{3.3}$$

or

$$\begin{aligned} Y\left(\omega\right)=&G_0+\int G_1\left(\omega_1\right)X\left(\omega-\omega_1\right)df_1+\cdots \\ &+\int\cdots\int G_n\left(\omega_1,\omega_2,\cdots,\omega_n\right)X(\omega-\omega_1)\cdots X(\omega-\omega_2)d\omega_1\cdots d\omega_n \end{aligned} \tag{3.4}$$

,where $X(f)$, $Y(f)$ denote the Fourier transform of $x(t)$, $y(t)$ respectively. G_0, $G_1(f)$, $G_2(f_1,f_2)$,and $G_3(f_1,f_2,f_3)$ are referred to as a constant, linear, quadratic, and cubic transfer functions (LTF, QTF, and CTF), and so on.

3.1.3. Impulse and Frequency Response Functions

The kernels in Eq. (3.1) may be considered as describing the system through a series of n^{th} degree impulse response functions. It is presumed that each impulse response function is sufficiently smooth and integrable so that there exists the n^{th} Fourier transform. Accordingly, it is assumed that each n^{th} degree impulse response function corresponds to an n^{th} degree frequency response function, $G_n(\omega_1, \omega_2, \cdots, \omega_n)$. The transform pairs relating impulse and frequency response functions may be defined as follows:

$$g_n(t_1,t_2\cdots t_n)=\frac{1}{(2\pi)^n}\iint\cdots\int G_n(\omega_1,\omega_2\cdots\omega_n)\exp\left(i\sum_{j=1}^{n}\omega_j t_j\right)d\omega_1 d\omega_2\cdots d\omega_n \tag{3.5}$$

$$G_n(\omega_1,\omega_2\cdots\omega_n)=\iint\cdots\int g_n(t_1,t_2\cdots t_n)\exp\left(-i\sum_{j=1}^{n}\omega_j t_j\right)dt_1 dt_2\cdots dt_n \tag{3.6}$$

Regardless of the degree, the basic importance of the transform of the impulse response function is the same; that is, convolution in the time domain usually corresponds to multiplication in the frequency domain (Appendix).

As a consequence of the assumed symmetry of the impulse response functions and the transform, Eq. (3.5) and(3.6), the n^{th} degree frequency response function is also symmetric in its arguments. That is,

$$G_n(\omega_1,\omega_2\cdots\omega_n) = G_n(\omega_2,\omega_1\cdots\omega_n) \tag{3.7}$$

for any and all rearrangements of the ω_j. Additionally, because the impulse response functions are real:

$$G_n(-\omega_1,-\omega_2\cdots-\omega_n) = G_n^*(\omega_1,\omega_2\cdots\omega_n) \tag{3.8}$$

where $*$ denotes the complex conjugate, and all arguments on the left hand side are negative.

3.1.4. Volterra Quadratic input-output model in time domain

In the present work, the functional series (output or response), $y(t)$ may be adequately approximated by a functional polynomial containing terms of degree no higher than the second, which means that Eq. (3.1) at n=2 converts the functional series into a quadratic functional polynomial;

$$y(t) \cong g_0 + \int g_1(t_1)\,x(t-t_1)\,dt_1 + \iint g_2(t_1,t_2)\,x(t-t_1)x(t-t_2)dt_1dt_2 \tag{3.9}$$

If $x(t)$ is assumed to be zero for all time in Eq. (3.9), then by homogeneity,

$$y(t)\big|_{x(t)=0} = g_0 = \text{a constant}$$

Accordingly, the term of degree zero in the series may be discarded as far as outputs due to only fluctuation of inputs (e.g. waves) are considered.

$$y(t) = \int g_1(t_1)x(t-t_1)dt_1 + \iint g_2(t_1,t_2)x(t-t_1)x(t-t_2)dt_1dt_2 \tag{3.10}$$

Therefore, Eq. (3.10) is the fundamental mathematical model in the present study. This model is identical to the model proposed by Tick (1961) as a time invariant quadratic system.

3.1.5. Fourier Transform pair between Impulse Response Function and Frequency Response Function

$g_1(t_1)$, and $g_2(t_1,t_2)$ are the linear and quadratic impulse response functions respectively. The Fourier transform of these gives the linear transfer function (LTF), G_1, and quadratic transfer function (QTF), G_2, making Fourier transform pairs-convention A (Appendix):

$$\begin{aligned}
G_1(\omega) &= \int g_1(t)e^{-i\omega t}dt \\
g_1(t) &= \frac{1}{2\pi}\int G_1(\omega)e^{i\omega t}d\omega \\
G_2(\omega_1,\omega_2) &= \iint g_2(t_1,t_2)e^{-i(\omega_1 t_1+\omega_2 t_2)}dt_1dt_2 \\
g_2(t_1,t_2) &= \frac{1}{(2\pi)^2}\iint G_2(\omega_1,\omega_2)e^{i(\omega_1 t_1+\omega_2 t_2)}d\omega_1 d\omega_2
\end{aligned} \tag{3.11}$$

3.1.6. Symmetry in kernels

$G_1(\omega)$ is a function of mono-frequency ω, while $G_2(\omega_1,\omega_2)$ is a function of bi-frequency ω_1 and ω_2. Because the kernel $g_2(t_1, t_2)$ is assumed to be symmetrical in its arguments:

$$g_2(t_1,t_2) = g_2(t_2,t_1) \tag{3.12}$$

and

$$G_2(\omega_1,\omega_2) = G_2(\omega_2,\omega_1) \tag{3.13}$$

$$G_2^*(\omega_1,\omega_2) = G_2(-\omega_1,-\omega_2) = G_2(-\omega_2,-\omega_1) \tag{3.14}$$

Fig. 3.1 summarizes the results of applying Eqs. (3.13) and (3.14) in the bi-frequency plane for the eight possible coordinate positions of two frequencies *a* and *b*. Eq. (3.13) results in a line of symmetry along the line ω_2=ω_1. Eq. (3.14) results in a line of symmetry of the real part of $G_2(\omega_1,\omega_2)$ defined by $\omega_2 = -\omega_1$ (and it may be noted that along this line the imaginary part of the function is zero). These two lines and the ω_1, ω_2 axes divide the bi-frequency plane into octants, of which the two on either side of the positive ω_1 axis may be arbitrarily chosen for reference. Therefore, without loss in generality, further interpretation of the quadratic frequency response needs only to involve the octants on either side of the positive ω_1 axis. In these octants ω_1 is positive and $|\omega_1| \geq \omega_2$.

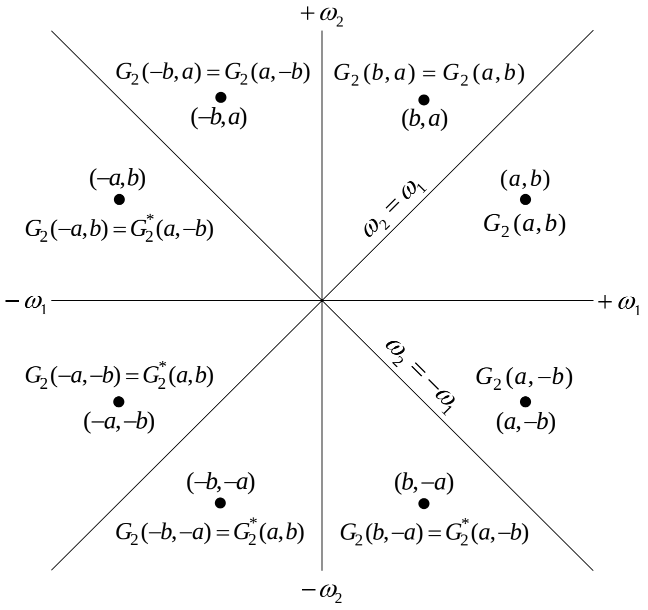

Fig. 3.1 Distribution of QTF in bi-frequency domain showing the symmetries of QTF

3.1.7. Output in terms of frequency response functions

The interpretation of the quadratic frequency response function is less direct than for the linear case, but can be approached in a grossly similar manner.
If in the linear case, the system is considered to be excited by

$$x(t) = a(\omega)\cos\omega t = a(\omega)\frac{\left(e^{i\omega t} + e^{-i\omega t}\right)}{2}$$

The output is then,

$$\begin{aligned}
y_1(t) &= \int g_1(t)x(t-t_1)dt_1 \;= \int g_1(t)\cdot\frac{a(\omega)}{2}\left(e^{i\omega(t-t_1)} + e^{-i\omega(t-t_1)}\right)dt_1 \\
&= \frac{a(\omega)}{2}e^{i\omega t}\int g_1(t)e^{-i\omega t_1}dt_1 + \frac{a(\omega)}{2}e^{-i\omega t}\int g_1(t)e^{i\omega t_1}dt_1 \\
&= \frac{a(\omega)}{2}e^{i\omega t}G_1(\omega) + \frac{a(\omega)}{2}e^{-i\omega t}G_1(-\omega) \;= \frac{a(\omega)}{2}\cdot 2\,\mathrm{Re}\left\{G_1(\omega)e^{i\omega t}\right\} \\
&= \mathrm{Re}\left\{a(\omega)G_1(\omega)e^{i\omega t}\right\}
\end{aligned}$$

In the quadratic system,

$$\begin{aligned}
y_2(t) &= \iint g_2(t_1,t_2)x(t-t_1)x(t-t_2)dt_1dt_2 \\
&= \iint g_2(t_1,t_2)\cdot\frac{a_1(\omega_1)}{2}\left(e^{i\omega_1(t-t_1)} + e^{-i\omega_1(t-t_1)}\right) + \frac{a_1(\omega_1)}{2}\left(e^{i\omega_2(t-t_2)} + e^{-i\omega_2(t-t_2)}\right)dt_1dt_2 \\
&= \frac{a_1^2(\omega_1)}{4}\left[\begin{array}{l} e^{i2\omega_1 t}\iint g_2(t_1,t_2)e^{-i\omega_1 t_1 - i\omega_1 t_2}dt_1dt_2 + e^{i\omega_1 t - i\omega_1 t}\iint g_2(t_1,t_2)e^{-i\omega_1 t_1 + i\omega_1 t_2}dt_1dt_2 \\ + e^{-i\omega_1 t + i\omega_1 t}\iint g_2(t_1,t_2)e^{i\omega_1 t_1 - i\omega_1 t_2}dt_1dt_2 + e^{-i2\omega_1 t}\iint g_2(t_1,t_2)e^{i\omega_1 t_1 + i\omega_1 t_2}dt_1dt_2 \end{array}\right] \\
&= \frac{a_1^2(\omega_1)}{4}\left[e^{i2\omega_1 t}G_2(\omega_1,\omega_1) + G_2(\omega_1,-\omega_1) + G_2(-\omega_1,\omega_1) + e^{-i2\omega_1 t}G_2(-\omega_1,-\omega_1)\right]
\end{aligned}$$

By using symmetry,

$$\begin{aligned}
y_2(t) &= \frac{a_1^2(\omega_1)}{4}\left[e^{i2\omega_1 t}G_2(\omega_1,\omega_1) + e^{-i2\omega_1 t}G_2^*(\omega_1,\omega_1) + G_2(\omega_1,-\omega_1) + G_2(-\omega_1,\omega_1)\right] \\
&= \frac{a_1^2(\omega_1)}{4}\left[2\,\mathrm{Re}\left\{e^{i2\omega_1 t}G_2(\omega_1,\omega_1)\right\} + 2G_2(\omega_1,-\omega_1)\right] \\
&= \underbrace{\frac{a_1^2(\omega_1)}{2}\mathrm{Re}\left\{e^{i2\omega_1 t}G_2(\omega_1,\omega_1)\right\}}_{double} + \underbrace{\frac{a_1^2(\omega_1)}{2}G_2(\omega_1,-\omega_1)}_{mean} \qquad (3.15)
\end{aligned}$$

The first term is for double frequency components and the second term is for mean frequency components in eq (3.15).

$G_1(\omega)$ is interpreted in terms of normalized amplitude and phase of response. To interpret the complete quadratic frequency response, dual harmonic excitation is necessary. Accordingly, it is assumed for illustration that:

$$x(t) = a_1(\omega_1)\cos\omega_1 t + a_2(\omega_2)\cos\omega_2 t = \frac{a_1(\omega_1)}{2}\left(e^{i\omega_1 t} + e^{-i\omega_1 t}\right) + \frac{a_2(\omega_2)}{2}\left(e^{i\omega_2 t} + e^{-i\omega_2 t}\right)$$

In linear system,

$$\begin{aligned}
y_1(t) &= \int g_1(t)x(t-t_1)dt_1 \\
&= \int g_1(t)\cdot\frac{a_1(\omega_1)}{2}\left(e^{i\omega_1(t-t_1)} + e^{-i\omega_1(t-t_1)}\right)dt_1 + \int g_1(t)\cdot\frac{a_2(\omega_2)}{2}\left(e^{i\omega_2(t-t_1)} + e^{-i\omega_2(t-t_1)}\right)dt_1 \\
&= \frac{a_1(\omega_1)}{2}e^{i\omega_1 t}\int g_1(t)e^{-i\omega_1 t_1}dt_1 + \frac{a_1(\omega_1)}{2}e^{-i\omega_1 t}\int g_1(t)e^{i\omega_1 t_1}dt_1 \\
&\qquad + \frac{a_2(\omega_2)}{2}e^{i\omega_2 t}\int g_1(t)e^{-i\omega_2 t_1}dt_1 + \frac{a_2(\omega_2)}{2}e^{-i\omega_2 t}\int g_1(t)e^{i\omega_2 t_1}dt_1 \\
&= \frac{a_1(\omega_1)}{2}e^{i\omega_1 t}G_1(\omega_1) + \frac{a_1(\omega_1)}{2}e^{-i\omega_1 t}G_1(-\omega_1) + \frac{a_2(\omega_2)}{2}e^{i\omega_2 t}G_1(\omega_2) + \frac{a_2(\omega_2)}{2}e^{-i\omega_2 t}G_1(-\omega_2) \\
&= \frac{a_1(\omega_1)}{2}\cdot 2\,\mathrm{Re}\left\{G_1(\omega_1)e^{i\omega_1 t}\right\} + \frac{a_2(\omega_2)}{2}\cdot 2\,\mathrm{Re}\left\{G_1(\omega_2)e^{i\omega_2 t}\right\} \\
&= \mathrm{Re}\left\{a_1(\omega_1)G_1(\omega_1)e^{i\omega_1 t} + a_2(\omega_2)G_1(\omega_2)e^{i\omega_2 t}\right\}
\end{aligned}$$

In quadratic system,

$$\begin{aligned}
y_2(t) &= \iint g_2(t_1,t_2)x(t-t_1)x(t-t_2)dt_1dt_2 \\
&= \iint g_2(t_1,t_2)\cdot\left[\frac{a_1(\omega_1)}{2}\left(e^{i\omega_1(t-t_1)} + e^{-i\omega_1(t-t_1)}\right) + \frac{a_1(\omega_1)}{2}\left(e^{i\omega_2(t-t_1)} + e^{-i\omega_2(t-t_1)}\right)\right]\cdot \\
&\qquad \frac{a_1(\omega_1)}{2}\left(e^{i\omega_1(t-t_2)} + e^{-i\omega_1(t-t_2)}\right) + \frac{a_1(\omega_1)}{2}\left(e^{i\omega_2(t-t_2)} + e^{-i\omega_2(t-t_2)}\right)dt_1dt_2
\end{aligned}$$

Using symmetry,

$$\begin{aligned}
y_2(t) &= \underbrace{\frac{a_1^2(\omega_1)}{2}G_2(\omega_1,-\omega_1) + \frac{a_2^2(\omega_2)}{2}G_2(-\omega_2,\omega_2)}_{mean} \\
&\quad \underbrace{+\frac{a_1^2(\omega_1)}{4}e^{i2\omega_1 t}G_2(\omega_1,\omega_1) + \frac{a_1^2(\omega_1)}{4}e^{-i2\omega_1 t}G_2(-\omega_1,-\omega_1)}_{double}
\end{aligned}$$

$$+\underbrace{\frac{a_2^2(\omega_2)}{4}e^{i2\omega_2 t}G_2(\omega_2,\omega_2)+\frac{a_2^2(\omega_2)}{4}e^{-i2\omega_2 t}G_2(-\omega_2,-\omega_2)}_{double}$$

$$+\underbrace{\frac{a_1(\omega_1)a_2(\omega_2)}{2}e^{i(\omega_1+\omega_2)t}G_2(\omega_1,\omega_2)+\frac{a_1(\omega_1)a_2(\omega_2)}{2}e^{i(-\omega_1-\omega_2)t}G_2(-\omega_1,-\omega_2)}_{sum}$$

$$+\underbrace{\frac{a_1(\omega_1)a_2(\omega_2)}{2}e^{i(\omega_1-\omega_2)t}G_2(\omega_1,-\omega_2)+\frac{a_1(\omega_1)a_2(\omega_2)}{2}e^{i(-\omega_1+\omega_2)t}G_2(-\omega_1,\omega_2)}_{difference}$$

where $G_2(-\omega_1,-\omega_1)=G_2^*(\omega_1,\omega_1)$, $G_2(-\omega_2,-\omega_2)=G_2^*(\omega_2,\omega_2)$,

$G_2(-\omega_1,-\omega_2)=G_2^*(\omega_2,\omega_1)=G_2^*(\omega_1,\omega_2)$, $G_2(-\omega_1,\omega_2)=G_2^*(-\omega_2,\omega_1)=G_2^*(\omega_1,-\omega_2)$ in **Fig. 3.1**.

$$y_2(t)=\underbrace{\frac{a_1^2(\omega_1)}{2}G_2(\omega_1,-\omega_1)+\frac{a_2^2(\omega_2)}{2}G_2(-\omega_2,\omega_2)}_{mean}$$

$$+\underbrace{\frac{a_1^2(\omega_1)}{2}\mathrm{Re}\left\{e^{i2\omega_1 t}G_2(\omega_1,\omega_1)\right\}+\frac{a_1^2(\omega_1)}{2}\mathrm{Re}\left\{e^{-i2\omega_1 t}G_2(\omega_2,\omega_2)\right\}}_{double}$$

$$+\underbrace{a_1(\omega_1)a_2(\omega_2)\,\mathrm{Re}\left\{e^{i(\omega_1+\omega_2)t}G_2(\omega_1,\omega_2)\right\}}_{sum}+\underbrace{a_1(\omega_1)a_2(\omega_2)\,\mathrm{Re}\left\{e^{i(\omega_1-\omega_2)t}G_2(\omega_1,-\omega_2)\right\}}_{difference}$$

Now, we have the output in terms of LTF and QTF:

$$y(t)=y_1(t)+y_2(t)$$

$$\begin{aligned}&=\mathrm{Re}\left\{a_1(\omega_1)G_1(\omega_1)e^{i\omega_1 t}+a_2(\omega_2)G_1(\omega_2)e^{i\omega_2 t}\right\}\\&\quad+\underbrace{\frac{a_1^2(\omega_1)}{2}G_2(\omega_1,-\omega_1)+\frac{a_2^2(\omega_2)}{2}G_2(-\omega_2,\omega_2)}_{mean}\\&\quad+\underbrace{\frac{a_1^2(\omega_1)}{2}\mathrm{Re}\left\{e^{i2\omega_1 t}G_2(\omega_1,\omega_1)\right\}+\frac{a_1^2(\omega_1)}{2}\mathrm{Re}\left\{e^{-i2\omega_1 t}G_2(\omega_2,\omega_2)\right\}}_{double}\\&\quad+\underbrace{a_1(\omega_1)a_2(\omega_2)\,\mathrm{Re}\left\{e^{i(\omega_1+\omega_2)t}G_2(\omega_1,\omega_2)\right\}}_{sum}+\underbrace{a_1(\omega_1)a_2(\omega_2)\,\mathrm{Re}\left\{e^{i(\omega_1-\omega_2)t}G_2(\omega_1,-\omega_2)\right\}}_{difference}\end{aligned}\tag{3.16}$$

We have a total of eight frequency response terms in Eq. (3.16). The first two terms are the linear responses due to each of the dual waves, while the rest six QTF terms consist of the mean terms, which are functions of each wave frequency, the second two expresses in double frequency; the third represents the sum frequency and the last represents the difference frequency term.

Elimination of the redundant terms due to the symmetry of QTFs in **Fig. 3.1** leads to the resultant QTF distributed in the two octants as shown in **Fig. 3.2**. The octant of bi-frequency plane above the positive ω_1–axis corresponds to the portion of the quadratic frequency response which defines *sum-frequency* interactions, and the octant below the positive ω_1 –axis corresponds to the portion of the function which defines *difference-frequency* interactions. We may add the distribution of LTF along the mono-frequency ω_1-axis. The mean and double frequency terms are distributed along the limiting lines: $\omega_1 = -\omega_2$ and $\omega_1 = \omega_2$. The terms on these two limiting lines are created when the dual waves become identical. Since QTF is continuous function of bi-frequency, the low frequency response tends toward the approximate model derived by Newman (1974).

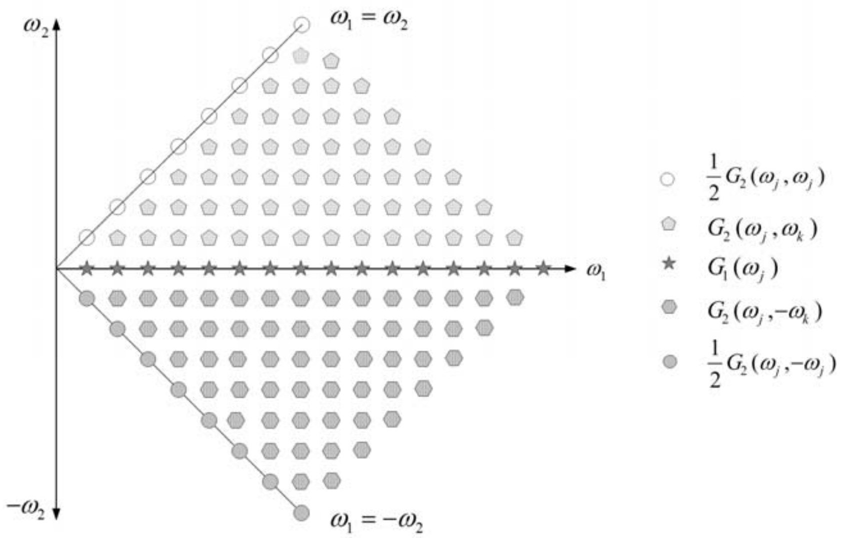

Fig. 3.2 Schematic diagram of LTF and QTF distributed in bi-frequency domain.

The response in a compact form:

$$
\begin{aligned}
y(t) &= y_1(t) + y_2(t) \\
&= \mathrm{Re}\sum_{j=1}^{2} a_j G_1 \exp(-i\omega_j t) + \frac{1}{2}\mathrm{Re}\sum_{j=1}^{2}\sum_{k=1}^{2} a_j a_k \left\{ \begin{array}{l} G_{2\,jk}^{+} \exp\left[-i(\omega_j + \omega_k)t\right] \\ +G_{2\,jk}^{-} \exp\left[-i(\omega_j - \omega_k)t\right] \end{array} \right\}
\end{aligned}
\tag{3.17}
$$

One may express the output with finite number of frequency in a general form as

$$
\begin{aligned}
y(t) &= y_1(t) + y_2(t) \\
&= \mathrm{Re}\sum_{j=1}^{n} a_j G_1 \exp(-i\omega_j t) + \frac{1}{2}\mathrm{Re}\sum_{j=1}^{n}\sum_{k=1}^{n} a_j a_k \left\{ \begin{array}{l} G_{2jk}^{+} \exp\left[-i(\omega_j + \omega_k)t\right] \\ +G_{2jk}^{-} \exp\left[-i(\omega_j - \omega_k)t\right] \end{array} \right\}
\end{aligned}
\tag{3.18}
$$

Given the random input time series and LTF and QTF obtained either from model test data or theoretical computation, one may reconstruct the output using the synthesized formula Eq.(3.18), which will be utilized in the Reconstruction later for both Gaussian and non-Gaussian method.

3.1.8. The output frequency axis (+Ω_2)

It is advantageous to introduce the frequency transformation from ω_1, ω_2–plane into a difference- and sum-frequency plane in accordance with

$$\Omega_1 = \omega_1 - \omega_2,\ \Omega_2 = \omega_1 + \omega_2 \tag{3.19}$$

Ω_1- and Ω_2-axis are coincident with the symmetry lines of the function $G_2(\omega_1,\omega_2)$. The quadrant of Ω_1, Ω_2-plane, in which both difference- and sum-frequencies are positive, corresponds to the quadrant selected earlier in **Fig. 3.2** in interpreting the response to dual excitation. In accordance with the earlier discussion of dual excitation the sum-frequency Ω_2 is identical to the output frequency of the quadratic system. Any combination of input frequencies $\omega_1 + |\omega_2|$ on the line $\Omega_2 = \omega_1 + \omega_2 =$ constant will generate a component at the frequency. We have the output frequencies due to dual excitation of ω_1 and ω_2 making $2\omega_1$ & $2\omega_2$, $\omega_1 - \omega_2$, and $\omega_1 + \omega_2$. The output frequency of QTF along Ω_1-axis is zero (Ω_2=0). Cosidering all of the above we have six output frequencies of QTF. The QTF disributed in the domain bounded by the dotted line (**Fig. 3.3**) will produce dominently a slow varying response if the ouput frequency Ω_2 is low. $\omega_1 = -\omega_2$ and $\omega_1 = \omega_2$ along the Ω_1- and Ω_2-axis, respectively, in **Fig. 3.2** correponds to the zero and double frequency along the Ω_2-axis.

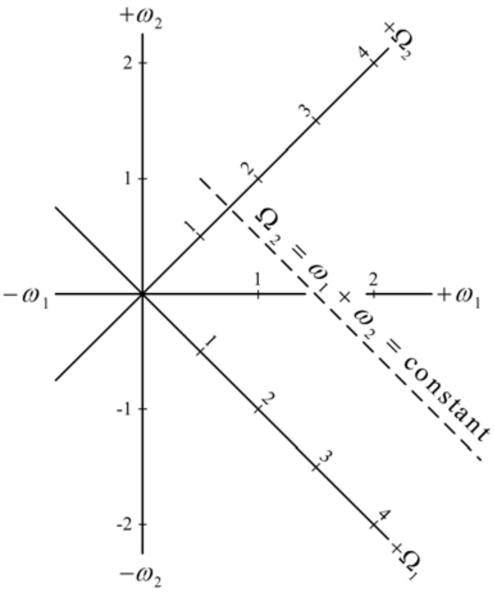

Fig. 3.3 Sketch of difference- and sum-frequency plane

3.2. Volterra quadratic model with Gaussian input

3.2.1. Estimation of LTF from measurement

In order to derive the cross correlation function between $x(t)$ and $y(t)$ from Eq. (3.10):

$$y(t) - E[y(t)] = \int g_1(t_1)x(t-t_1)dt_1 + \iint g_2(t_1,t_2)x(t-t_1)x(t-t_2)dt_1dt_2 - E[y(t)] \quad (3.20)$$

Multiply $x(t-\tau)$ both side and take the expected value.

$$\begin{aligned} &E\left[\{y(t)-E[y(t)]\}x(t-\tau)\right] \\ &= \int g_1(t_1)E[x(t-t_1)x(t-\tau)]dt_1 \\ &+ \iint g_2(t_1,t_2)E[x(t-t_1)x(t-t_2)x(t-\tau)]dt_1dt_2 - E[y(t)]E[x(t-\tau)] \end{aligned} \quad (3.21)$$

Because the input is assumed to be zero mean Gaussian, the last two terms are zero. i.e. $E[x(t-\tau)]=0$ and expected value of triple products of Gaussian variable are zero,

$$E\left[\{y(t)-E[y(t)]\}x(t-\tau)\right] = \int g_1(t_1)E[x(t-t_1)x(t-\tau)]dt_1 \quad (3.22)$$

Thus, cross-correlation is

$$R_{xy}(\tau) = \int g_1(t_1)R_{xx}(t_1-\tau)dt_1 \quad (3.23)$$

Take the Fourier transforms (Convention A) of Eq. (3.23)

$$\int R_{xy}(\tau)e^{-i\omega\tau}d\tau = \int g_1(t_1)e^{-i\omega t_1}dt_1 \cdot \int R_{xx}(\tau - t_1)e^{-i\omega(\tau - t_1)}d\tau \tag{3.24}$$

$$S_{xy}(\omega) = G_1(\omega)\cdot S_{xx}(\omega) \tag{3.25}$$

The measured input and output are used for estimation of the power spectrum and cross spectrum, by employing Blackman-Tukey, or Bendat (1990) method, from which LTF:

$$G_1(\omega) \;=\; \frac{U_{xy}(\omega)}{U_{xx}(\omega)} \tag{3.26}$$

,where U_{xx} is one-sided input energy spectrum and U_{xy} one-sided cross spectrum.

3.2.2. Estimation of QTF from measurement

3.2.2.1. The n-dimensional form of Parseval formula

The *n*-dimensional form of Parseval formula is useful in manipulations involving random processes. According to Barrett (1963) it is as follows:

$$\begin{aligned} &\iint\cdots\int f_1(t_1,t_2\cdots t_n)\; f_2(t_1,t_2\cdots t_n)dt_1dt_2\cdots dt_n \\ &= \frac{1}{(2\pi)^n}\iint\cdots\int F_1^*(\omega_1,\omega_2\cdots\omega_n)\,F_2(\omega_1,\omega_2\cdots\omega_n)d\omega_1 d\omega_2\cdots d\omega_n \end{aligned} \tag{3.27}$$

,where the $*$ denotes a complex conjugate and $f_\mathrm{n}(t_1,t_2,\cdots,t_\mathrm{n})$, and $F_\mathrm{n}(\omega_1,\omega_2,\cdots,\omega_\mathrm{n})$, are Fourier transform pairs defined:

$$\begin{aligned} F_2(\omega_1,\omega_2\cdots\omega_n) &= \iint\cdots\int f_j(t_1,t_2\cdots t_n)\exp\left(-i\sum_{r=1}^{n}\omega_r t_r\right)dt_1dt_2\cdots dt_n \\ f_j(t_1,t_2\cdots t_n) &= \frac{1}{(2\pi)^n}\iint\cdots\int F_j(\omega_1,\omega_2\cdots\omega_n)\exp\left(i\sum_{r=1}^{n}\omega_r t_r)\right)d\omega_1 d\omega_2\cdots d\omega_n \end{aligned} \tag{3.28}$$

3.2.2.2. Theoretical mean of the output

It is assumed that the input $x(t)$ is a stationary, Gaussian zero mean process. The auto-correlation of the process will be denoted $R_{xx}(\tau)$ and is defined as follows:

$$R_{xx}(\tau) = E\left[x(t)x(t-\tau)\right] \tag{3.29}$$

,where $E[\cdot]$ denotes the statistical expectation. The two-sided spectrum of the process is by definition:

$$S_{xx}(\omega)=\int_{-\infty}^{\infty} R_{xx}(\tau)e^{-i\omega\tau}d\tau \tag{3.30}$$

and the inverse FT gives the autocorrelation function by definition

$$R_{xx}(\tau)=\frac{1}{2\pi}\int_{-\infty}^{\infty} S_{xx}(\omega)e^{i\omega\tau}d\omega \tag{3.31}$$

Thus,

$$R_{xx}(0)=\frac{1}{\pi}\int_{0}^{\infty} S_{xx}(\omega)d\omega \tag{3.32}$$

The scale spectrum with the one-sided spectrum $U_{xx}(\omega)$ is given by

$$S_{xx}(\omega)=\pi U_{xx}(\omega), \quad 0\le\omega\le\infty \tag{3.33}$$

by satisfying the relation between the total variance and integral of one-sided spectrum :

$$R_{xx}(0)=\int_{0}^{\infty} U_{xx}(\omega)d\omega \tag{3.34}$$

Taking the expected value of the Volterra quadratic Eq. (3.10)

$$E\left[y(t)\right]=\int g_1(t_1)E\left[x(t-t_1)\right]dt_1+\iint g_2(t_1,t_2)E\left[x(t-t_1)x(t-t_2)\right]dt_1dt_2 \tag{3.35}$$

$$\begin{aligned} E\left[y(t)\right]&=\iint g_2(t_1,t_2)E\left[x(t-t_1)x(t-t_2)\right]dt_1dt_2 \\ &=\iint g_2(t_1,t_2)R_{xx}(t_1-t_2)dt_1dt_2 \end{aligned} \tag{3.36}$$

where the first term in Eq. (3.35) is zero by definition of zero mean input system. Applying Parseval's formula, Eq. (3.27) and (3.28); let: $f_1(t_1,t_2)=g_2(t_1,t_2)$ and $f_2(t_1,t_2)=R(t_1-t_2)$.

Multiplying the above with $e^{i\omega_1\tau_2-i\omega_1\tau_2}=1$:

$$\begin{aligned} F_2(\omega_1,\omega_2)&=\iint R_{xx}(t_1-t_2)\,e^{-i\omega_1(t_1-t_2)}e^{-i(\omega_1+\omega_2)t_2}dt_1dt_2 \\ &=\iint R_{xx}(\tau)e^{-i\omega_1\tau}\; e^{-i(\omega_1+\omega_2)t_2}d\tau dt_2 \\ &=\int R_{xx}(\tau)e^{-i\omega_1\tau}d\tau\cdot\int e^{-i(\omega_1+\omega_2)t_2}dt_2 \end{aligned} \tag{3.37}$$

By using of FT pair of Dirac delta,

$$F_2(\omega_1,\omega_2)=S_{xx}(\omega_1)\cdot 2\pi\,\delta(\omega_1+\omega_2) \tag{3.38}$$

Substituting (3.38) in eq (3.27):

$$E[y(t)]=\frac{1}{(2\pi)^2}\iint G_2^{*}(\omega_1,\omega_2)S_{xx}(\omega_1)\cdot 2\pi\,\delta(\omega_1+\omega_2)d\omega_1d\omega_2$$

Let $\omega_2 = -\omega_1$,

$$E[y(t)] = \frac{1}{2\pi}\int G_2^*(\omega_1, -\omega_1) S_{xx}(\omega_1) d\omega_1 \cdot \int \delta(\omega_1 - \omega_1) d\omega_1$$

By changing variable ω_1 to ω, and using symmetry in arguments, $G_2^*(\omega, -\omega) = G_2\ (\omega, -\omega)$.

$$\begin{aligned} E[y(t)] &= \frac{1}{2\pi}\int_{-\infty}^{\infty} G_2(\omega, -\omega) S_{xx}(\omega) d\omega \\ &= \frac{1}{2}\int_{-\infty}^{\infty} G_2(\omega, -\omega) U_{xx}(|\,\omega\,|) d\omega \\ &= \int_{0}^{\infty} G_2(\omega, -\omega) U_{xx}(\omega) d\omega \end{aligned} \tag{3.39}$$

where it can be shown that $G_2(\omega, -\omega)$ is real. $U_{xx}\ (\omega)$ is a one-sided input spectrum. $E[y(t)]$ is the expected value of output. Eq. (3.39) was given by Maruo (1957).

Eq. (3.39) has been derived with only assumption of zero-mean input; thus, Eq. (3.39) is applicable to QTFs estimated by the Gaussian or non-Gaussian method.

Since the mean of the response to a monochromatic wave is from (3.17)

$$\overline{Y}_2(\omega) = A^2 \frac{1}{2} G_2(\omega, -\omega) \tag{3.40}$$

The mean of the response in the random wave:

$$E[y(t)] = 2\int_0^{\infty} \frac{\overline{Y}_2(\omega)}{A^2(\omega)} U_{xx}(\omega) d\omega \tag{3.41}$$

3.2.2.3. Energy density spectrum of linear and quadratic response

The energy spectrum of the total output is determined by taking the auto-correlation of the output $y(t)$, and applying Fourier transform. The Parseval's formula is applied similar way. The 2nd-order moment or auto-correlation of the output about zero-mean:

$$\begin{aligned} M_{yy}(\tau) &= E\left[\{y(t) - E[y(t)]\}\{y(t+\tau) - E[y(t+\tau)]\}\right] \\ &= \frac{1}{2\pi}\int_{-\infty}^{\infty} \left|G_1(\omega)\right|^2 S_{xx}(\omega) e^{i\tau\omega} d\omega \\ &\quad + \frac{2}{(2\pi)^2}\int_{-\infty}^{\infty}\int_{-\infty}^{\infty} \left|G_2(\omega_1, \omega_2)\right|^2 S_{xx}(\omega_1) S_{xx}(\omega_2) e^{i\tau(\omega_1+\omega_2)} d\omega_1 d\omega_2 \end{aligned} \tag{3.42}$$

Letting

$\omega_1 = \omega - \xi$; $\omega_2 = \xi$, in the second term:

$$\begin{aligned} M_{yy}(\tau) &= \frac{1}{2\pi}\int_{-\infty}^{\infty}\left|G_1(\omega)\right|^2 S_{xx}(\omega)e^{i\omega\tau}d\omega \\ &+\frac{1}{2\pi^2}\int_{-\infty}^{\infty}\int_{-\infty}^{\infty}\left|G_2(\omega-\xi,\omega)\right|^2 S_{xx}(\omega-\xi)S_{xx}(\xi)d\xi e^{i\omega\tau}d\omega \end{aligned} \tag{3.43}$$

Applying the inverse Fourier transform on each term we obtain the energy spectrum of the linear and quadratic response:

$$S_{yy}(\omega) = \left|G_1(\omega)\right|^2 S_{xx}(\omega) + \frac{1}{\pi}\int_{-\infty}^{\infty}\left|G_2(\omega-\xi,\xi)\right|^2 S_{xx}(\omega-\xi)S_{xx}(\xi)d\xi \tag{3.44}$$

Folding the double-sided integral about ξ, and applying (3.33)

$$U_{yy}(\omega) = \left|G_1(\omega)\right|^2 U_{xx}(\omega) + 2\int_{0}^{\infty}\left|G_2(\omega-\xi,\xi)\right|^2 U_{xx}(|\,\omega-\xi\,|)U_{xx}(|\,\xi\,|)d\xi \tag{3.45}$$

3.2.2.4. The third moment function and cross-bi-spectrum

Tick (1961) defines the cross-bispectrum (CBS) as the double Fourier transform of a third moment function $M_3(\tau_1, \tau_2)$ as:

$$M_{xxy}(\tau_1,\tau_2) = E[x(t+\tau_2)x(t+\tau_1)\{y(t)-E[y(t)]\}] \tag{3.46}$$

$$CBS(\omega_1,\omega_2) = \frac{1}{(2\pi)^2}\iint e^{-i(\tau_1\omega_1+\tau_2\omega_2)}M_{xxy}(\tau_1,\tau_2)d\tau_1 d\tau_2 \tag{3.47}$$

Dalzel (1972) modified the third moment function for $y(t)$ by writing:

$$M_{xxy}(\tau_1,\tau_2) = E\left[x(t+\tau_1)x(t-\tau_1)\left\{y(t-\tau_2)-E[y(t-\tau_2)]\right\}\right] \tag{3.48}$$

From Eq. (3.10) and (3.35)

$$y(t-\tau_2) = \int g_1(t_1)x(t-\tau_2-t_1)dt_1 + \iint g_2(t_1,t_2)x(t-\tau_2-t_1)x(t-\tau_2-t_2)dt_1 dt_2 \tag{3.49}$$

$$\begin{aligned} E[y(t-\tau_2)] &= \int g_1(t_1)E[x(t-\tau_2-t_1)]dt_1 \\ &+\iint g_2(t_1,t_2)E[x(t-\tau_2-t_1)x(t-\tau_2-t_2)]dt_1 dt_2 \\ &= \iint g_2(t_1,t_2)R_{xx}(t_1-t_2)dt_1 dt_2 \end{aligned} \tag{3.50}$$

Subtracting Eq. (3.50) from Eq. (3.49)

$$\begin{aligned} y(t-\tau_2)-E[y(t-\tau_2)] &= \int g_1(t_1)x(t-\tau_2-t_1)dt_1 \\ &+\iint g_2(t_1,t_2)x(t-\tau_2-t_1)x(t-\tau_2-t_2)dt_1dt_2 \\ &-\iint g_2(t_1,t_2)R_{xx}(t_1-t_2)dt_1dt_2 \\ &=\int g_1(t_1)x(t-\tau_2-t_1)dt_1 \\ &+\iint g_2(t_1,t_2)\left\{x(t-\tau_2-t_1)x(t-\tau_2-t_2)-R_{xx}(t_1-t_2)\right\}dt_1dt_2 \end{aligned} \tag{3.51}$$

Substituting Eq. (3.51) into (3.48)

$$\begin{aligned} M_{xxy}(\tau_1,\tau_2) &= E[x(t+\tau_1)x(t-\tau_1)\{y(t-\tau_2)-E[y(t-\tau_2)]\}] \\ &=\int g_1(t_1)E[x(t+\tau_1)x(t-\tau_1)x(t-\tau_2-t_1)]dt_1 \\ &+\iint g_2(t_1,t_2)E[x(t+\tau_1)x(t-\tau_1)\cdot \\ &\quad \{x(t-\tau_2-t_1)x(t-\tau_2-t_2)-R_{xx}(t_1-t_2)\}]dt_1dt_2 \end{aligned} \tag{3.52}$$

Noting that the expected values of triple products of Gaussian variables are zero and the fourth order moment of Gaussian system gives: $E[x(t+\tau_1)\ x(t-\tau_1)\ x(t-\tau_2-\tau_1)]=0$ and $x(t+\tau_1)\ x(t-\tau_1)\ =x(t+2\tau_1)]$

$$\begin{aligned} E[x(t_1)x(t_2)x(t_3)x(t_4)] &= R_{xx}(t_2-t_1)\cdot R_{xx}(t_4-t_3) \\ &+R_{xx}(t_3-t_1)\cdot R_{xx}(t_4-t_2) \\ &+R_{xx}(t_4-t_1)\cdot R_{xx}(t_3-t_2) \end{aligned} \tag{3.53}$$

Then,

$$\begin{aligned} M_{xxy}(\tau_1,\tau_2) &= \iint g_2(t_1,t_2)R_{xx}(t_1+\tau_1+\tau_2)R_{xx}(t_2-\tau_1+\tau_2)dt_1dt_2 \\ &+\iint g_2(t_1,t_2)R_{xx}(t_1-\tau_1+\tau_2)R_{xx}(t_2+\tau_1+\tau_2)dt_1dt_2 \end{aligned} \tag{3.54}$$

Since $g_2(t_1,t_2)$ is symmetric in t_1 and t_2 and the intergration limits are infinite, the two double integrals in Eq.(3.54) are equivalent. Thus,

$$M_{xxy}(\tau_1,\tau_2)=2\iint g_2(t_1,t_2)R_{xx}(t_1+\tau_1+\tau_2)R_{xx}(t_2-\tau_1+\tau_2)dt_1dt_2 \tag{3.55}$$

Utilizing the Parseval formula Eq.(3.27):

$$f_1(t_1,t_2)=g_2(t_1,t_2),\quad f_2(t_1,t_2)=R_{xx}(t_1+\tau_1+\tau_2)R_{xx}(t_2+\tau_2-\tau_1),\ F_1(\omega_1,\omega_2)=G_2(\omega_1,\omega_2)$$

$$
\begin{aligned}
F_2\left(\omega_1,\omega_2\right) &= \iint R_{xx}(t_1+\tau_1+\tau_2)R_{xx}(t_2+\tau_2-\tau_1)e^{-i\omega_1 t_1}e^{-i\omega_2 t_2}dt_1 dt_2 \\
&= \int R_{xx}(t_1+\tau_1+\tau_2)e^{-i\omega_1(t_1+\tau_1+\tau_2)}dt_1\, e^{-i\omega_1(\tau_1+\tau_2)} \;\cdot \\
&\quad \int R_{xx}(t_2+\tau_2-\tau_1)e^{-i\omega_2(t_2+\tau_2-\tau_1)}dt_2\, e^{-i\omega_2(\tau_2-\tau_1)} \\
&= S_{xx}(\omega_1)S_{xx}(\omega_2)e^{\{i\omega_1(\tau_1+\tau_2)+i\omega_2(\tau_2-\tau_1)\}} \\
&= S_{xx}(\omega_1)S_{xx}(\omega_2)e^{\{i\tau_1(\omega_1-\omega_2)+i\tau_2(\omega_1+\omega_2)\}}
\end{aligned}
$$

Substituting them into Parseval formula Eq. (3.27)

$$M_{xxy}(\tau_1,\tau_2)=\frac{2}{(2\pi)^2}\iint G_2^{\,*}(\omega_1,\omega_2)S_{xx}(\omega_1)S_{xx}(\omega_2)e^{\{i\tau_1(\omega_1-\omega_2)+i\tau_2(\omega_1+\omega_2)\}}d\omega_1 d\omega_2$$

Let the variables be changed to sum and difference frequencies(3.19):

$$
\begin{aligned}
M_{xxy}(\tau_1,\tau_2) = \frac{1}{(2\pi)^2}\iint G_2^{\,*}\left(\frac{\Omega_1+\Omega_2}{2},\frac{\Omega_1-\Omega_2}{2}\right)\cdot \\
S_{xx}\left(\frac{\Omega_1+\Omega_2}{2}\right)S_{xx}\left(\frac{\Omega_1-\Omega_2}{2}\right)e^{i(\tau_1\Omega_1+\tau_2\Omega_2)}d\Omega_1 d\Omega_2
\end{aligned}
\tag{3.56}
$$

Where the Jacobian *J*=1/2 is applied in coordinate transform, ($d\omega_1 d\omega_2$=1/2×$d\Omega_1 d\Omega_2$) Thus, the modified CBS is the double Fourier transform of the third moment (3.56).

$$
\begin{aligned}
C(\Omega_1,\Omega_2) &= \iint M_{xxy}(\tau_1,\tau_2)e^{-i(\tau_1\Omega_1+\tau_2\Omega_2)}d\tau_1 d\tau_2 \\
&= G_2^*(\omega_1,\omega_2)S_{xx}(\omega_1)S_{xx}(\omega_2)
\end{aligned}
\tag{3.57}
$$

where the transform pair:

$$
\begin{aligned}
M_{xxy}(\tau_1,\tau_2) &= \frac{1}{(2\pi)^2}\iint C(\Omega_1,\Omega_2)e^{i(\tau_1\Omega_1+\tau_2\Omega_2)}d\Omega_1 d\Omega_2 \\
C(\Omega_1,\Omega_2) &= \iint M_{xxy}(\tau_1,\tau_2)e^{-i(\tau_1\Omega_1+\tau_2\Omega_2)}d\tau_1 d\tau_2
\end{aligned}
$$

Comparing with Eq. (3.11) and the QTF is defined by

$$G_2(\omega_1,\omega_2)=\frac{C^*(\omega_1-\omega_2,\omega_1+\omega_2)}{S_{xx}(\omega_1)S_{xx}(\omega_2)}\ ,\ -\infty\le(\omega_1,\ \omega_2)\le+\infty \tag{3.58}$$

provided the denominator is not zero. This simple fact becomes a serious problem in estimating the CBS. It happens because the energy spectrum has very small values in the tails (**Fig. 3.4**). Consequently, the large diverging magnitude of QTF occurs due to the division process, and this unrealistic QTF should be eliminated carefully.

Scaling the one-sided energy spectrum to two-sided spectrum with Eq. (3.33):

$$G_2(\omega_1,\omega_2)=\frac{C^*(\omega_1-\omega_2,\omega_1+\omega_2)}{\pi^2 U_{xx}(\omega_1)U_{xx}(\omega_2)},\quad 0\le(\omega_1,|\,\omega_2\,|)\le\infty \tag{3.59}$$

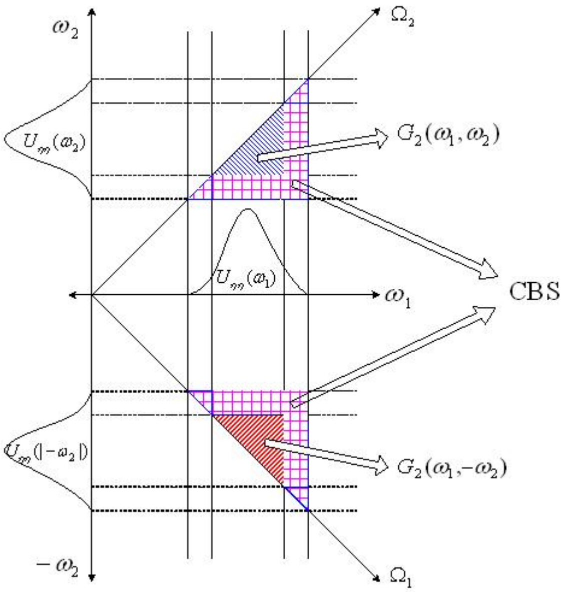

Fig. 3.4 Schematic diagram for extracting G_2 from CBS and energy spectra

3.2.2.5. Algorithm for the estimate of cross-bispectrum

Dalzell (1972, 1976) derived the formula for estimation of cross-bispectrum that is similar to Blackman-Tukey method for cross- and auto-spectrum following Shaman (1963). Hann or Hamming widow have been used with the Blackman-Tukey method. For finite sample, it is only possible to estimate the cross bispectral averages rather than accrual densities.

$$\hat{C}(\Omega_1,\Omega_2) = \iint H(\Omega_3,\Omega_4)\,C(\Omega_1+\Omega_3,\Omega_2+\Omega_4)\,d\Omega_3 d\Omega_4 \qquad (3.60)$$

where the average is weighted by the kernels or “cross-bispectral window,” $H(\Omega_3,\Omega_4)$. since the window is for average over frequency, its integral should be unity.

$$\iint H(\Omega_3,\Omega_4)\,d\Omega_3 d\Omega_4 = 1 \qquad (3.61)$$

Applying Parseval (3.27) and Fourier transform pair (Appendix) to Eq. (3.60)

$$F_1(\Omega_3,\Omega_4) = C(\Omega_1+\Omega_3,\Omega_2+\Omega_4) \qquad (3.62)$$

$$F_2(\Omega_3,\Omega_4) = H(\Omega_3,\Omega_4) \qquad (3.63)$$

$$\begin{aligned} f_1(\tau_1,\tau_2) &= \frac{1}{(2\pi)^2}\iint \hat{C}(\Omega_1+\Omega_3,\Omega_2+\Omega_4)e^{i(\Omega_3\tau_1+\Omega_4\tau_2)}d\Omega_3 d\Omega_4 \\ &= e^{-i(\Omega_1\tau_1+\Omega_2\tau_2)}\frac{1}{(2\pi)}\iint \hat{C}(\Omega_1+\Omega_3,\Omega_2+\Omega_4)d\Omega_3 d\Omega_4 \\ &\qquad \cdot\, e^{i\{\tau_1(\Omega_1+\Omega_3)+\tau_2(\Omega_2+\Omega_4)\}}d(\Omega_1+\Omega_3)d(\Omega_2+\Omega_4) \\ &= M_{xxy}(\tau_1,\tau_2)\,e^{-i(\Omega_1\tau_1+\Omega_2\tau_2)} \end{aligned} \tag{3.64}$$

Defining $h(\tau_1,\tau_2) = f_2(\tau_1,\tau_2)$

$$h(\tau_1,\tau_2) = \frac{1}{(2\pi)^2}\iint H(\Omega_3,\Omega_4)e^{i(\Omega_3\tau_1+\Omega_4\tau_2)}d\Omega_3 d\Omega_4 \tag{3.65}$$

Then

$$\hat{C}(\Omega_1,\Omega_2) = \iint M_{xxy}(-\tau_1,-\tau_2)\,h'(\tau_1,\tau_2)\,e^{i(\Omega_1\tau_1+\Omega_2\tau_2)}d\Omega_1 d\Omega_2 \tag{3.66}$$

where, $h'(\tau_1,\ \tau_2) = (2\pi)^2 h(\tau_1,\ \tau_2)$ is a lag window.

Eq. (3.66) has the same form as Eq. (3.57) with the "lag window". The above is the continuous form of the cross-bispectral estimate. The discredited form is derived applying Eq. (3.48), (3.61), (3.65), and (3.66). The two-dimensional Hamming filter is used for the lag window. More details are in derived in the reference (Dalzell, 1972).

$$\begin{aligned} \hat{C}(\Omega_1,\Omega_2) = \left(\frac{\Delta t}{e_1+e_2}\right)^2 &\sum_{j=0}^{m} r(j)\,(e_1+e_2\cos\pi j/m)\cos(\pi p_1 j/m)\,\cdot \\ &\sum_{k=-u}^{u}(e_1+e_2\cos\pi k/u)[\cos(\pi p_2 k/u)+i\sin(\pi p_2 k/u)]\,\cdot \\ &\frac{1}{N_s}\sum_n x(n+j)x(n-j)y(n+k) \end{aligned} \tag{3.67}$$

This equation is for cross-bispectral averages over a bispectral window which is essentially a two dimensional Hamming filter as defined by the product of terms of the form (e_1+$e_2$cos$\pi j/m$) with e_1=0.54 and e_2=0.46.

with

$$r(j) = \begin{cases} 1 & \text{for } j=0 \\ 2 & \text{otherwise} \end{cases} \quad \text{and} \quad \Omega_1 = \frac{\pi P_1}{m\Delta t},\ \ \Omega_2 = \frac{\pi P_2}{u\Delta t}$$

$x(N)$ = the input time series corrected to zero sample mean

$y(N)$ = the output time series corrected to zero sample mean

N_s= the number of possible products summed
Δt= sampling interval used to convert the original analog time histories into time series
m = maximum lags in difference frequency direction (Ω_1)
n = maximum lags in sum frequency direction (Ω_2)

letting:

$$\hat{C}(P_1,P_2)=\mathrm{Re}\{\hat{C}(P_1,P_2)\}+i\,\mathrm{Im}\{\hat{C}(P_1,P_2)\} \tag{3.68}$$

$$\begin{aligned}
\mathrm{Re}\{\hat{C}(P_1,P_2)\} &= \left(\frac{\Delta t}{e_1+e_2}\right)^2 \sum_{j=0}^{m}\{r(j)\,(e_1+e_2\cos\pi j/m)\cos(\pi P_1 j/m)\cdot \\
&\quad [\frac{1}{N_s}\sum_n x(n+j)x(n-j)\sum_{k=0}^{u}\frac{r(k)}{2}(e_1+e_2\cos\pi k/u)\cdot \\
&\quad \cos(\pi P_2 k/u)(y(n-k)+y(n+k))]\} \\
&= \left(\frac{\Delta t}{e_1+e_2}\right)^2 \sum_{k=0}^{u}\{\frac{r(k)}{2}(e_1+e_2\cos\pi k/u)\cos(\pi P_2 k/u)\cdot \\
&\quad [\frac{1}{N_s}\sum_n (y(n-k)+y(n+k))\cdot\sum_{j=0}^{m} r(j)(e_1+e_2\cos\pi j/m)\cdot \\
&\quad \cos(\pi P_1 j/m)y(n+j)y(n-j)]\}
\end{aligned} \tag{3.69}$$

$$\begin{aligned}
\mathrm{Im}\{\hat{C}(P_1,P_2)\} &= \left(\frac{\Delta t}{e_1+e_2}\right)^2 \sum_{j=0}^{m}\{r(j)\,(e_1+e_2\cos\pi j/m)\cos(\pi P_1 j/m)\cdot \\
&\quad [\frac{1}{N_s}\sum_n x(n+j)x(n-j)\sum_{k=1}^{u}(e_1+e_2\cos\pi k/u)\cdot \\
&\quad \sin(\pi P_2 k/u)(y(n+k)-y(n-k))]\} \\
&= \left(\frac{\Delta t}{e_1+e_2}\right)^2 \sum_{k=1}^{u}\{\,(e_1+e_2\cos\pi k/u)\sin(\pi P_2 k/u)\cdot \\
&\quad [\frac{1}{N_s}\sum_n (y(n+k)+y(n-k))\cdot\sum_{j=0}^{m} r(j)(e_1+e_2\cos\pi j/m)\cdot \\
&\quad \cos(\pi P_1 j/m)y(n+j)y(n-j)]\}
\end{aligned} \tag{3.70}$$

The results, eqs (3.69) and (3.70) have been arranged in two forms to facilitate evaluations for the present purpose. The first form is computationally convenient for evaluation of $\hat{C}(P_1, P_2)$ along the line P_2=constant, the second for evaluation along the line P_1=constant.

3.3. Volterra quadratic model with non-Gaussian input

The Volterra quadratic model with Gaussian assumption is regarded as an approximate model. Kim and Powers (1988) have invesitigated the Volterra quadratic model with assumption of the non-Gaussian input and validated the model using a mathematical non-Gaussian input. The key idea in modeling a quadratic system in the frequency domain is to model the system with a parallel combination of linear and quadratic transfer functions (Schetzen,1981). The Volterra quadratic model Eq. (3.10) is written in the frequency domain assuming the non-Gaussian input as following

$$Y(f_m) = H_1(f_m)X(f_m) + \sum\sum\nolimits_{i+j=m} H_2(f_{i,}f_j)X(f_i)X(f_j) \tag{3.71}$$

$X(f_m)$ = the discrete Fourier transform of input time series
$Y(f_m)$ = the discrete Fourier transform of output time series
$H_1(f_m)$ = linear transfer functions
$H_2(f_{i,}\, f_j)$ = quadratic transfer functions

Without loss of generality, the quadratic transfer function can always be written in a symmetric in its arguments; Therefore, we have $H_2(f_{i,}\, f_j)= H_2(f_j\, , f_{i,})$.

We confine the signal involved to be real-valued output process and use the symetric properties of the Fourier transform, $Y(f_m)$ with negative frequency index is complex conjugate, i.e. $Y(f_m) = Y^*(-f_m)$. Therefore, it is suffiecient to consider $Y(f_m)$ in Eq. (3.71) for only nonnegative frequencies. Expanding the summation term for theses nonnegative frequencies, Eq. (3.71) can be written in simplified notation.

In the Eq. (3.72), output frequencies associated with H_1 have the same as those of input, $X(m)$, while output frequencies involved with H_2 have created thorough interactions which dose not exist in input.

When m is odd, quadratic parts are expressed with half of the terms, but when m is even, there is a term contatinng $H_2(m/2,m/2)$ which cannot be incorporated for the reduction of terms. Thus, digital implementation becomes a little more complicated that we thought.

$$
\begin{aligned}
Y(m) &= H_1(m)X(m) \\
&+ \underbrace{\begin{matrix} H_2(m-M,M)X(m-M)X(m) + \cdots + H_2(-1,m+1)X(-1)X(m+1) \\ +H_2(0,m)X(0)X(m) \end{matrix}}_{\text{(a) difference frequencies interaction}} \\
&+ \underbrace{H_2(1,m-M)X(1)X(m-1) + \cdots + H_2(m-1,1)X(m-1)X(1)}_{\text{(b) sum frequencies interaction}} \\
&+ \underbrace{\begin{matrix} H_2(m,0)X(m)X(0) + H_2(m+1,-1)X(m+1)X(-1) + \cdots \\ +H_2(M,m-M)X(M)X(m-M) \end{matrix}}_{\text{(c) difference frequencies interaction}}
\end{aligned}
\tag{3.72}
$$

Thus, one can write (3.72) as follows:

$$
Y(m) = \begin{cases}
H_1(m)X(m) \\
\quad + 2\begin{bmatrix} H_2(\frac{m+1}{2},\frac{m-1}{2})X(\frac{m+1}{2})X(\frac{m-1}{2}) + \cdots + H_2(m-1,1)X(m-1)X(1) \\ + H_2(m,0)X(m)X(0) + \cdots + H_2(M,m-M)X(M)X(m-M) \end{bmatrix}, \\
\hfill \text{for } m \text{ odd}, \\
H_1(m)X(m) + H_2(\frac{m}{2},\frac{m}{2})X(\frac{m}{2})X(\frac{m}{2}) \\
\quad + 2\begin{bmatrix} H_2(\frac{m}{2}+1,\frac{m}{2}-1)X(\frac{m}{2}+1)X(\frac{m}{2}-1) + \cdots + H_2(m-1,1)X(m-1)X(1) \\ + H_2(m,0)X(m)X(0) + \cdots + H_2(M,m-M)X(M)X(m-M) \end{bmatrix}, \\
\hfill \text{for } m \text{ even}.
\end{cases}
\tag{3.73}
$$

Since Eq. (3.73) is linear with respect to the fransfer function H_1 and H_2, one can express Eq. (3.73) as a multiple-input single-output linear system (Kim and Powers, 1988; Birkelund and Powers, 2001)

$$
Y(m) = \begin{bmatrix} X(m) \\ X(\frac{m}{2}+1)X(\frac{m}{2}-1) \\ \vdots \\ X(m)X(0) \\ \vdots \\ X(M)X(m-M) \end{bmatrix}^t \begin{bmatrix} H_1(m) \\ 2H_2(\frac{m+1}{2},\frac{m-1}{2}) \\ \vdots \\ 2H_2(m-1,1) \\ \vdots \\ 2H_2(m,0) \\ 2H_2(M,m-M) \end{bmatrix}, \text{ for } m \text{ odd}
\tag{3.74}
$$

$$Y(m)=\begin{bmatrix} X(m) \\ X(\frac{m}{2})X(\frac{m}{2}) \\ X(\frac{m}{2}+1)X(\frac{m}{2}-1) \\ \vdots \\ X(m)X(0) \\ \vdots \\ X(M)X(m-M) \\ \\ \end{bmatrix}^t \begin{bmatrix} H_1(m) \\ H_2(\frac{m}{2},\frac{m}{2}) \\ 2H_2(\frac{m}{2}+1,\frac{m}{2}-1) \\ \vdots \\ 2H_2(m,0) \\ \vdots \\ 2H_2(M,m-M) \\ \\ \end{bmatrix}, \text{ for } m \text{ even.} \qquad (3.75)$$

In vector form,

$$Y(m)=\vec{X}^t\,\vec{H} \qquad (3.76)$$

where ^{t} denotes transpose

To solve this linear system in the transfer fucnion $\vec{H}$, one needs to mutilply $X^*(m)$ and $X^*(k)\,X^*(l)$, $k+l=m$, respectively to Eq. (3.76) and then take an expected value of each.

$$E\left[\vec{X}^*Y(m)\right]= E\left[\vec{X}^*\vec{X}^t\right]\vec{H} \qquad (3.77)$$

,where

$$\vec{X}^*(m)=\begin{bmatrix} X^*(m) \\ X^*(\frac{m}{2}+1)X^*(\frac{m}{2}-1) \\ \vdots \\ X^*(m)X^*(0) \\ \vdots \\ X^*(M)X^*(m-M) \end{bmatrix} \quad \text{or} \quad \begin{bmatrix} X^*(m) \\ X^*(\frac{m}{2})X^*(\frac{m}{2}) \\ X^*(\frac{m}{2}+1)X^*(\frac{m}{2}-1) \\ \vdots \\ X^*(m)X^*(0) \\ \vdots \\ X^*(M)X^*(m-M) \\ \\ \end{bmatrix}$$

$$\text{for } m \text{ odd} \qquad\qquad \text{for } m \text{ even}$$

Since Eq. (3.77) is also linear with respect to the transfer fucntion $\vec{H}$, the linear general solution of non-Gaussian input method obtained as (Kim and Powers, 1988)

$$\vec{H}=\left\{E\left[\vec{X}^*\vec{X}^t\right]\right\}^{-1}E\left[\vec{X}^*Y(m)\right] \qquad (3.78)$$

where $E[\vec{X}^{*}\vec{X}^{t}]$ is a Hermitian matrix consisting of various spectral moments of the input data and it may be expressed more explicity. For example, if m is even, $E[\vec{X}^{*}\vec{X}^{t}]$ has following from:

$$\left[\begin{array}{c|cccc} E\left[\left|X(m)\right|^{2}\right] & E\left[X^{*}(m)X(\frac{m}{2})X(\frac{m}{2})\right] & E\left[X^{*}(m)X(\frac{m}{2}+1)X(\frac{m}{2}-1)\right] & \cdots & E\left[X^{*}(m)X(M)X(m-M)\right] \\ \hline E\left[X^{*}(\frac{m}{2})X^{*}(\frac{m}{2})X(m)\right] & E\left[\left|X(m)\right|^{4}\right] & E\left[X^{*}(\frac{m}{2})X^{*}(\frac{m}{2})X(\frac{m}{2}+1)X(\frac{m}{2}-1)\right] & \cdots & \\ E\left[X^{*}(\frac{m}{2}+1)X^{*}(\frac{m}{2}-1)X(m)\right] & & E\left[\left|X(\frac{m}{2}+1)\right|^{2}\right]E\left[\left|X(\frac{m}{2}-1)\right|^{2}\right] & \cdots & \\ \vdots & & & \vdots & \\ E\left[X^{*}(M)X^{*}(m-M)X(m)\right] & & & \cdots & E\left[\left|X(M)\right|^{2}\right]E\left[\left|X(m-M)\right|^{2}\right] \end{array}\right] \tag{3.79}$$

In vector form,

$$E[\vec{X}^{*}Y(m)] = \begin{bmatrix} S_2^{yx} & \begin{bmatrix} \cdot & \cdot & S_3^{yx} & \cdot & \cdot \end{bmatrix} \end{bmatrix}$$

$$E[\vec{X}^{*}\vec{X}^{t}] = \begin{bmatrix} S_2^{xx} & \begin{bmatrix} \cdot & \cdot & S_3^{xx} & \cdot & \cdot \end{bmatrix} \\ \begin{bmatrix} \cdot \\ \cdot \\ \hat{S}_3^{xx} \\ \cdot \\ \cdot \end{bmatrix} & \begin{bmatrix} \cdot & \cdot & \cdot & \cdot & \cdot \\ \cdot & \cdot & \cdot & \cdot & \cdot \\ \cdot & \cdot & S_4^{xx} & \cdot & \cdot \\ \cdot & \cdot & \cdot & \cdot & \cdot \\ \cdot & \cdot & \cdot & \cdot & \cdot \end{bmatrix} \end{bmatrix} \tag{3.80}$$

$\hat{\hat{H}}$ = The estimated solution of the general Volterra model

S_2^{xx} = spectrum

S_3^{xx} = bispectrum
$\hat{S}_3^{xx}$ = conjugate of bispectrum
S_4^{xx} = trispectrum
S_2^{yx} = cross spectrum
S_3^{yx} = cross bispectrum

The inversion of input spectral momenet matrix, $E[\vec{X}^*\vec{X}^t]$ and the multiplication with $E[\vec{X}^*Y(m)]$ is significantly complicated and affected by the number of ensemble average over the data segment used because the variance of the trispectrum, s_4^{xx} estimate has higher variance than the power spectrum, s_2^{xx}. And the small variance of trispectrum gives better and stable solution. Ensemble average over data segment provides reasonable inversion results for $\{E[\vec{X}^*\vec{X}^t]\}$ with numerical stability.

This implies the estimated solution of the Vollterra model has close realtionhsip with the variace of input spectral momnets. Thus, we need to invert this matrix with small variance to computate better solution. In the next section, Principal component analysis will be inroduced to reduce a variance in the inversion of the spectral moment matrix.

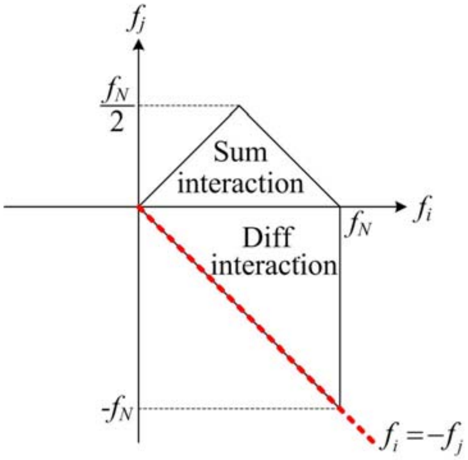

f_N: Nyquist frequency

Fig. 3.5 H_2 plane

It should be noted that this method dose not include frequencies along $f_i = -f_j$ in difference interaction region (**Fig. 3.5**) when H_2 is computed. H_1 corresponds to G_1 and H_2 to G_2 of Gaussian input method, respectively.

The non-Gaussian method necessarily involves division in the multiplication of the inverse input spectral momenet matrix, $E[\vec{X}^*\vec{X}^t]$ and $E[\vec{X}^*Y(m)]$ like the Gaussian method. Consequently, the large diverging magnitude of QTF occurs in some parts of H_2 plane due to the large numerator compared to the small denominator (tails of input energy spectra) in the division process. In this method, the unrealistic QTF should be accurately eliminated as done in the Gaussian method. This process could lose some true QTF.

3.4. Principal Component Analysis (PCA)

If the estimated input spectral matrix $\underline{A}$ contains some linearly dependent columns as a result of the high variance in the estimate, the determinant will be zero and no inverse matrix exists. Similarly, if some of the columns are nearly dependent, there will be eigenvalues close to zero, and the matrix inversion is numerically unstable (Johnson and Wichern, 1998). This is in fact the main problem with estimating the Volterra model using the non-Gaussian input assumption.

The input spectral moment matrix is Hermitian, $\underline{A} = \underline{A}^H$, so that one can represent the unitary decomposition of $\underline{A}$ as (Scharf, 1991)

$$\underline{A} = \underline{U}_r \underline{\Lambda}_r \underline{U}_r^H = \sum_{i=1}^{q} \lambda_i u_i u_i^H \tag{3.81}$$

Here λ_i are nonnegative real eigenvalues with corresponding eigenvector u_i, $\underline{\Lambda} = diag\{\lambda_1, \lambda_2, \cdots, \lambda_q\}$, and $\underline{U} = diag\{u_1, u_2, \cdots, u_q\}$. The eigenvalues are further required to be ordered as $\lambda_1 \geq \lambda_2 \geq \cdots \geq \lambda_q$. The low rank approximation of $\underline{A}$ formed, using only the r largest eigenvalues and their corresponding eigenvectors, can be written as (Scharf, 1991; Johson and Wichern, 1998)

$$\underline{A}_r = \underline{U}_r \underline{\Lambda}_r \underline{U}_r^H = \sum_{i=1}^{r} \lambda_i u_i u_i^H \tag{3.82}$$

where the error $e^2 = \sum_{i=r+1}^{q} \lambda_i^2$ is the sum of the squares of all elements in $(\underline{A} - \underline{A}_r)$.

If we choose to use only those components satisfying $\lambda_i > \alpha\lambda_1$, where $\alpha << 1$ is chosen appropriately, we have efficiently removed the effect of all small eigenvalues. The resulting low rank matrix can not have (nearly) linear dependent eigenvectors, and inverse matrix can be written as (Johson and Wichern, 1998)

$$\underline{A}_r^{-1} = \underline{U}_r \underline{\Lambda}_r^{-1} \underline{U}_r^H = \sum_{i=1}^{r} \frac{1}{\lambda_i} u_i u_i^H \tag{3.83}$$

Since $\underline{U}_r$ is a unitary matrix $(\underline{U}_r^{-1} = \underline{U}_r^H)$. The formation in Eq. (3.83) is numerically stable.

The r^{th}-order low rank matrix in Eq. (3.82) is the least squares best approximation to $\underline{A}$ in an r dimensional subspace of the true $\underline{A}$. The use of only the largest eigenvalues ensures that the main variation of the original matrix is preserved.

For noisy estimates the use of $\underline{A}_r^{-1}$ instead of $\underline{A}^{-1}$ in the estimation of the Volterra model in $\hat{H}(f_m) = B(f_m)\underline{A}^{-1}(f_m)$, will remove nearly linearly dependent columns but may also affect the true variation in $\underline{A}$. This leads to some bias in the estimated the Volterra kernel, but considering the numerical problem related to the full matrix inversion this bias is tolerable. For reasonably noise-free estimates, the principal component analysis will not alter the original input spectral matrix and the resulting the Volterra model will be similar to the one obtained through use of the full matrix in the inversion.

The PCA method depends on the choice of the order r. For the data in this study, the (empirical) choice $\lambda_i > \lambda_1/1000$, leads to an order-$p$ which remove the noise induced invertibility problem (Birkelund , 2001; Birkelund et al. 2003).

CHAPTER IV

CASE STUDY

In this chapter, the Gaussian and non-Gaussian methods will be applied to the analysis of three different experiments. Sea states in these experiments range from the rough to the phenomenal seas. The data to be examined are the following:

Surge force on fixed barge at various sea states

A series of model test were conducted to find the effect of sea severity and the record length on the estimation of the linear and quadratic frequency response functions for the surge wave exciting forces on a barge tested in a wave tank. Using sea waves of significant wave height: 3m and 9m, the surge wave exciting forces were measured (Kim and Kim, 2002, 2003, 2004).

Surge motion of a compliant Mini TLP

1:40 scale model test of Mini-TLP was carried out in the wave basin of the Offshore Technology Research Center located at Texas A&M University. The surge drift resonance frequency was at 0.007Hz (0.044 rad/s). A 10-year return storm sea in Africa (Hs=3.99m, f_p = 0.07Hz) was used (Liagre, 2000; Niedzwecki et al, 2001; Birkelund et al, 2003).

Surge force on a fixed and truncated column

Surge force on a vertical truncated cylinder in irregular waves was measured in the wave basin of the MARINTEK (diameter is 0.625m in model scale of 1:55). The model corresponds to a 100-year storm. The cylinder Sea state is Hs=15.4m, T_p=17.5sec, and JONSWAP, γ=1.7 in full scale (Stansberg et al. 1995).

4.1. A fixed barge in rough and high seas

The Gaussian and non-Gaussian methods will be applied to rough sea (Hs=3 m) and high seas (Hs=9 m), and the differences of both methods will be compared. In addition, the effect of data length will be included (Kim and Kim, 2002, 2003, 2004).

4.1.1. Experimental setup

The wave tank is 37 m long, 0.91 m wide, and 1.22 m deep and is equipped with a Commercial Hydraulic RSW 90-85 dry-back, hinged-flap wavemaker, and a downstream wave-energy absorbing beach. The still water depth is kept constant at 0.88 m.

The wavemaker is made by SEASIM. The electro-mechanical components are operated in the frequency range of 2.0 rad/s~12.0 rad/s, and voltage range of ±1.5 volts. The outboard switches of the driving signal (analog) for the wavemaker are set for a range of ± 1.5 volts to match with the frequency of the wavemaker. The wavemaker is driven by the analog signal obtained from the computed digital signal, through the Strawberry Tree Digital to Analog (D/A) board installed in the computer for running the wavemaker. The voltage limits have recently been changed from the previous ±5.0 volts to ± 1.5 volts to prevent the fatigue-induced damage of the old wavemaker due to an unexpected excessive motion.

Resistance-type wave gauges are used to measure wave surface elevations. The accuracy of the wave gauge is ±0.1 cm. The horizontal wave force is measured by an ARCTEC strain gauge platform with a capacity of 178 N, the accuracy of which is ±1.0 % of the applied force. The scanning rate of measuring the wave and force is 50 Hz.

The location of the design waves is at 20 m down the tank from the flap, where we set up the barge was set up with the wave gauge as shown in **Fig. 4.1** to measure the horizontal forces and wave elevation simultaneously. The distance is chosen so as to avoid the wave reflection from both ends of the tank during the measuring time period of 30 seconds. The barge, which is made of wood, is 0.758 m long, 0.296 m wide and 0.2 m deep. The draft of the barge is chosen as 0.08 m. The barge model is attached to the ARCTEC platform dynamometer, which is fixed to the frame on the tank top. Froude similitude law was applied with length scale ratio of 1/100. The measuring time step used is 0.02 second for the model.

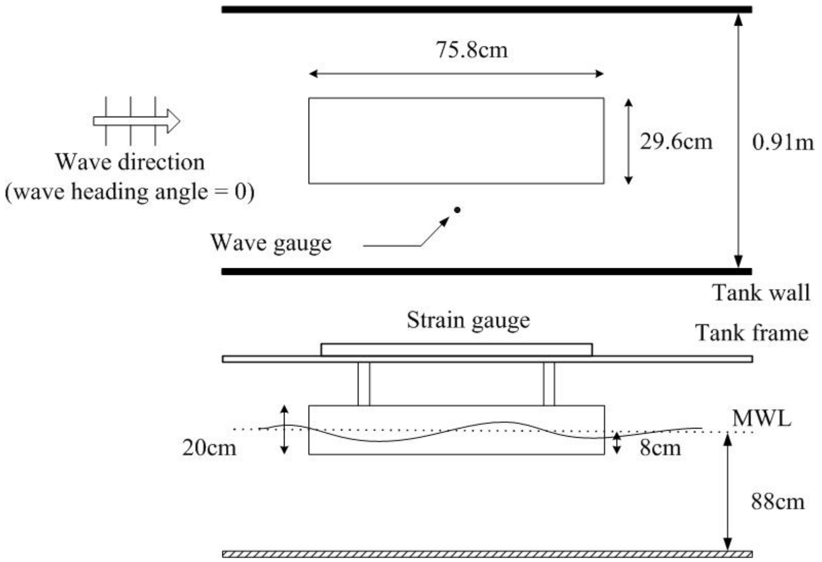

Fig. 4.1 Model setup for wave and force measurement

4.1.2. Time series of wave and surge force on a barge

In this experiment, 40 random wave data sets were generated to have statistical convergence (Kumar and Kim, 2002). The target spectra are P-M spectra: Hs=3 m, ω_m (modal frequency) = 0.525 rad/s; Hs=9 m, ω_m =0.425 rad/s. The ensemble of the wave data was made by connecting each record in a series. Each finite clean record is 30 seconds long; thus, it needed to have 12 segments to make 360 seconds for the model, which corresponds to 1 hour for the prototype.

The input wave and the output surge force time series of Hs=3m and 9m, as an example, that were measured simultaneously, are shown in **Fig. 4.2** and **Fig. 4.3**. Comparing the peaks of the wave and force at the same instant, the phase of surge peak force leads the wave peak an average about 90 degrees, as expected.

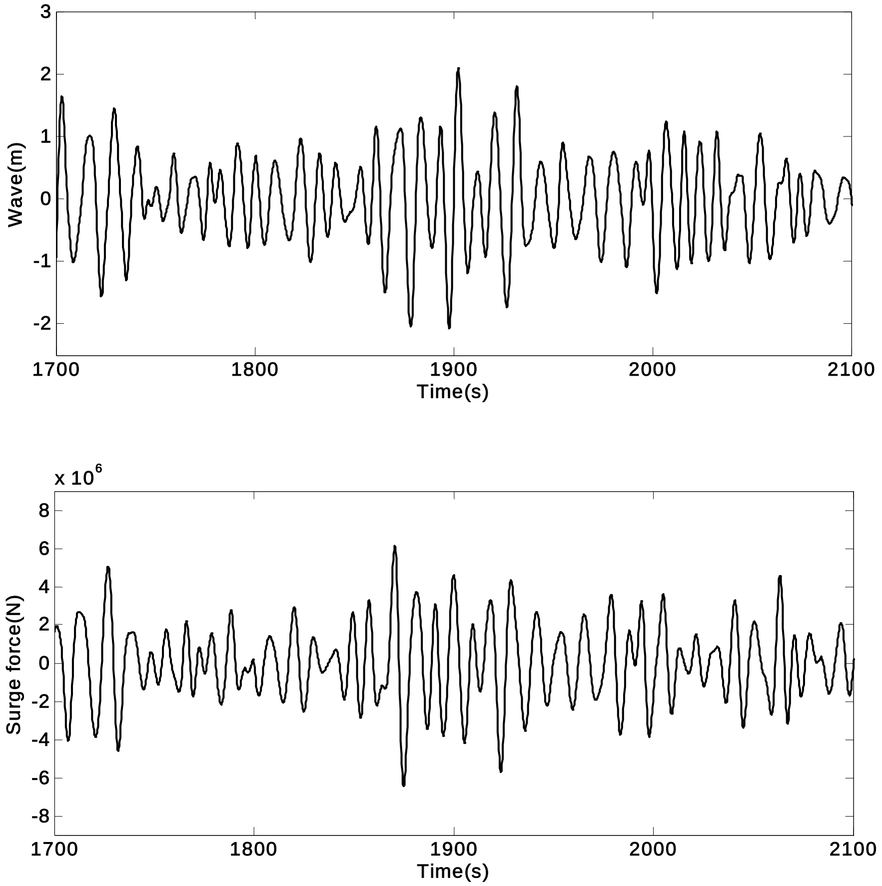

Fig. 4.2 Time series of waves (top) and surge forces (bottom) at Hs=3m

Amplitudes of surge force Hs=3 m appear to be symmetrical around zero. On the other hand, those of Hs=9 m seem to be shifted upward, which means that the high sea contains more nonlinear effects. Surge forces at Hs=9 m appear to have strong groups or transient effects in its time series unlike at Hs=3 m. This also indicates nonlinear effects in a high sea state.

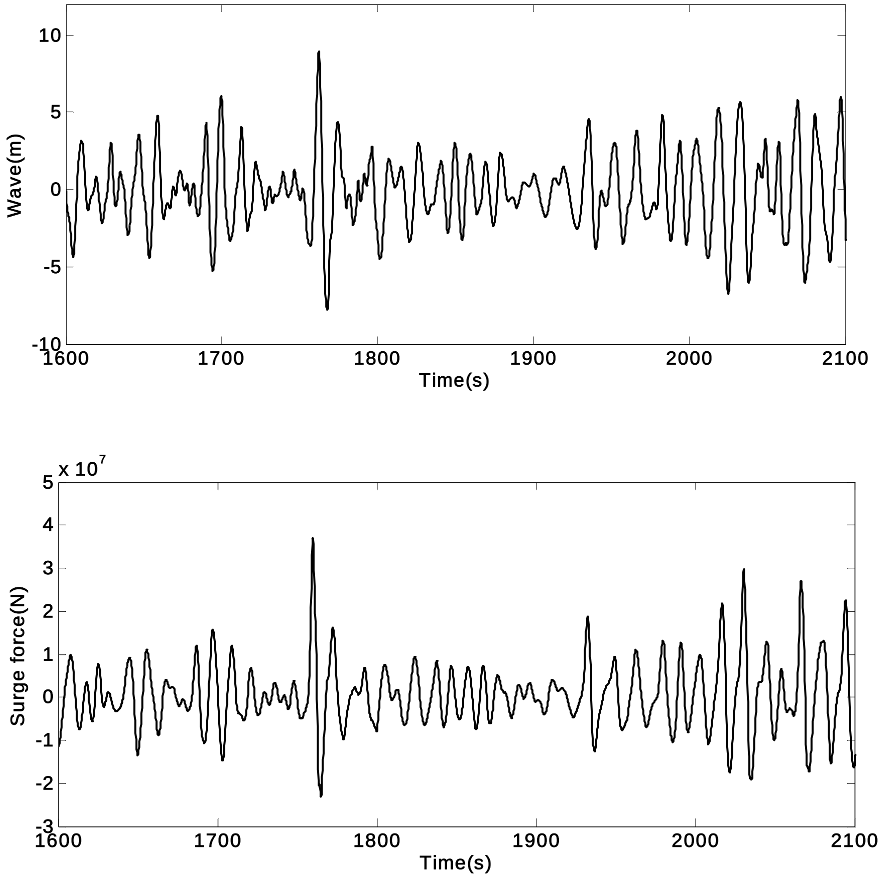

Fig. 4.3 Time series of waves (top) and surge forces (bottom) at Hs=9m

Contrary to expected wave statistics, the mean of waves is negative (**Table 4.1** and **Table 4.2**), whereas surge forces are positive in the time series. This is a contribution of the depression due to the 2nd-order nonlinear effects in waves (Kim, 2005**)**. The depression is induced by the 2nd-order difference frequencies interaction and is called set-down. The depression gets stronger as the sea state gets higher; the 2nd-order nonlinearity becomes stronger. The wave and surge force at Hs = 9 m have a bigger deviation from 0 or 3 for skewness and kurtosis than those of Hs = 3 m (**Table 4.1** and **Table 4.2**), respectively.

Table 4.1 Statistics of waves and surge forces at Hs = 3 m

	Mean(m)	Skewness	Kurtosis
Wave	-0.012	0.011	2.949
Surge force	5.676×10^4	0.074	2.970

Table 4.2 Statistics of waves and surge forces at Hs = 9 m

	Mean(m)	Skewness	Kurtosis
Wave	-0.036	0.038	3.119
Surge force	3.361×10^5	0.278	3.701

4.1.3. The effect of sea severity on statistics of measured waves

Fig. 4.4 shows the probability density of wave elevation and the distribution of crest height compared with the Gaussian and Rayleigh distributions, respectively.

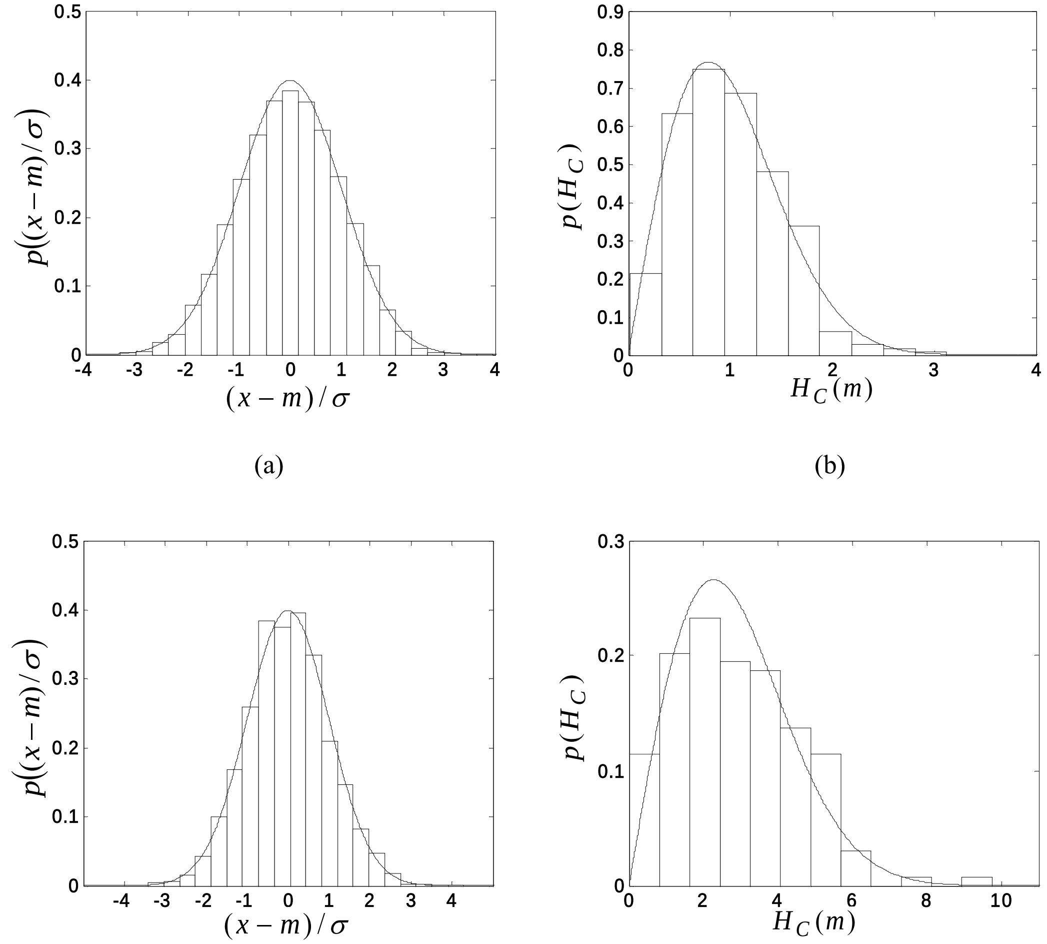

(a) (b)

(c) (d)

Fig. 4.4 Probability density of wave elevation (a, c) and distribution of crest height of waves (b, d)
(a) and (b) at Hs=3m, (c) and (d) at Hs=9m

The wave of Hs = 3 m agrees well with Gaussian and Rayleigh distributions. Thus, the waves considered to be linear random waves. As the significant wave height increases, the experimental data deviates increasingly from the Gaussian and Rayleigh distributions (Kim and Kim, 2003). The wave of Hs=9 m appears to be the nonlinear wave. The probability of exceedance of the crest heights is compared with the Rayleigh distributions in **Fig. 4.5**. The wave of Hs=3 m appears to be nearly linear wave, and the wave of Hs=9 m seems to be nonlinear, as expected.

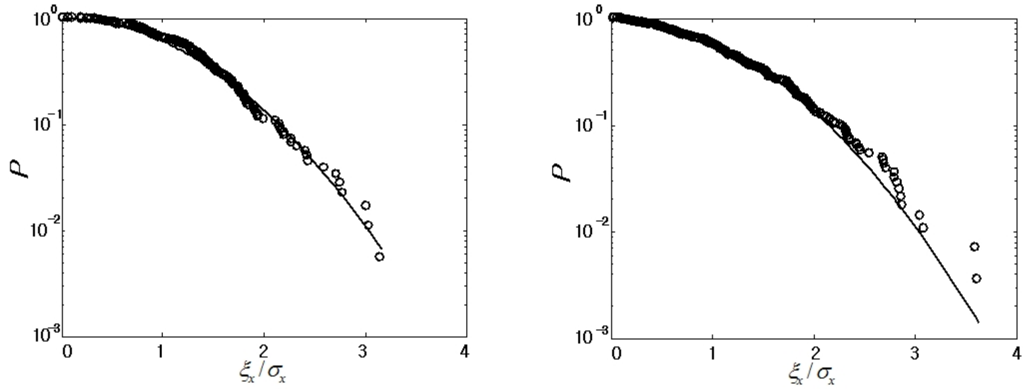

Fig. 4.5 Rayleigh distribution compared with the probability of exceedence of positive peak of waves; at Hs=3m (left) and Hs=9m (right)

4.1.4. Convergence of mean surge force

Since the convergence of the mean 2nd-order force is so important and fundamental in the analysis of the 2nd-order response, the variation of mean surge force is displayed for two different sea states. The result of the mean values averaged with moving scheme or the cumulative time average is shown in **Fig. 4.6**. The cumulative time average is defined:

$$\bar{y}_{cum}(t_N) = \frac{1}{N}\sum_{i=1}^{N} y(t_i) \tag{4.1}$$

The mean surge force at 3 hours of duration shows much different values than those at 30 hours duration. It should be noted that the mean force varies until about 30 hours (**Fig. 4.6**). In other words, a long data is required to analyze and find the convergence of the 2nd-order mean force, specifically, for such sea states, structures and modes of force as measured in the specified wave tank. This mean force behavior is similar to the numerical simulation of mean drift force in beam seas by Kim and Boo (1990) that converges after 15 hours.

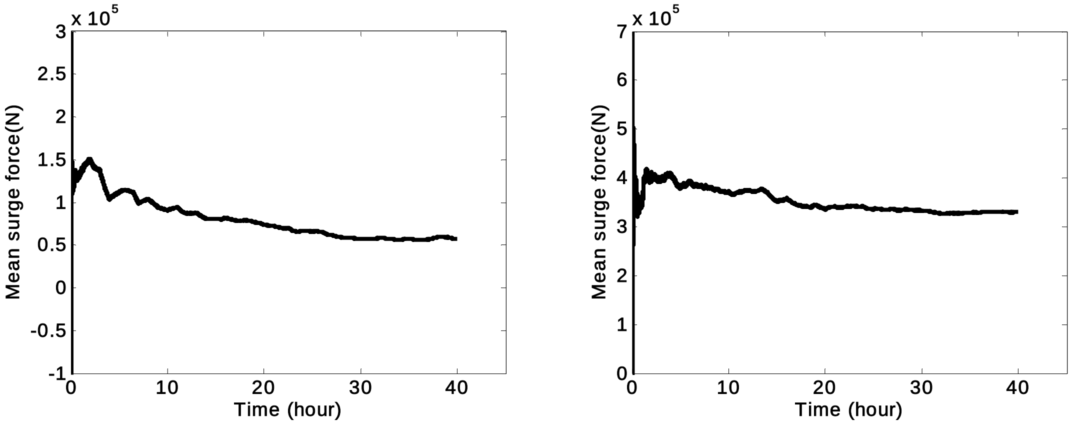

Fig. 4.6 Cumulative mean of surge force at Hs =3m (left) and Hs=9m (right)

4.1.5. Measured wave spectrum

Fig. 4.7 shows the spectra of measured waves which are based on the target spectra, P-M spectra: Hs=3 m, ω_m (modal frequency) =0.525 rad/s; Hs=9m, ω_m =0.425 rad/s.

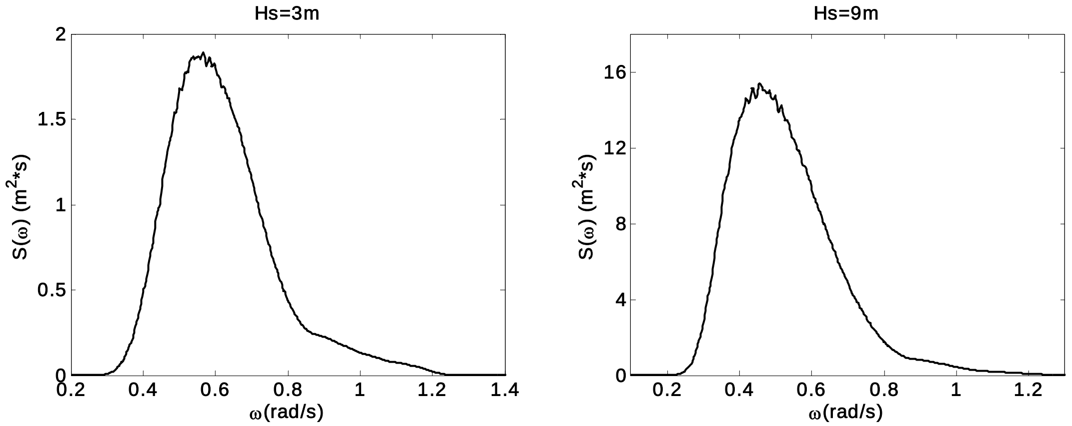

Fig. 4.7 Wave spectra of Hs=3m (left) and Hs=9m (right)

4.1.6. Linear transform function and Quadratic transfer function

As the first step of investigation of the sea severity and data length, the linear transfer function was compared at different sea states with different data lengths. In both sea states, LTFs with a short data length seem to be less smooth, and, LTFs get smoother with a longer data length in **Fig. 4.8**.

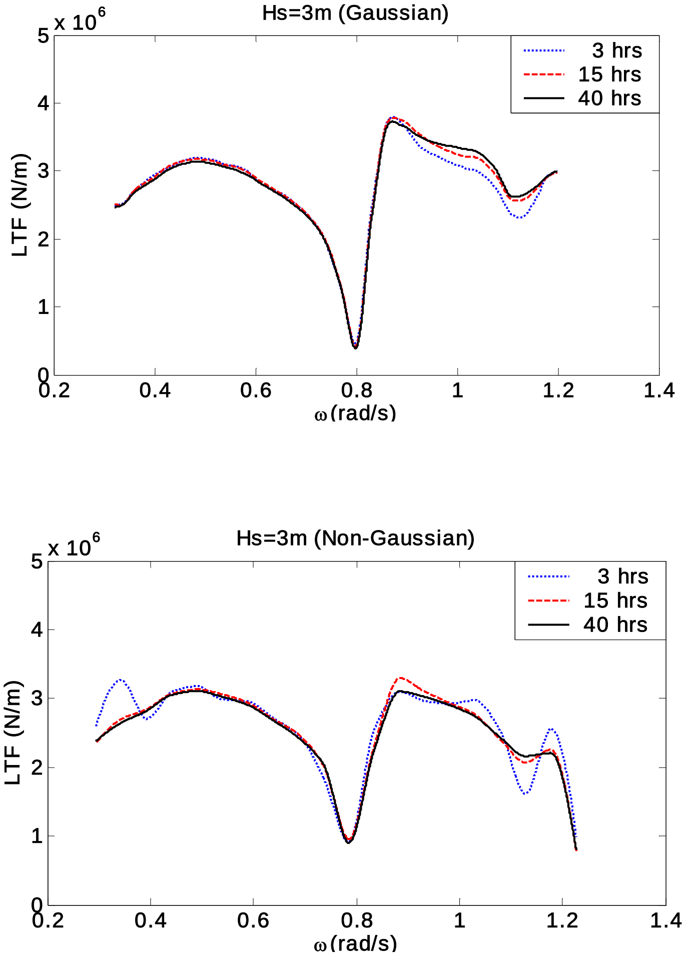

Fig. 4.8 Effects of data length on LTFs

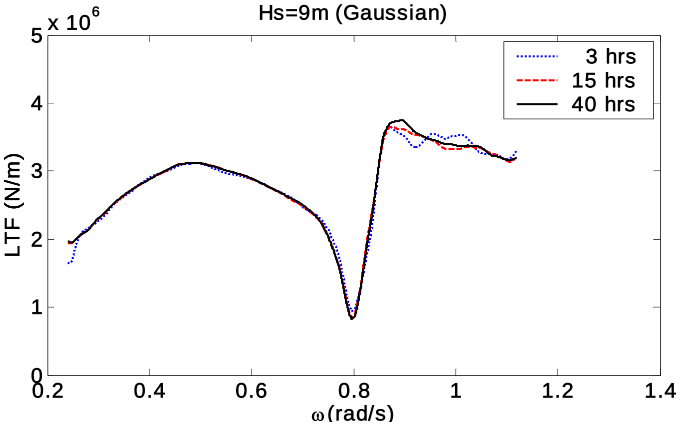

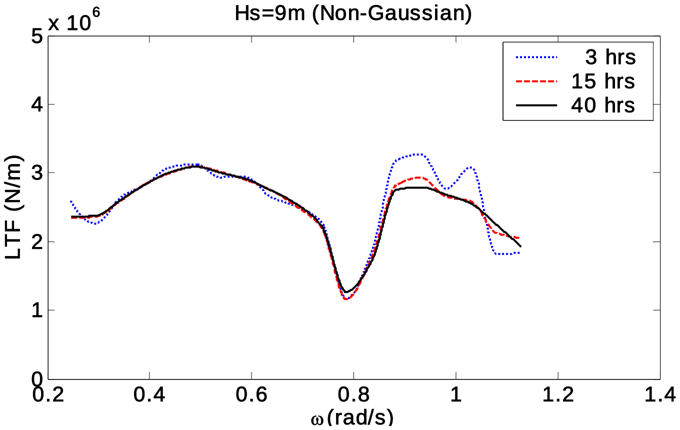

Fig. 4.8 Continued

The estimated LTFs with 40-hour data were compared to see the effects of sea severity and difference of methods in **Fig. 4.9**. In the Gaussian method, LTFs are in fairly good agreement, while, in the non-Gaussian method, LTFs show a discrepancy in high frequency region, higher than 0.8 rad/s. It is noticed that the non-Gaussian method is much sensitive to sea states than the Gaussian method.

Although the LTF is a system characteristic, the estimated LTFs depend on the sea severity.

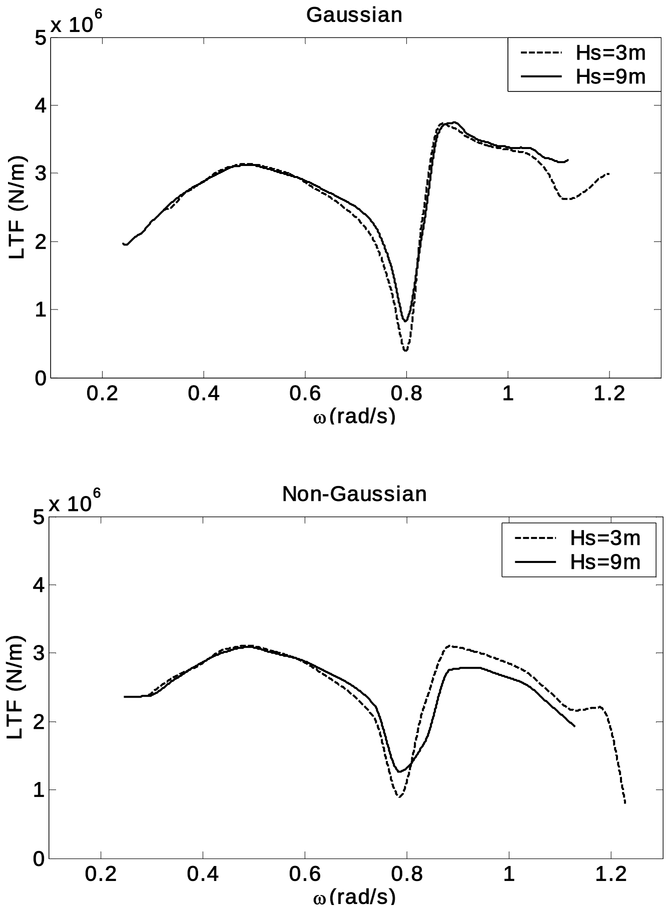

Fig. 4.9 Effects of sea severity on LTFs

In general, QTFs are more sensitive and complicated than LTFs. In the Gaussian method, each 1-hour data was computed and the ensemble average was made over several hours of data to obtain the QTF, which means, for instance, that the QTF of 3-hour data is the ensemble average of 3 QTFs from each 1-hour data. In this computation, the 70 of maximum lag was used. It should be noted that the shapes of QTF have two bumps near the sum and difference frequency axes. Also, we see that the effect of data length on QTFs estimated with the Gaussian assumption appears to be negligible in **Fig. 4.10** and **Fig. 4.11**.

The non-Gaussian method is modified with the principal component analysis algorithm, which yields considerably lower variance in the estimation of the Volterra model (Birkelund et al., 2003). In the non-Gaussian method, both input and output data have been decimated by a factor R=5. After the down-sampling, the time step becomes one second, and the maximum frequency, $\omega_{\max} = 2\pi$ rad/s, is large enough to cover the 2nd-order frequency range associated with input frequency components. The segment length is chosen to be 128. Hence, the number of segments in 3, 15 and 40 hour data are 84, 421, and 1125, respectively. It was found that QTFs estimated from the non-Gaussian method are affected significantly by the data length, which contrasts to the Gaussian method shown in **Fig. 4.10** and **Fig. 4.11.**

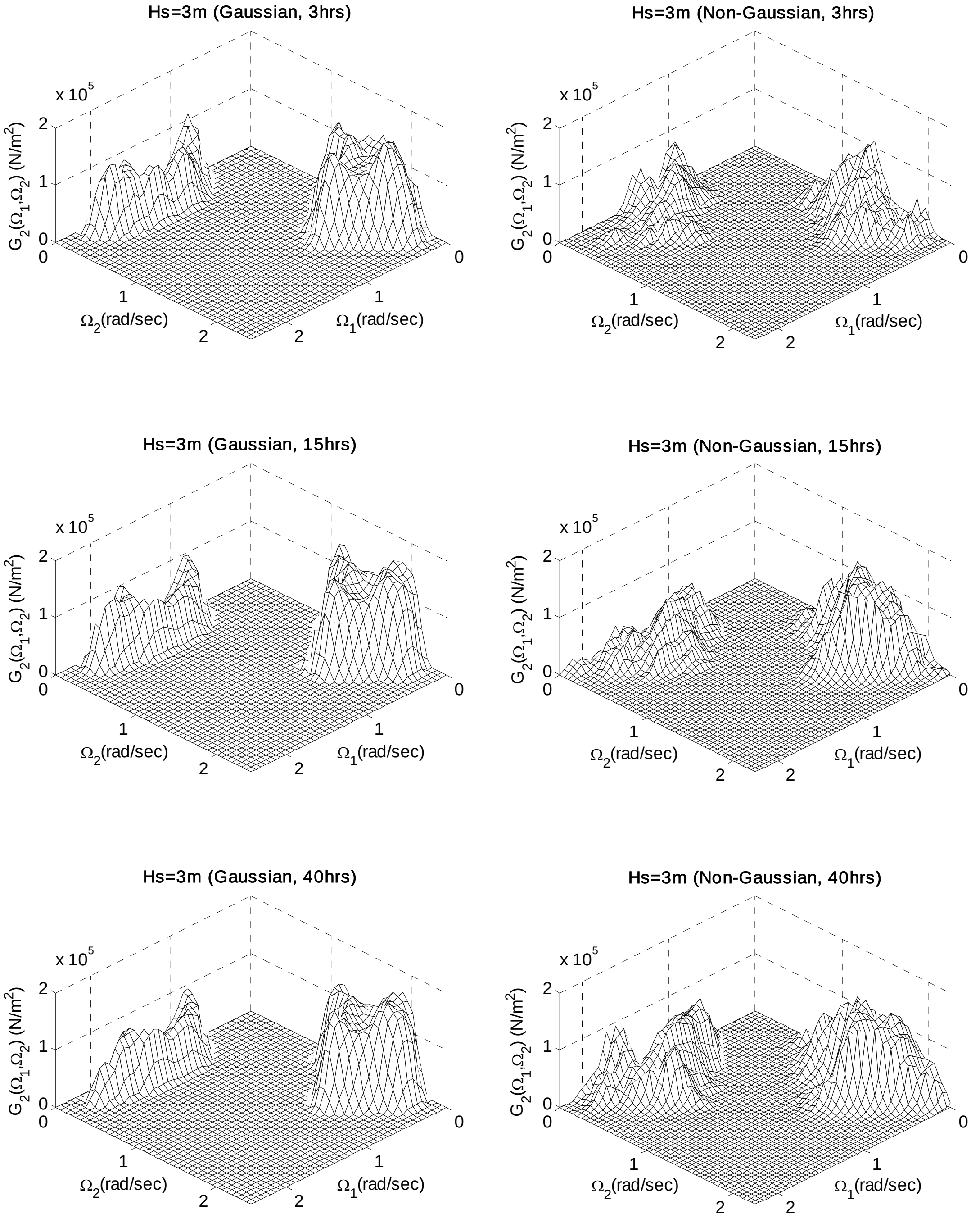

Fig. 4.10 Estimated QTFs by the Gaussian and non-Gaussian methods at Hs=3m

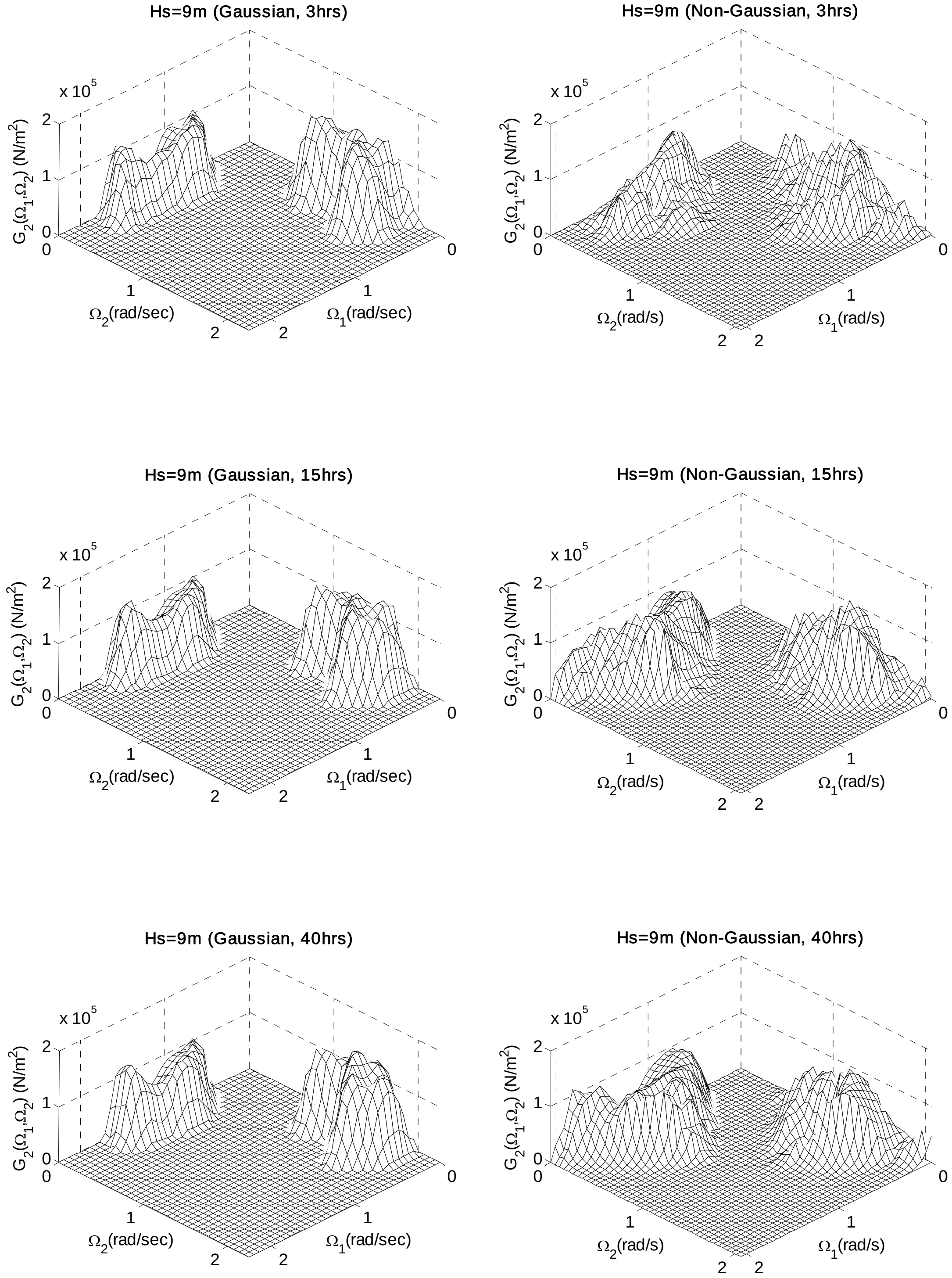

Fig. 4.11 Estimated QTFs by the Gaussian and non-Gaussian methods at Hs=9m

4.1.7. Dependency of normalized mean force on sea states

The normalized mean surge force can be obtained from the estimated QTFs. The normalized mean surge force values are distributed on the Ω_1–axis (Ω_2=0) in the G_2 plane. It should be noted that the non-Gaussian method does not include frequencies along the Ω_1–axis as explained in chapter 3. Thus, the closest parallel frequency line ($\Omega_2 \approx 0$) to the Ω_1–axis was chosen as an alternative way.

The normalized mean surge force at high sea is always higher than at low sea, except the case (b) in **Fig. 4.12** that seems to be induced by a short data length. Even though, the normalized mean force is one of the system characteristics and should be theoretically independent of sea state, it varies with the sea states in reality. This fact also was found in the model test with a moored semi-submersible (Stansberg, 2001).

The dependency of mean force on sea states may be interpreted as effects from viscous forces (which are most important for long waves) or other experimental limitations. Hence, it needs to be analyzed more in future with CFD or potential theory, etc.

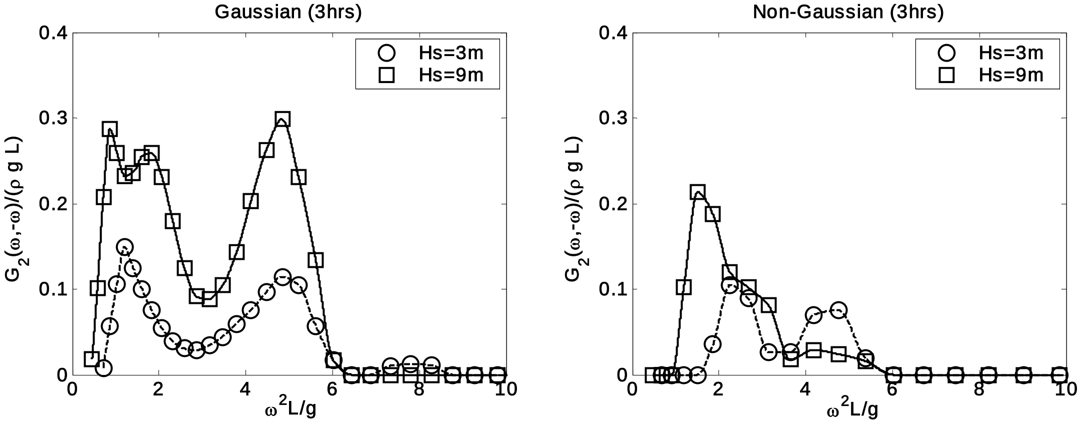

Fig. 4.12 Normalized mean drift force (ρ=water density, g= acceleration of gravity, and L= length of barge)

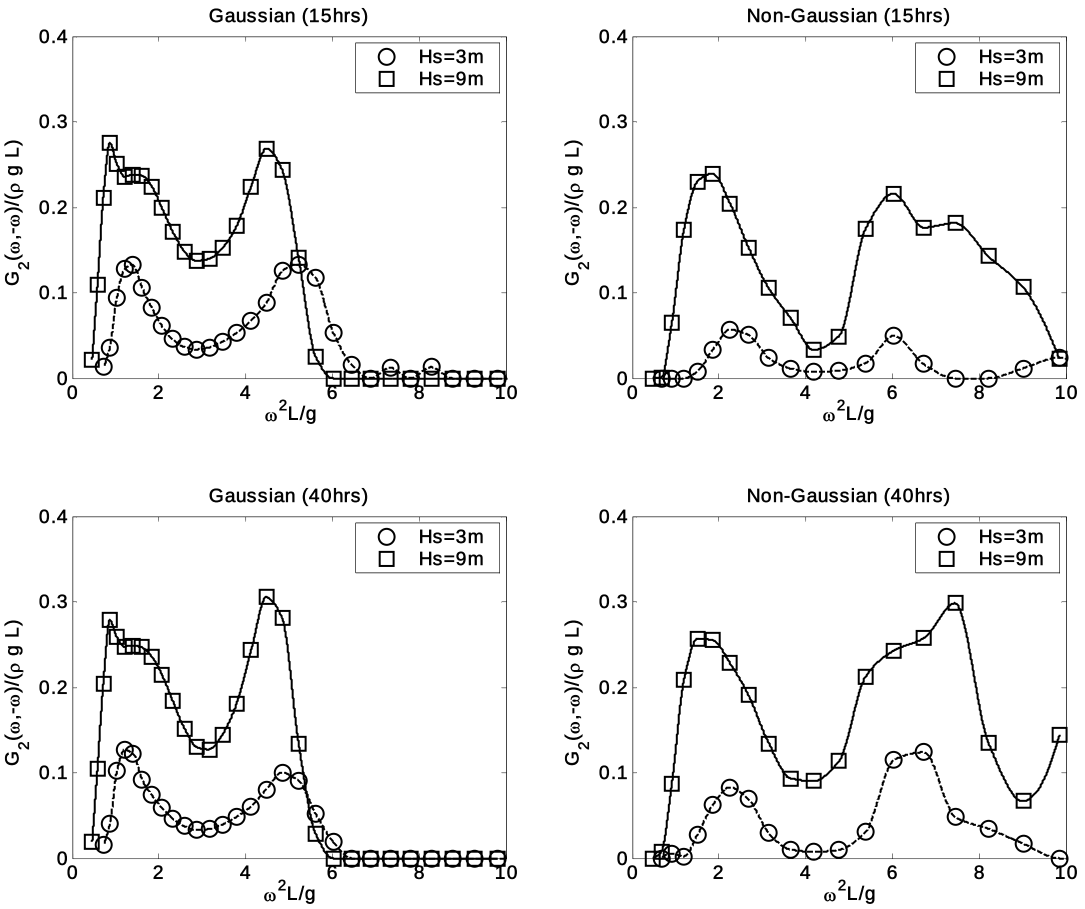

Fig. 4.12 Continued

4.1.8. Reconstruction

In order to evaluate the quality of LTFs and QTFs estimated by the Gaussian (Dalzell, 1976) and non-Gaussian methods (Kim and Powers, 1988), one needs to compare the measured and reconstructed data in time domain, which may be performed using the reconstruction procedure. Referring to **Fig. 4.13**, one identifies first the estimated LTFs and QTFs, which will be used in the next step with the previously measured nonlinear random wave data in Eq. 3.18 to reconstruct the output.

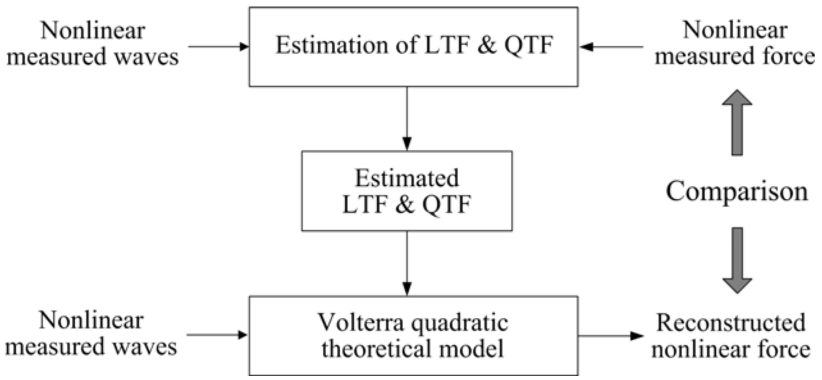

Fig. 4.13 Schematic diagram for reconstruction

Fig. 4.14 illustrates comparisons of the measured and reconstructed time series of outputs for the Gaussian and non-Gaussian methods, respectively. It should be noted that the effects of sea severity are significant, as seen in (b) **Fig. 4.14**. The agreement of the time series at higher sea (Hs = 9m) is less favorable than that at the lower sea (Hs = 3m).

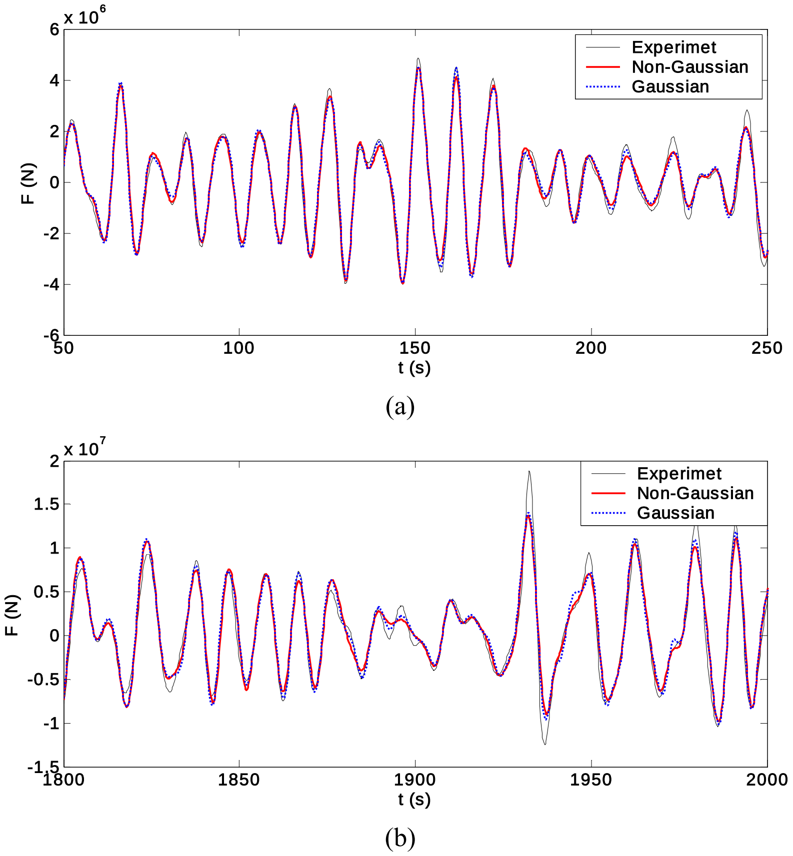

Fig. 4.14 Comparisons of time series with (a) the Gaussian method with 40-hour data at Hs=3m and (b) the non-Gaussian method with 40-hour data at Hs=9m

The 2nd-order forces are extracted from the measured data in **Fig. 4.15**. The amplitudes of 2nd-order forces at Hs=9m is much stronger than at Hs=3m, and the differences of both methods are more distinctive at Hs=9m; the amplitudes and periods of the Gaussian method seem to be similar to those of the non-Gaussian method at Hs=3m but appear to be much different at Hs =9m.

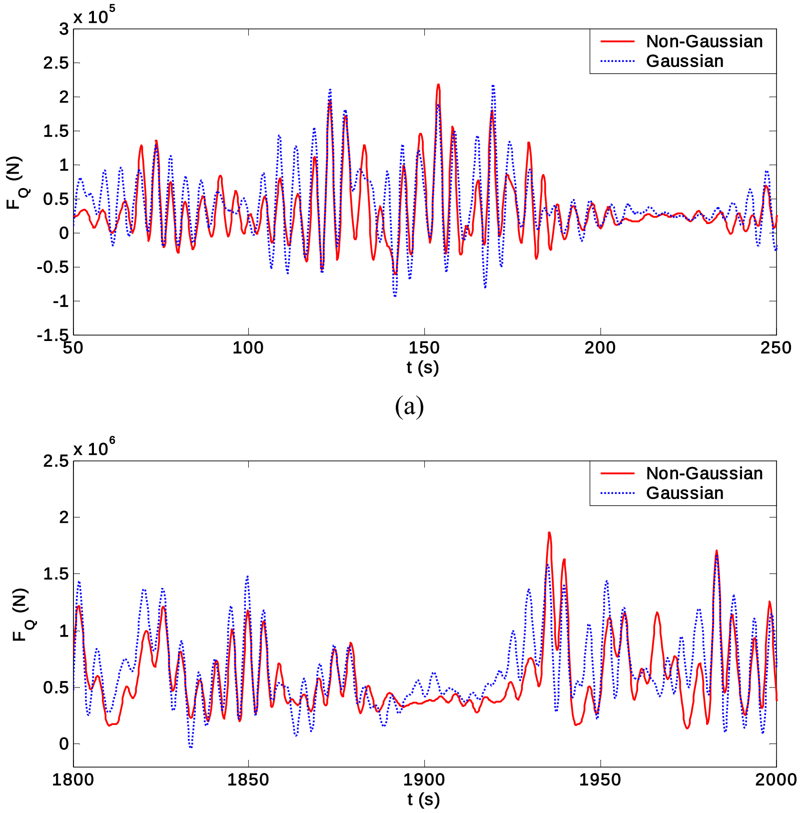

(a)

(b)

Fig. 4.15 Comparisons of extracted quadratic time series with (a) the Gaussian method with 40-hour data at Hs=3m and (b) the non-Gaussian method with 40-hour data at Hs=9m

4.1.9. Normalized mean square error

To compare the quality of the estimations, the normalized mean square error (NMSE) was used to compare the measured and reconstructed time series statistically:

$$\mathrm{NMSE} = \sqrt{\frac{\frac{1}{N}\sum_{t=1}^{N}\left\{[x_{\mathrm{rec}}(t)-\overline{x}_{\mathrm{rec}}(t)]-[x_{\mathrm{exp}}(t)-\overline{x}_{\mathrm{exp}}(t)]\right\}^{2}}{\frac{1}{N}\sum_{t=1}^{N}[x_{\mathrm{exp}}(t)-\overline{x}_{\mathrm{exp}}(t)]^{2}}} \tag{4.2}$$

where N is the number of data, $x_{\mathrm{rec}}(t)$ is the constructed time series, and $x_{\mathrm{exp}}(t)$ is the experimental time series.

The NMSE is computed to compare the reconstruction with the raw experimental data and the experimental data filtered by eliminating the frequency components higher than 4 rad/s, which may be regarded as noise.

NMSE (**Table 4.3**) is lower at Hs = 3m than at Hs = 9m, and the differences, due to the use of the Gaussian and non-Gaussian methods, are very small, which implies that the estimation of the response is better for the low sea than for the high sea.

Table 4.3 Comparison of NMSE with filtered experimental data

	Hs = 3m		Hs =9m	
	Gaussian method	Non-Gaussian method	Gaussian method	Non-Gaussian method
3 hours	0.178	0.184	0.270	0.277
15 hours	0.184	0.189	0.272	0.282
40 hours	0.184	0.193	0.273	0.283

4.1.10. Surge force Amplitude Spectrum

Time domain data is expressed in the amplitude spectra shown in **Fig. 4.16**. Amplitude spectra of the measured and reconstructed surge force are in good agreement at the state of low sea severity, Hs=3 m, compared to those in the state of high sea severity, Hs = 9 m.

In regards to the data length, spectra of reconstructed surge forces get close to those of measured surge forces in the low frequency region, as the data length becomes longer, which implies that longer data contains more slowly varying effects in the time series and their corresponding effects on the barge.

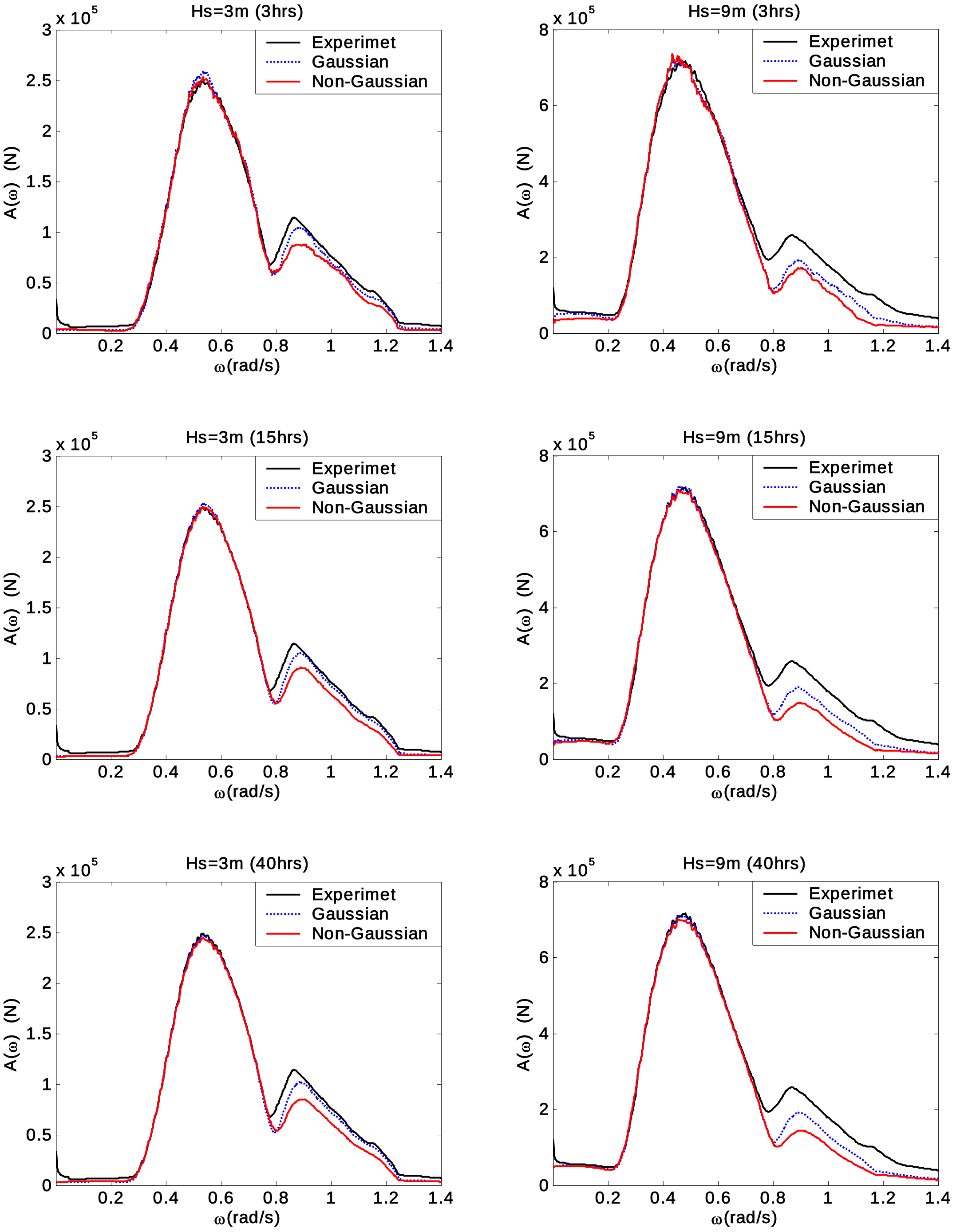

Fig. 4.16 Comparison of surge force amplitude spectra between measured and reconstructed time series

The slowly-varying effects in the magnified spectra are more clearly shown in **Fig. 4.17**. The spectra in the low-frequency region illustrates that the slowly-varying surge forces are more extracted at high sea because the 2nd-order slowly-varying signals are stronger.

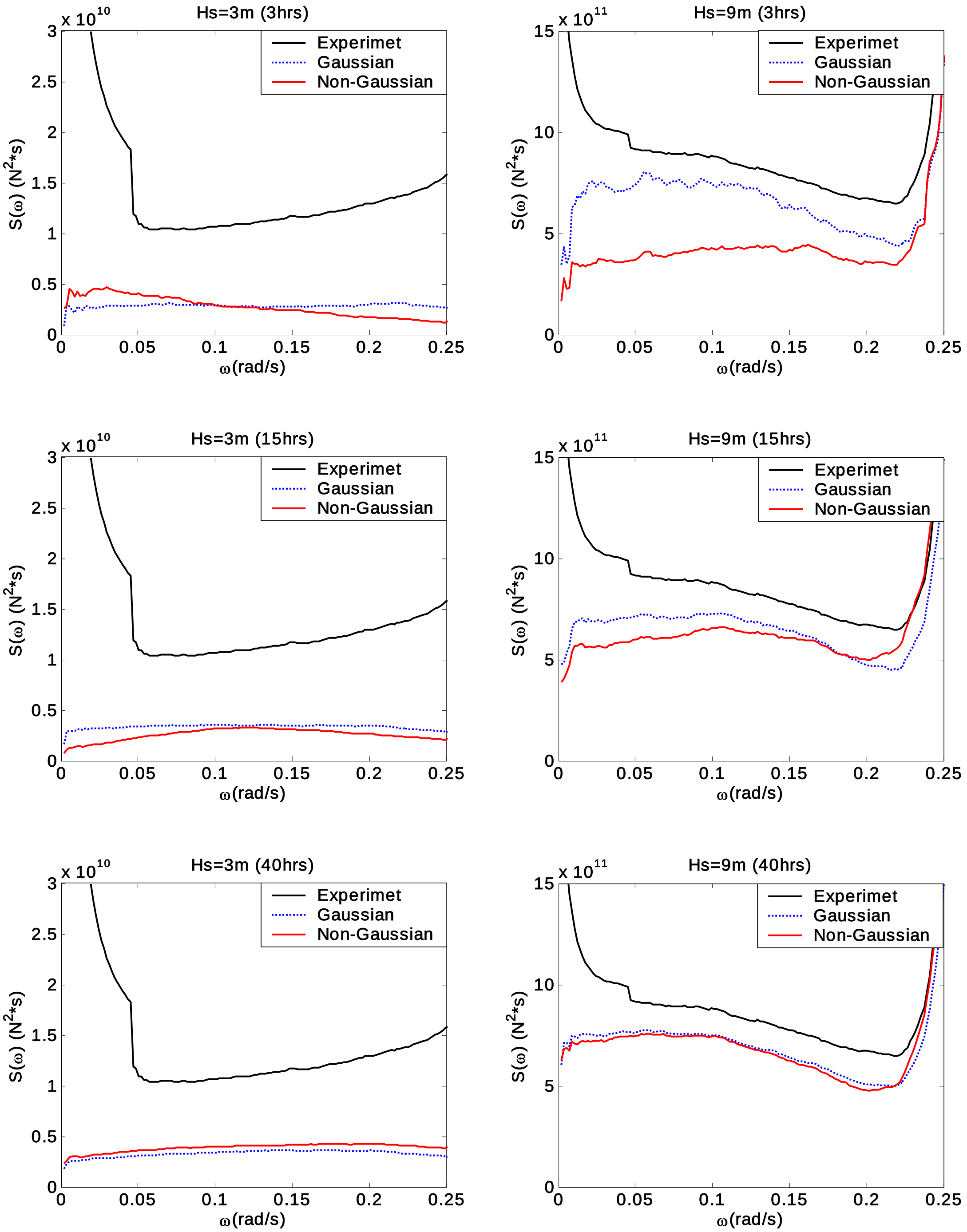

Fig. 4.17 Comparison of surge force spectra between measured and reconstructed time series at low frequency region

4.1.11. Comparisons of coherency

The reconstructed data and measured data are used for the coherency test. The linear and quadratic coherence functions are defined (Bendat, 1990):

$$\gamma^2_{xy_1}(\omega) = \frac{U_{y_1y_1}(\omega)}{U_{yy}(\omega)} \tag{4.3}$$

$$q^2_{xy_2}(\omega) = \frac{U_{y_2y_2}(\omega)}{U_{yy}(\omega)} \tag{4.4}$$

,where eq. (4.3) and (4.4) represent the linear and quadratic coherence function, respectively. U indicates one-sided energy density spectra. The suffixes y_1 and y_2 stand for the reconstructed linear and quadratic output, respectively, and y denotes the measured output. The sum of these coherence functions should lie in between 0 and 1. A goodness-of-fit measure for the validity of the quadratic nonlinear model can be defined by seeing how close the sum of these linear and quadratic coherence function to unity is (Bendat, 1990). Comparing **Fig. 4.18** and **Fig. 4.19**, the coherency test shows the dependency of the sea severity and record length.

Concerning the effects of sea severity, at the low sea state of Hs = 3m, the linear coherency seems to good in the frequency range, 0.2-1.2 rad/s, while the quadratic coherency is about 0.3 in the frequency range of 0-0.2 rad/s and 0.3 in the range 1.2-1.4. This means that, since the 2nd-order surge force signal was weak at the low sea state, the extraction of linear responses is trustworthy, but, the extraction of the 2nd-order nonlinear responses is not at the low sea state. At more severe sea, Hs = 9m, the linear coherency holds in the frequency range of 0.2-0.7 rad/s, while the quadratic coherency is about 0.8 in the low-frequency range of 0-0.2 rad/s and about 0.3 in the range of 0.8~1.4 rad/s. This means that the system is more than the 2nd-order in the high sea state than in the low sea state, and that the nonlinear effects can be more extracted at the high sea due to the strong nonlinear signal as shown in the low-frequency region, where nonlinear forces are dominant (**Fig. 4.17**).

In regard to the effects of record length, the non-Gaussian method is affected by the data length, on the other hand, the Gaussian method is insensitive. The effects of data length occuring in the non-Gaussian method may be attribured to the estimation procedure: It divides given data set into many segments and makes ensemble-averages of the results of many segments. This method would give better estimations, if the number of segments would be many or if data length would be long enough.

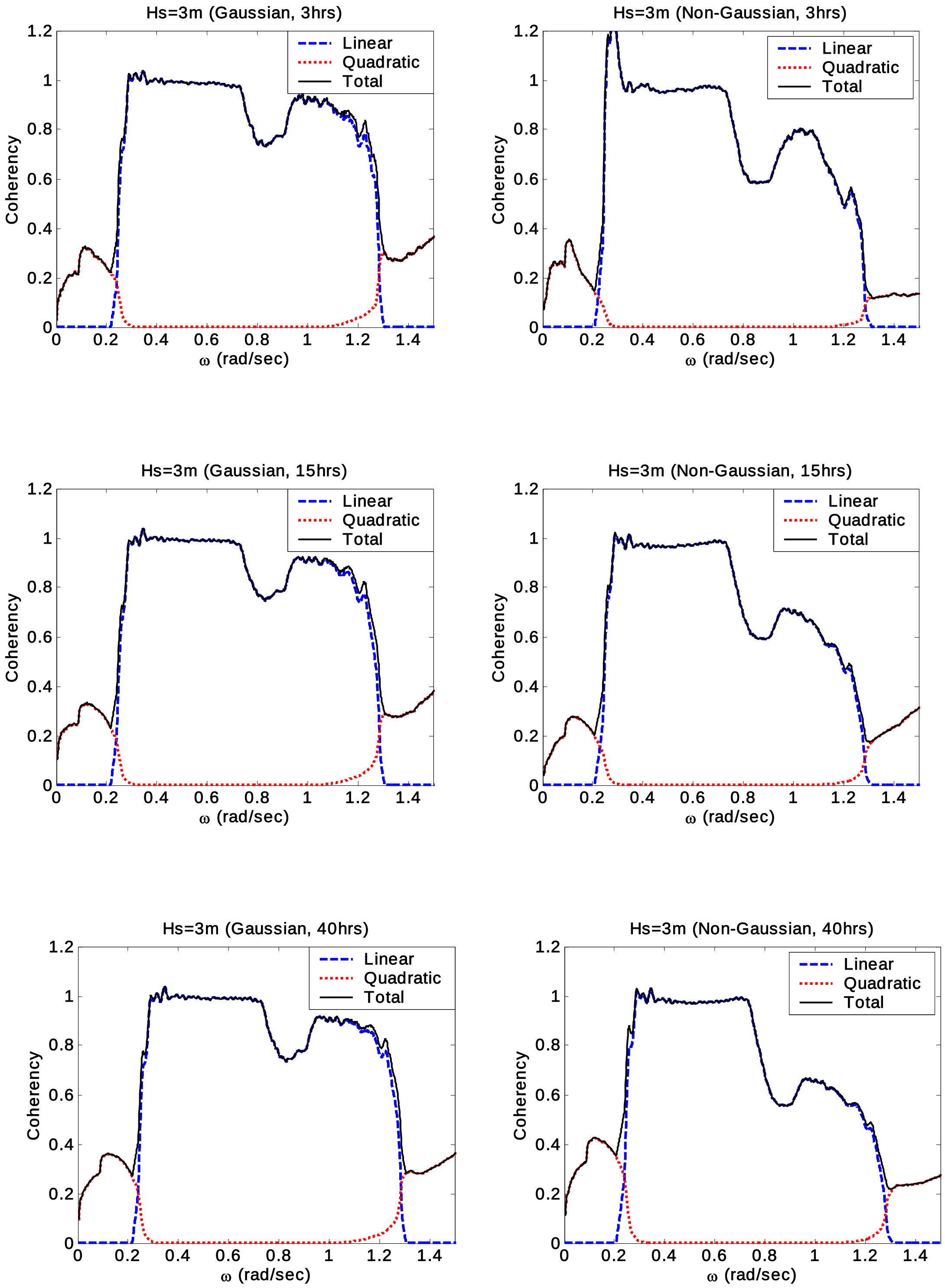

Fig. 4.18 Coherency of reconstructed surge forces of a barge at Hs=3m

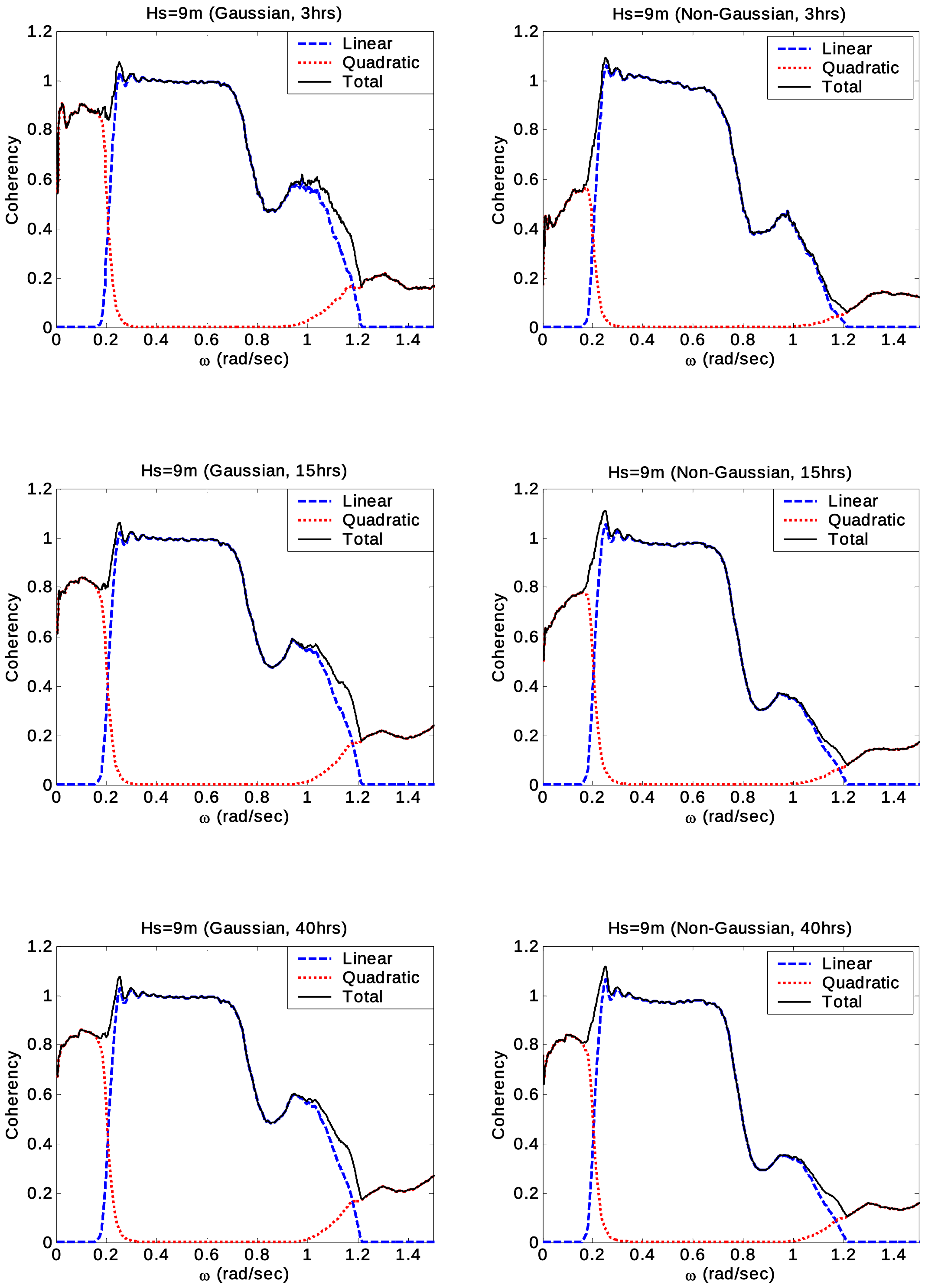

Fig. 4.19 Coherency of reconstructed surge forces of a barge at Hs=9m

4.1.12. Quadratic response spectrum

In order to consider the extracted 2nd-order responses in frequency domain, the quadratic spectra were computed by the combination of the estimated QTF and the spectrum of the waves using Eq. (3.45), which was derived under assumption of the Gaussian input, but used as approximation here.

Fig. 4.20 and **Fig. 4.21** show that the quadratic spectrum obtained from the estimated QTFs and the quadratic spectrum from the surge motion time series are in agreement. Hereby, this comparison proved the formula (Eq. 3.45) derived by Dalzell (1976). Here also, the 2nd-order effects get distinctive as the data length becomes longer and the sea state gets higher, which is the same results previous discussed with coherency.

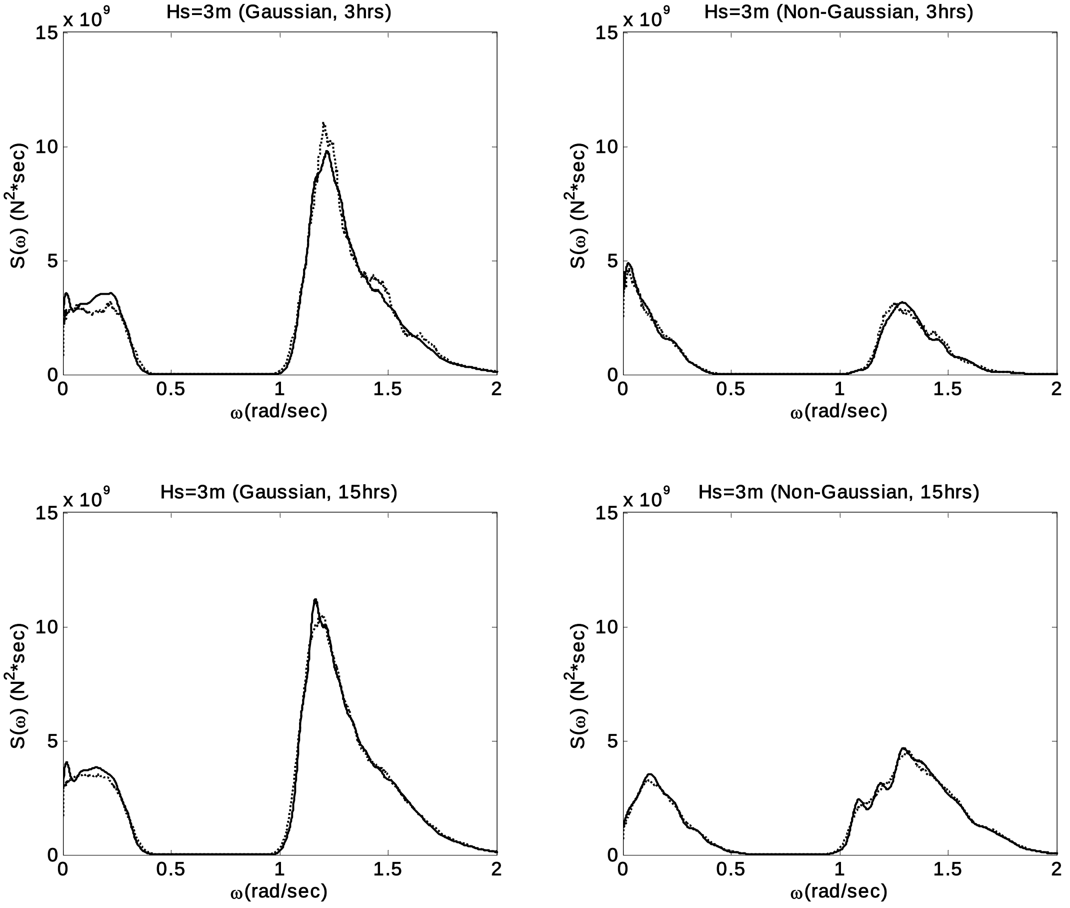
Hs=3m (Gaussian, 3hrs)
Hs=3m (Non-Gaussian, 3hrs)
Hs=3m (Gaussian, 15hrs)
Hs=3m (Non-Gaussian, 15hrs)

Fig. 4.20 Comparison between the quadratic spectrum of the extracted 2nd-order time series (dotted) and the quadratic spectrum of 2nd-order response by Eq. (3.45) (solid) at Hs=3m

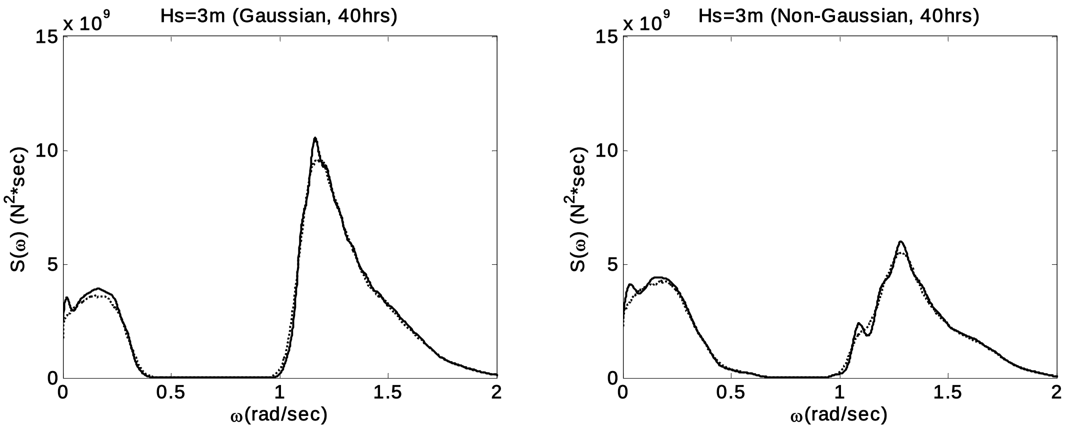

Fig. 4.20 Continued

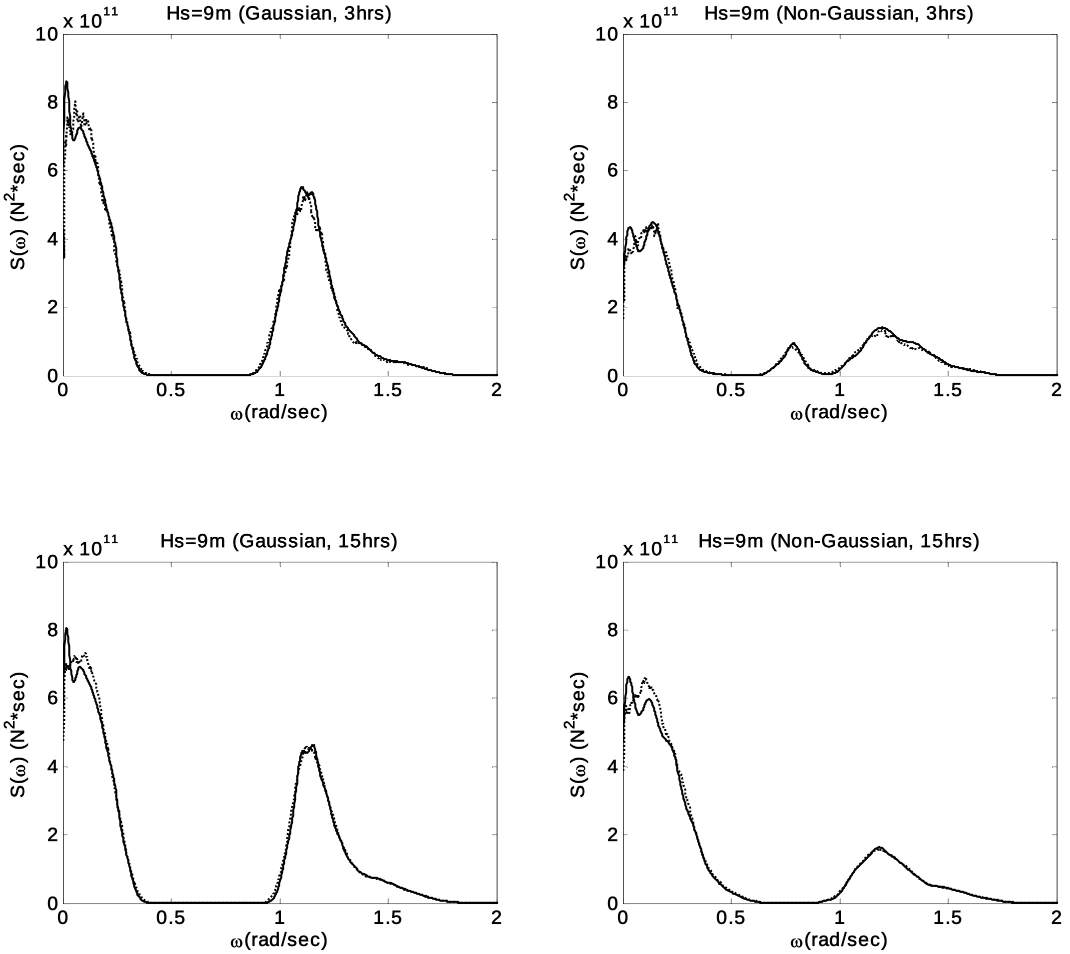

Fig. 4.21 Comparison between the quadratic spectrum of the extracted 2^{nd}-order time series (dotted) and the quadratic spectrum of 2^{nd}-order response by Eq. (3.45) (solid) at Hs=9m

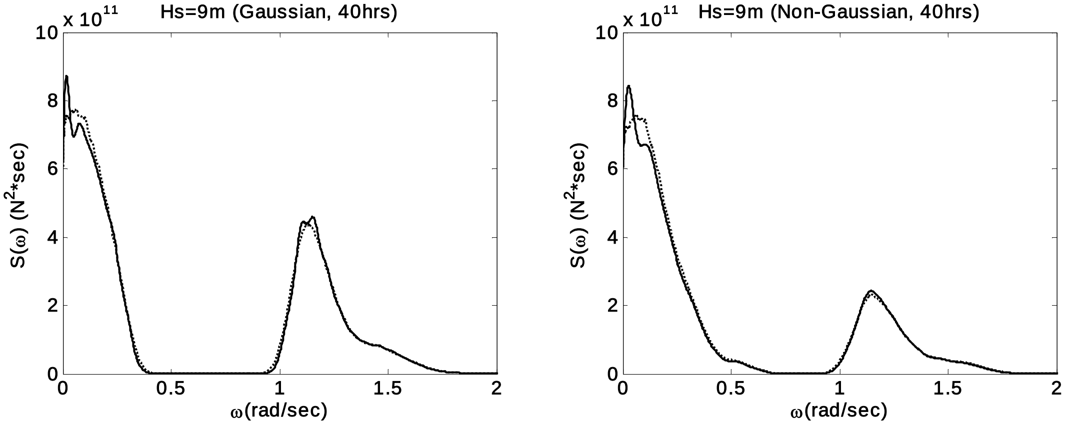

Fig. 4.21 Continued

4.1.13. Estimated mean surge force

The mean surge force was estimated from components along the estimated $G_2(\omega,-\omega)$ in the QTF plane combined with the input wave spectrum by using Eq. (3.39). The theoretical mean varies with the record length depending on the QTFs.

The estimated values by the Gaussian method are higher than by the non-Gaussian method with respect to the three given record lengths. Among these, the 40-hour data, which converged at the stead value, will be discussed (**Table 4.4**).

At the low sea of Hs=3m, errors of the Gaussian and non-Gaussian methods are 13.7% and 29.1%, respectively, while errors of the Gaussian and non-Gaussian methods are 125.5% and 108.8%, respectively at the high sea of Hs=9m. Errors in both methods at the low sea are in acceptable range, but considerably higher at higher sea.

Table 4.4 Comparison between measured and estimated mean surge force on a barge

	Hs = 3m			Hs =9m		
	Measured	G	N.G	Measured	G	N.G
3 hours	1.380×10^5	5.092×10^4	4.300×10^4	3.956×10^5	7.206×10^5	3.927×10^5
15 hours	8.086×10^4	5.441×10^4	2.515×10^4	3.517×10^5	7.184×10^5	5.860×10^5
40 hours	$\mathbf{5.676\times10^4}$	$\mathbf{4.899\times10^4}$	$\mathbf{4.022\times10^4}$	$\mathbf{3.302\times10^5}$	$\mathbf{7.446\times10^5}$	$\mathbf{6.894\times10^5}$

G: Gaussian method, N.G: Non-Gaussian method

4.1.14. Probability Exceedance Curve

Vinje (1976) theoretically approached and calculated the statistical distribution of the individual maxima. Here, the probability of exceedance for the crest height of both measured and reconstructed surge forces, by two methods for Hs=3 m and Hs=9 m, will be compared in **Fig. 4.22**.

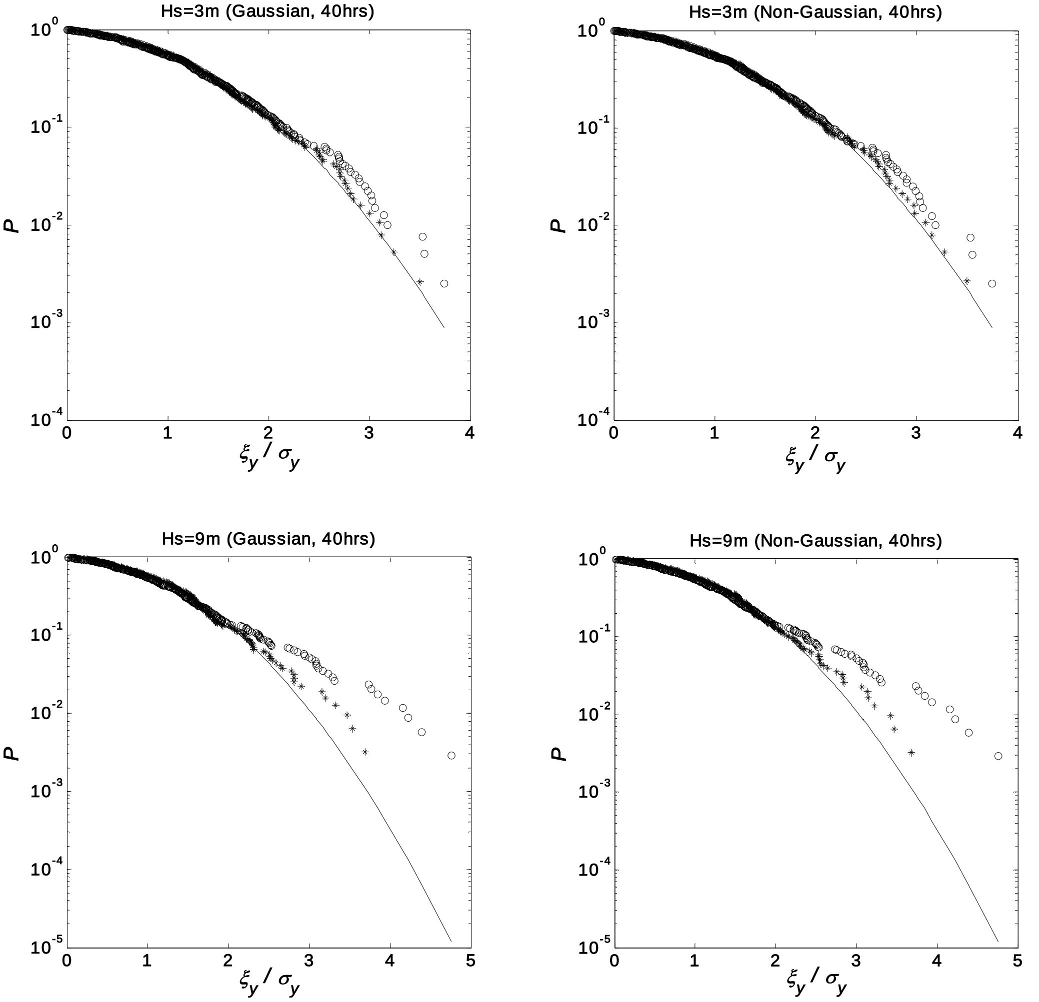

Fig. 4.22 Comparison of the probability of exceedance of the crest heights of both measured (○) and reconstructed surge forces (+)

At the low sea, Hs = 3m, the nonlinear effects are weak and the quadratic Volterra model can cover the response; thus, distributions of crest heights for measured and reconstructed surge forces are in good agreement. However, at more severe sea, Hs = 9m, the discrepancy is large due to the nonlinearity beyond the 2nd-order which the quadratic

Volterra model cannot cover. Therefore, the difference at the high sea is larger than at the low sea, which is interpreted as the nonlinear effects beyond the 2^{nd}-order. Since the reconstructed surge force was computed with the LTF and QTF by employing the quadratic Volterra model, the nonlinearity beyond the 2^{nd}-order is not reconstructed.

4.1.15. Fixed barge conclusion

Two sea states were investigated to find the effects of sea severity (Hs=3m and 9m) and record length (3 hours, 15 hours, and 40 hours) on the estimation of LTF and QTF of a fixed barge by employing the Gaussian and non-Gaussian methods. The surge force time series were reconstructed with the estimated LTF and QTF, and the 2nd-order nonlinear surge forces were extracted. The findings are as follows:

1. Both LTF and QTF estimated by the two methods varied with sea severity.
2. The 2^{nd}-order effects grew with the sea severity.
3. Coherency functions of reconstructed time series by the Gaussian and non-Gaussian methods behaved similarly in the low-frequency region as data length increased.
4. On the estimation of the mean surge force, the Gaussian method appeared to agree better with the measured mean value at low sea state, while the non-Gaussian method appeared to agree better with the measured mean value at high sea state.
5. The estimated LTF and QTF by the non-Gaussian method were more affected by the sea severity and data length than those by the Gaussian method.

4.2. Compliant mini TLP

The Gaussian and non-Gaussian methods will be applied to sea states of Hs=3.9m, which is classified as a rough sea, and the difference of both methods will be compared

4.2.1. Experimental setup

Mini TLP concept was designed for deployment off the coast of West Africa with a relatively benign environment. This platform is referred to as a “mini-TLP” because its maximum dimension in the horizontal plane is less than the outside diameter of a veridical hull column of the Heidrun TLP. Model tests of the Mini TLP were conducted in the OTRC wave basin to qualify its wave loads, airgaps, motion responses, and tensions in its tendons and risers (Liagre, 2000).

The experiments used a 1:40 scale model of a Mini TLP. The experiments were divided into two parts: fixed model tests and compliant model tests. This analysis takes into account the surge motion and uses the compliant tests data. In this compliant model test, the Mini TLP was treated in a conventional way, although the riser system was reduced to 4 risers instead of 12 in the original mini TLP design. A spring was inserted in each riser and tendon model to match the axial stiffness of the prototype risers and tendons. In the tests, both ends of risers and tendons were hinged to the floor bottom or the TLP. **Table 4.5** shows the as-built mini TLP properties in the prototype scale. Hereafter, the results are given in the prototype scale. 6 DOF motions were measured relative to center of gravity (CG).

The coordinates for the motion analysis of the mini TLP are shown in **Fig. 4.23** with *z*-axis positive upward. Wave heading is defined as the angle between the wave propagation direction and *x* axis. Analysis and reconstruction are conducted for 0 degree heading wave conditions. The target wave spectrum was chosen to simulate a 100-year West Africa stormy sea. It is a JONSWAP type spectrum of a peakness factor of 2.0, peak period of 16 seconds, and significant wave height of 3.9m. The waves were measured at a wave probe beside of the Mini TLP in **Fig. 4.23**.

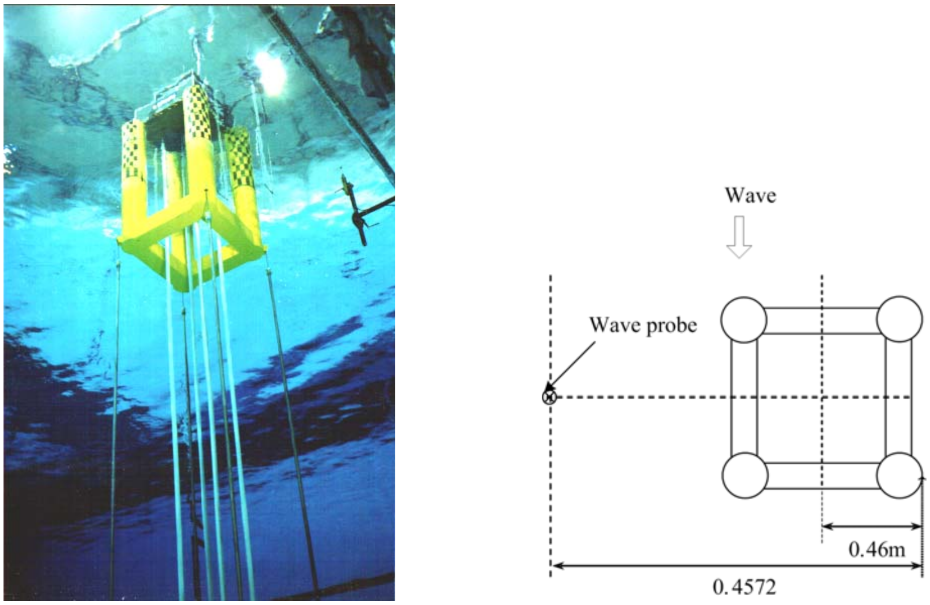

(a) (b)

Fig. 4.23 (a) Compliant model with 4 tendons and 4 risers. (Picture courtesy of P. Liagre, Texas A&M University, Texas and P. Teigen, Statoil AS, Norway), (b) the location of wave probe for measurement.

Table 4.5 Mini TLP properties

	Target		As-built			
PROPERTIES	Full scale value	Units	Full Scale value	Units	Error (%)	COMMENTS
Water depth	1000	m	673.61	m	-32.6%	Basin depth=55.25 ft.
In-place draft	28.5	m	28.51	m	0.0%	
Column diameter	8.75	m	8.64	m	-1.3%	
Pontoon height	6.25	m	6.22	m	-0.5%	
Pontoon width	6.25	m	6.22	m	-0.5%	
Column center-to-center	28.5	m	28.51	m	0.0%	
Total weight of mini-TLP	6620	mt	6445	mt	-2.6%	Total weight was decreased because vessel displacement is slightly less than target
Vessel displacement	10320	mt	10158	mt	-1.6%	
Tendon & riser pretension	3700	mt	3713	mt	0.4%	
Center of Gravity (X)	0	m	0	m	0.0%	Center of gravity slightly changed when adjusting tension in tendons and risers
Center of Gravity (Y)	0	m	0	m	0.0%	
Center of Gravity (Z)	29.5	m	29.5	m	0.0%	
Pitch radius of gyration	21.5	m	21.7	m	0.9%	Radii of gyration slightly changed when adjusting tension in tendons and risers
Roll radius of gyration	21.5	m	21.9	m	1.9%	
Yaw radius of gyration	14	m	17.2	m	22.9%	
Surge natural period	-	s	139.97	s	-	Evaluated from linear least square fitting of free decay tests
Sway natural period	-	s	135.55	s	-	
Heave natural period	2.6	s	2.79	s	7.3%	
Pitch natural period	4.9	s	4.58	s	-6.5%	
Roll natural period	4.9	s	4.56	s	-6.9%	
Yaw natural period	-	s	101.04	s	-	
Surge damping coefficient	-	-	0.1927	-	-	
Sway damping coefficient	-	-	0.1031	-	-	
Heave damping coefficient	-	-	0.0077	-	-	
Pitch natural coefficient	-	-	0.0166	-	-	
Roll natural coefficient	-	-	0.0165	-	-	
Yaw natural coefficient	-	-	0.0805	-	-	

Note: mt = metric ton.

4.2.2. Time series of wave and surge motion of a compliant mini TLP

The wave and surge motion time series are shown in **Fig. 4.24**. The sea state is classified as a rough sea (Hs=2.5-4.0) and seems to be linear random waves. The surge motion appears to be almost linear; the low-frequency surge motion looks very weak in the given time series; and the mean surge motion is also very small.

The statistics of the waves and surge motion are listed in **Table 4.6**. The mean of waves is positive unlike waves used in the previous case so that they are considered to have less nonlinearity.

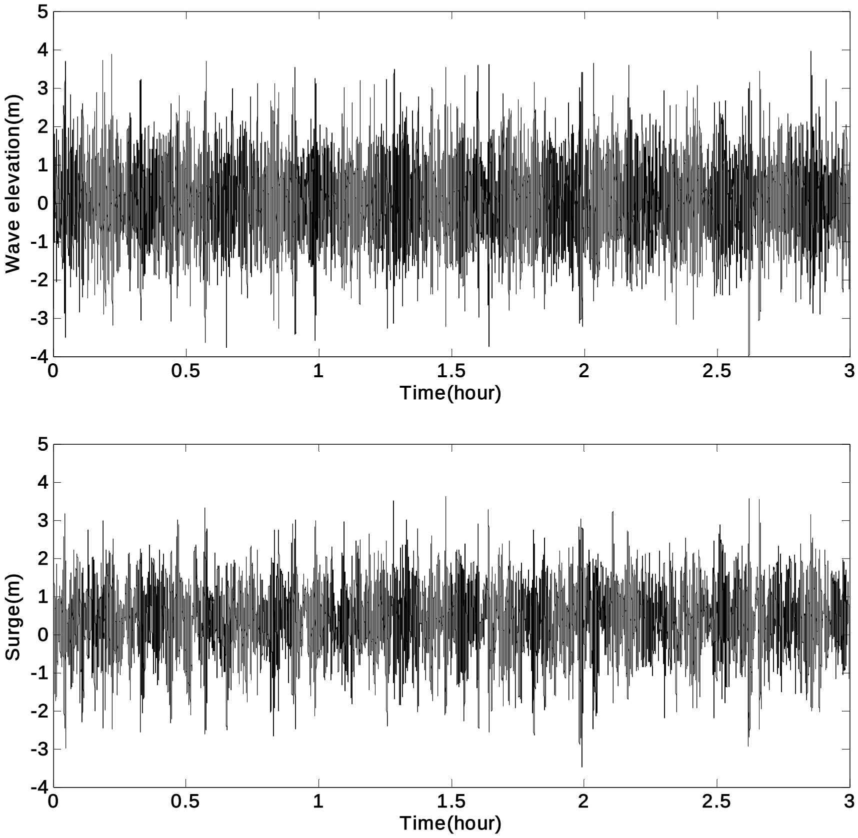

Fig. 4.24 Time series of waves (top) and surge motion (bottom)

Table 4.6 Statistics of waves and surge motion

	No. of oscillations	Mean(m)	Skewness	Kurtosis
Wave	968	0.0195	0.0522	3.1405
Surge	689	0.3698	-0.1627	3.1184

4.2.3. Statistics of measured waves

The probability densities of wave elevation and surge motion agree with the Gaussian distribution compared with the mathematical Gaussian distribution (Appendix) in **Fig. 4.25**.

Fig. 4.26 shows that the distribution of crest heights of waves and surge motion is not in agreement with the Rayleigh probability density, which implies the given data are Gaussian distribution but are not narrow band. **Fig. 4.27** illustrates the Rayleigh distribution compared with the probability of exceedence of crest heights of waves and surge motion (Appendix). The crest heights of waves and surge motion appear to be slightly deviated from Gaussian waves and are considered to be Gaussian.

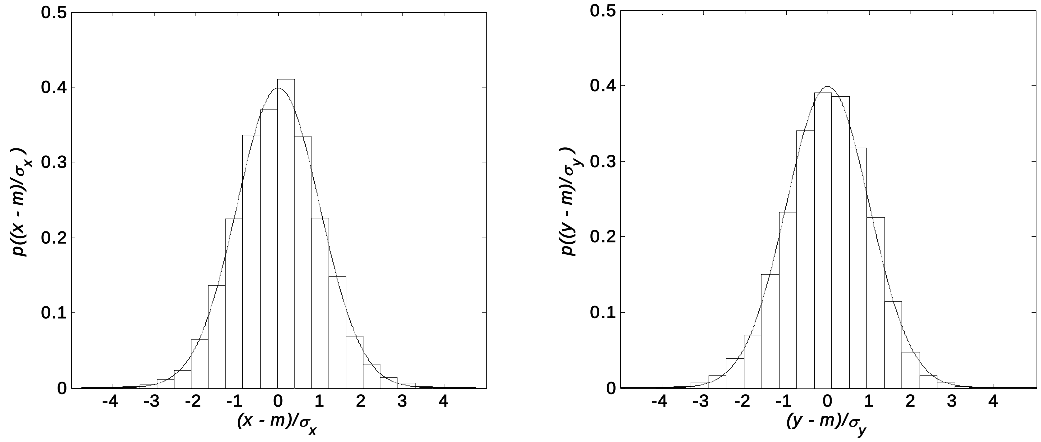

Fig. 4.25 Probability density of wave elevation (left) and surge motion (right) with Gaussian distribution (solid line)

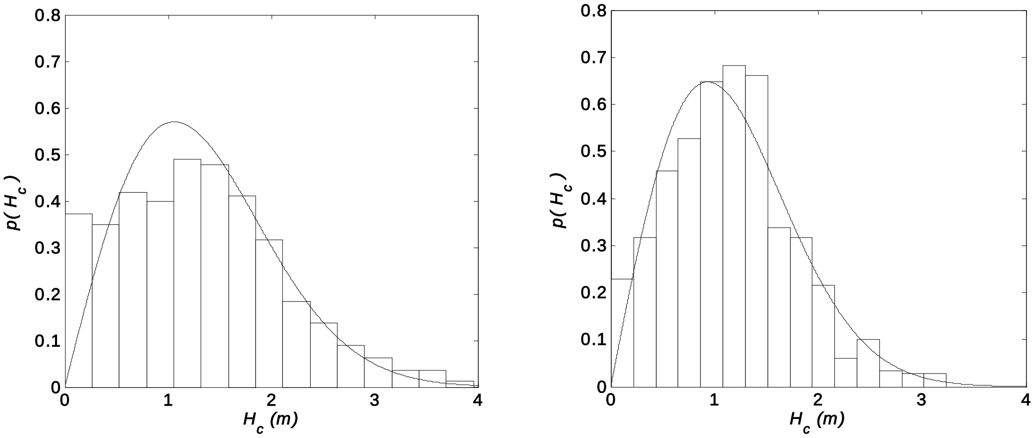

Fig. 4.26 Distribution of crest height of waves (left) and surge motion (right) compared with Rayleigh distribution (solid line)

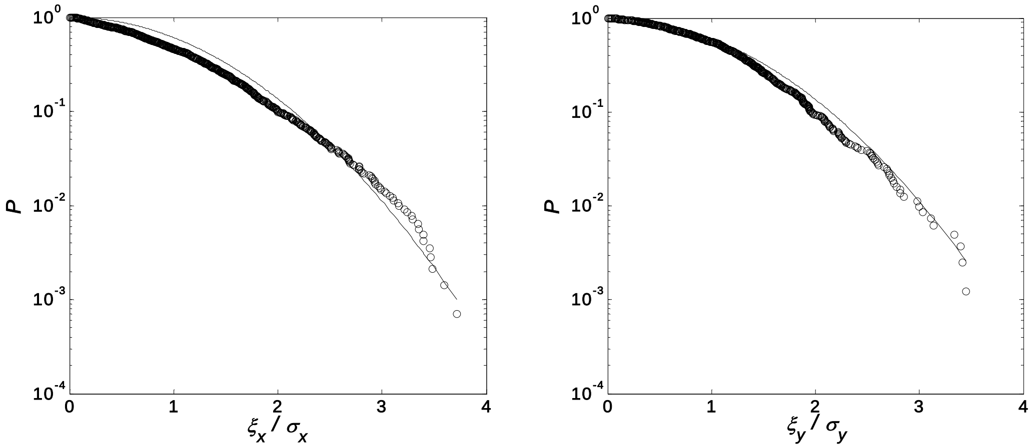

Fig. 4.27 Rayleigh distribution compared with the probability of exceedence of positive peak of wave (left) and surge motion (right)

4.2.4. Convergence of mean surge motion

The convergence of the mean surge motion was examined by the mean value averaged with moving scheme or cumulative average defined in Eq.(4.1).

Fig. 4.28 shows that the mean surge motion in a simulated 3-hour wave data has not reached a steady value. It requires more time to arrive at the unchanging mean value. The given data length for this experiment is much shorter than the data length proposed by Kim and Boo (1990).

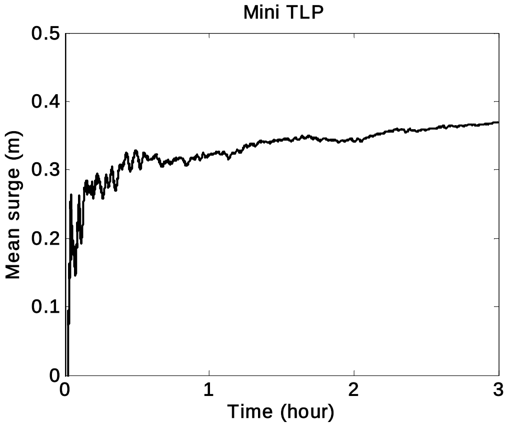

Fig. 4.28 Cumulative mean of surge motion

4.2.5. Measured wave and surge motion spectrum

The spectra of wave and surge motion are shown in **Fig. 4.29**. The target and measured spectra agree. Two peaks exist in the surge motion spectrum. The peak in the low frequency region represents the 2nd-order low-frequency surge motion created through the difference frequency interaction.

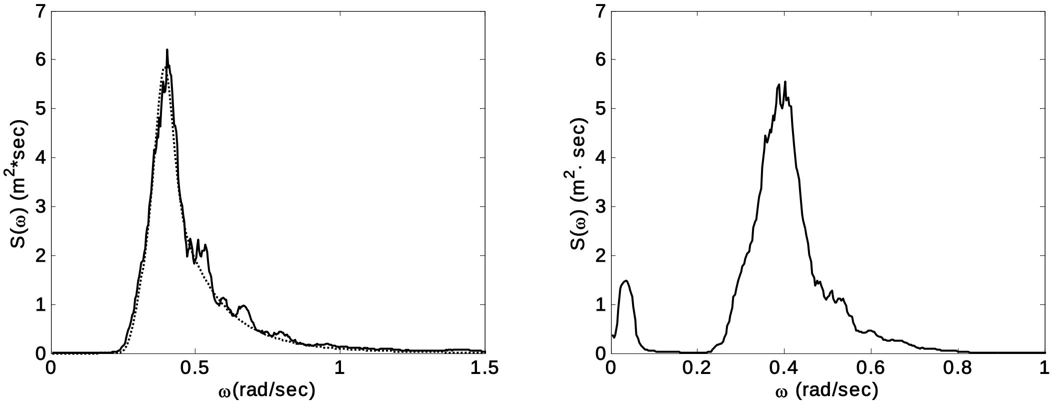

(a) (b)

Fig. 4.29 (a) Measured wave spectrum (solid), target spectrum (dotted): JONSWAP, Hs = 4m, T_p = 16 seconds, γ= 2, (b) measured surge motion spectrum.

4.2.6. Linear transform function and Quadratic transfer function

The slow drift motion of the compliant mini TLP is barely visible and is not dominant in the overall surge motion time series; and the surge motion of the compliant mini TLP is mainly a contribution of the linear surge force in the wave frequency region.

In order to take a close look at the slow drift motion clearly, the surge motion time series was filtered by a low-frequency band filter which has a pass band between 0.03 and 0.05 rad/s in **Fig. 4.30**. The mean period of the low-frequency surge motion is 165.9 seconds (0.038 rad/s) which is shown as a small peak in the surge spectrum in **Fig. 4.29**.

The surge motion spectrum in **Fig. 4.29** shows that the resonant surge motion occurs in the low frequency region, where the wave energy is negligibly small. This resonant frequency is close to the surge natural period (**Table 4.7**) and may be thought of as the resonant frequency occurring in the experiment.

As the spectrum of surge motion shows, the surge slow drift motion components are quite weak, which implies that the wave forces are not only small but also the size of the structure is smaller than other conventional compliant TLPs. Therefore, the applied forces on the mini TLP are weak, and the effects of 2nd-order difference frequency are small.

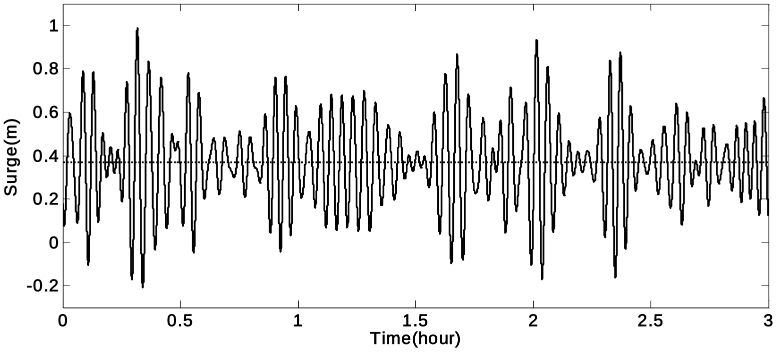

Fig. 4.30 Low frequency surge motion (No. of surge oscillation=64, average of surge period =165.9 sec)

Table 4.7 Surge natural frequency

	Target value	Measured value
Surge natural period(sec)	139.97	165.90

Fig. 4.31 shows the LTFs estimated by both methods. The LTF by the non-Gaussian method gives a less smooth curve than by the Gaussian method, which is attributed to a short data length. A smooth LTF curve would be obtained with longer data. Both estimated LTFs appear to be the same tendency, but the estimated LTF by the Gaussian method is slightly bigger in the effective wave frequency region than by the non-Gaussian.

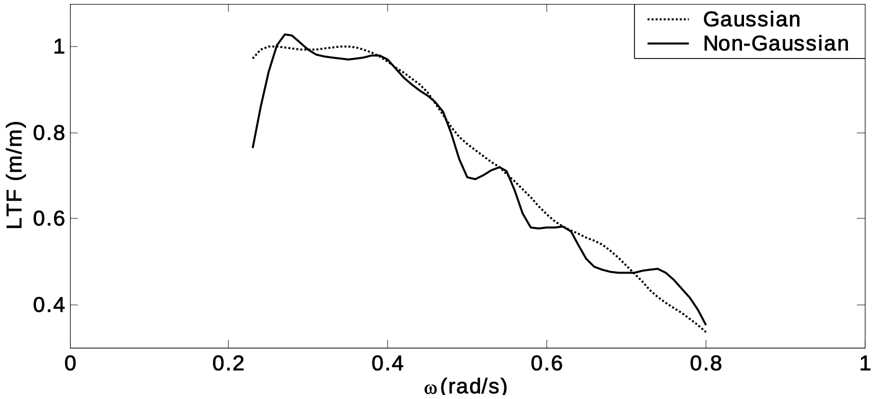

Fig. 4.31 Estimated LTF by the Gaussian and non-Gaussian methods

In the Gaussian method, each 1-hour data was computed, and an ensemble average was made over 3 hours of data to obtain the QTF. In this computation, the 70 of maximum lag was used.

In the non-Gaussian method, both input and output data were decimated by a factor R = 4. After the down sampling, the time step becomes 0.632 seconds. The maximum frequency, $\omega_{\max}$ = 9.9 rad/s, is large enough to cover the 2^{nd}-order frequency range associated with input frequency components. The segment length was chosen to be 256 and the number of segments was 66. The non-Gaussian method was modified with the principal component analysis (PCA) algorithm as used in the previous case.

Fig. 4.32 shows QTFs estimated by two methods. The QTF by the non-Gaussian method is smaller in volume than by the Gaussian method like the previous case with 3-hour data. Given a long enough data, a QTF would increase in volume.

The 2^{nd}-order components of a compliant mini TLP in a surge motion are mainly created by the low frequency 2^{nd} -order motion; thus, there is one distinctive bump along Ω_1-axis, and there is no bump along Ω_2 -axis in both QTFs.

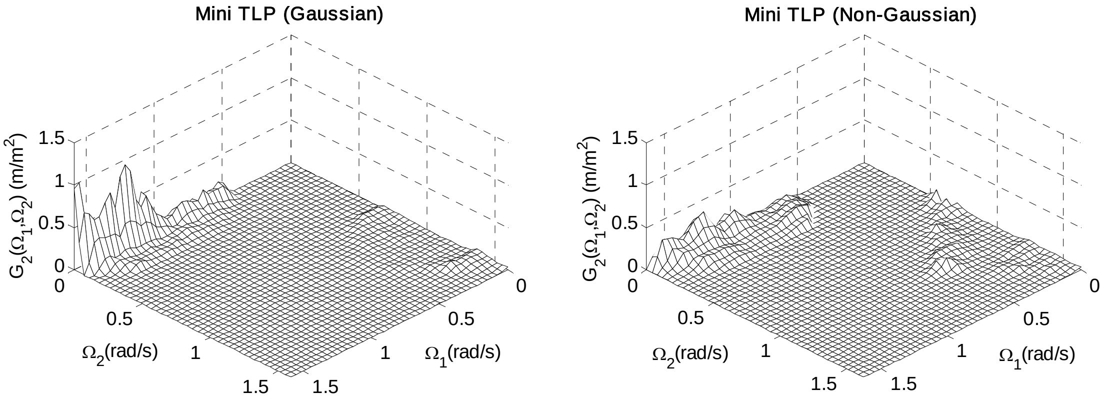
Mini TLP (Gaussian)

Mini TLP (Non-Gaussian)

Fig. 4.32 Estimated QTF by the Gaussian and non-Gaussian methods

4.2.7. Reconstruction

Time series were reconstructed with the estimated LTF, QTF, and input wave spectrum by employing Eq. (3.18). **Fig. 4.33** (a) illustrates comparisons between the measured and reconstructed time series by the Gaussian and non-Gaussian methods. The difference of both methods is not clearly seen in the time series. In the comparison of the extracted 2^{nd}-order surge motion, however, the 2^{nd}-order surge motion of the Gaussian method is stronger that that of the non-Gaussian, which is due to the difference of volume in QTFs.

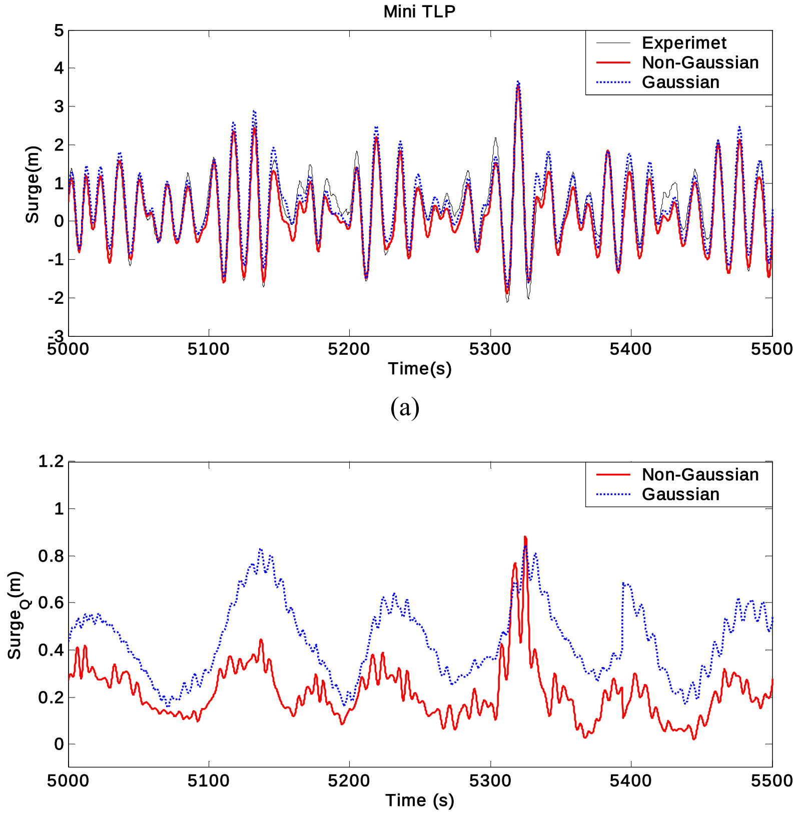

(a)

(b)

Fig. 4.33 Reconstruction of surge motion: (a) Linear + Quadratic (b) Quadratic

Fig. 4.34 shows the reconstructed low-frequency surge motion which is filtered by a band filter. The amplitudes of the 2nd-order low-frequency surge motion by the Gaussian method are stronger than by the non-Gaussian method. This result is attributed to the bigger volume in the QTFs.

Zero-upcrossing analysis was applied to the 2nd-order low-frequency surge motion to compare the low-frequency surge periods of the reconstructed time series with the low-frequency surge periods of the measured time series. It was found that the periods of both reconstructed low-frequency surge are almost same as the measured value listed in **Table 4.8**.

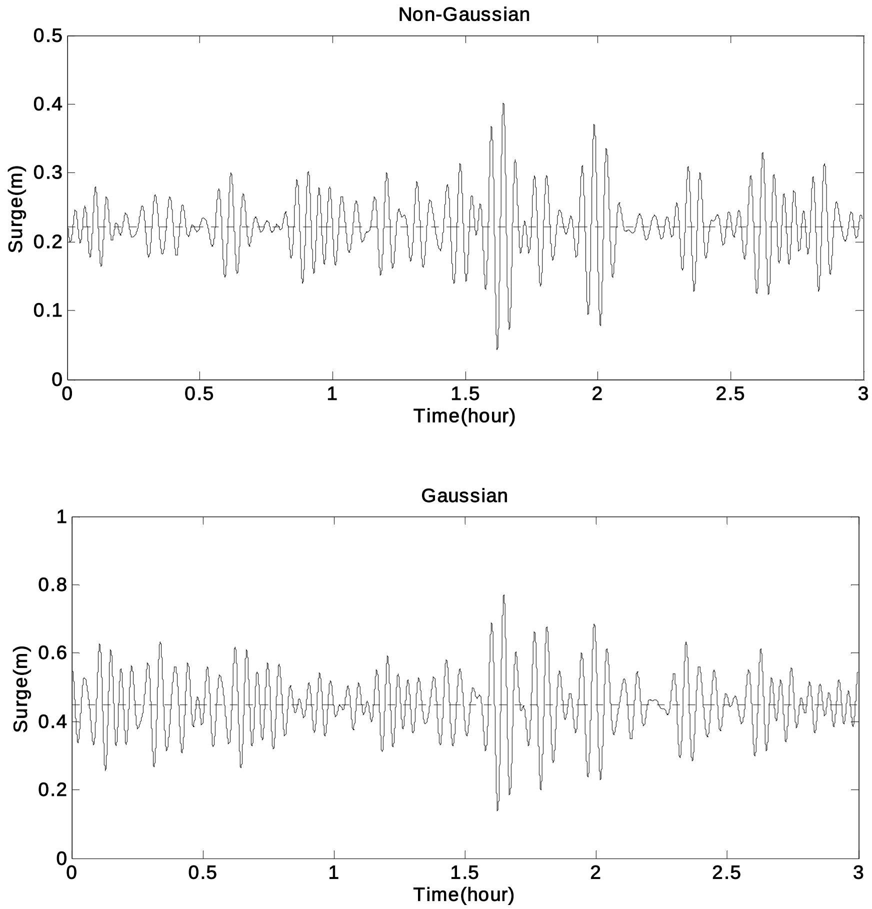

Fig. 4.34 Reconstructed low frequency surge motion

Table 4.8 Reconstructed low frequency surge motion (0.03rad/s<ω< 0.05rad/s)

	Gaussian method	Non-Gaussian method	measured
average of surge period (s)	162.8	163.3	165.9

4.2.8. Normalized mean square error

To compare the reconstructed and measured time series qualitatively, the normalized mean square error (NMSE) was computed as a statistical comparison with Eq.(4.2). The NMSE by the non-Gaussian method is slightly lower in the mini TLP (**Table 4.9**).

Table 4.9 Normalize mean square error

	Mini TLP	
	Gaussian method	Non-Gaussian method
3 hours	0.430	0.370

4.2.9. Surge motion spectrum

The surge motion spectra of reconstructed time series was compared with that of measured time series in **Fig. 4.35**. They are in agreement in the frequency region higher than 0.1 rad/s except less than 0.1 rad/s. The spectrum of the non-Gaussian method shows a bigger difference than that of the Gaussian method in the low-frequency region corresponding to a bump along Ω_1-axis in the G_2 plane of a QTF in **Fig. 4.32**, which is induced by a smaller bump of the estimated QTF by the non-Gaussian method.

The difference in both methods that occurred in the low-frequency region of spectra may be interpreted as a resonance by the natural surge period of the mini TLP.

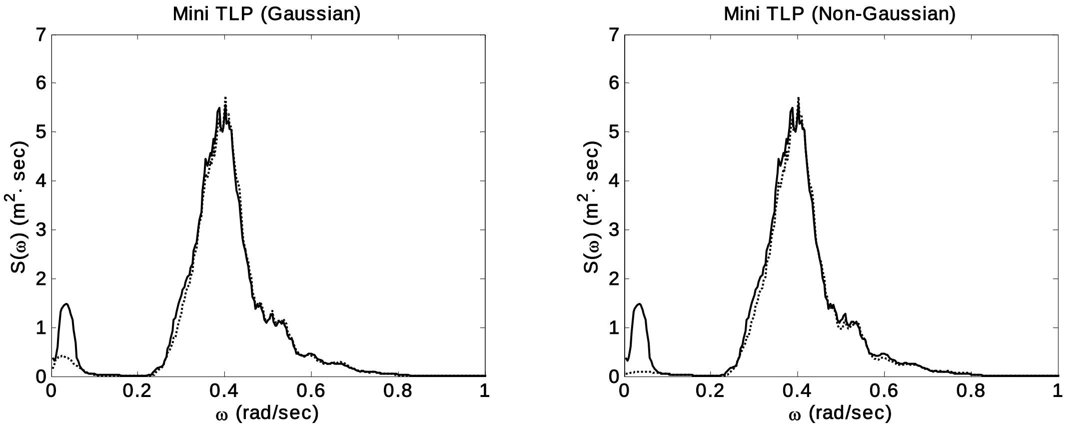

Fig. 4.35 Spectrum of surge motion: measured (solid), reconstructed (dotted)

4.2.10. Comparisons of coherency

The reconstructed data and measured data are used for the coherency test. The linear and quadratic coherency function (Eqs. (4.3) and (4.4)) were calculated in **Fig. 4.36**.

The linear coherency is close to 1 over the quite large frequency region, 0.2~0.9 rad/s, which means that the linear surge motion is dominant and the quadratic surge motion is small in this region. The quadratic coherency is about 0.4 for the Gaussian method and 0.2 for the non-Gaussian method, while the non-Gaussian method is much higher than the Gaussian method beyond 1 rad/s.

The coherency in the low-frequency region is considerably small because of the weak slowly varying surge motion unlike other compliant TLPs.

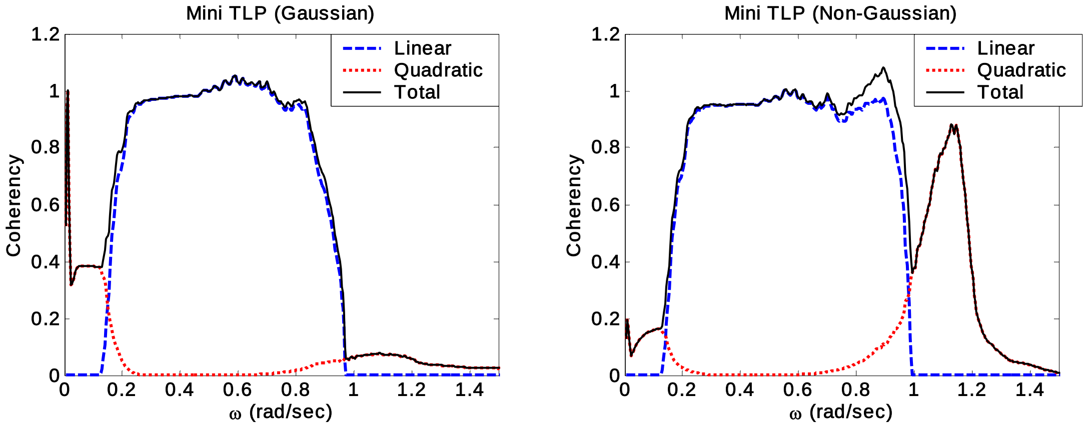

Fig. 4.36 Coherency of reconstructed surge motion

4.2.11. Quadratic response spectrum

In order to consider the 2nd-order components in the frequency domain, output spectra were computed directly from QTFs and the input wave spectrum by Eq. (3.45).

Fig. 4.37 shows that the quadratic spectrum obtained from the estimated QTFs and the quadratic spectrum from the surge motion time series are in agreement. The estimated 2nd-order surge motion spectrum by the Gaussian method is larger than by the non-Gaussian method which has a smaller bump in the QTF. The 2nd-order effects are detected in the low-frequency region, which are negligibly small in the high-frequency region, as expected in the surge motion of floating structures.

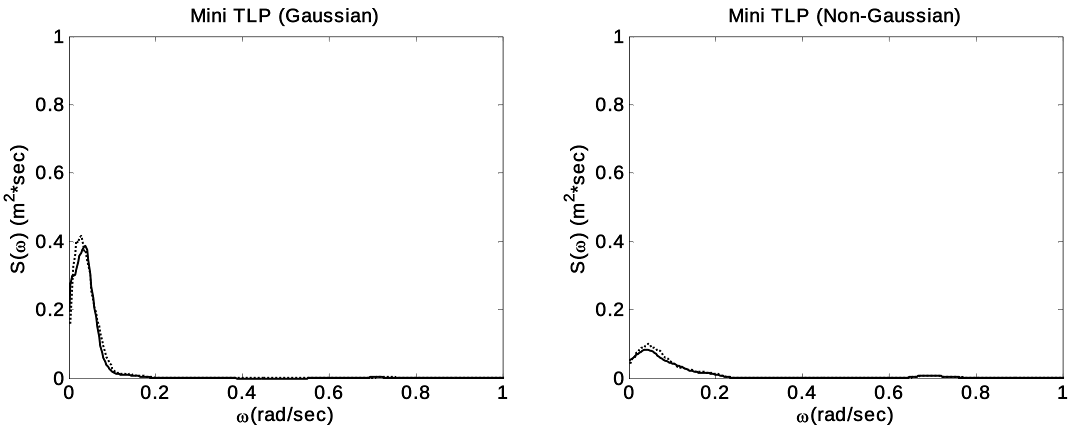

Fig. 4.37 Comparison between the quadratic spectrum of the extracted 2nd-order time series (dotted) and the quadratic spectrum of 2nd-order response by Eq. (3.45) (solid)

4.2.12. Estimated mean surge motion

The mean surge motion was estimated from components along the estimated $G_2(\omega,-\omega)$ in the QTF plane combined with a combination of the input wave spectrum by using Eq.(3.39).

The mean value by the Gaussian method was overestimated with the error of 21.4%; on the other hand, it was underestimated with the error of 47.8% by the non-Gaussian method (**Table 4.10**). The Gaussian method is favorable at a low sea state for prediction of mean surge as seen in a barge case.

Table 4.10 Estimated mean surge

Measured	Gaussian method	Non-Gaussian method
0.3698m	0.449m	0.193m

4.2.13. Probability exceedance curve

The low-frequency motion makes a zero-mean surge motion fluctuating about zero in the time series so that the overall positive peaks get lower in the time series; thus, the probability of exceedance gets lower.

Reversely, the reconstructed surge motion lost low-frequency effects (**Fig. 4.35**). Then the overall positive peaks went up compared with the measured surge motion; hence, the probability of the exceedance curve of the reconstructed surge motion is higher than that of the measured surge motion in **Fig. 4.38** unlike the previous case.

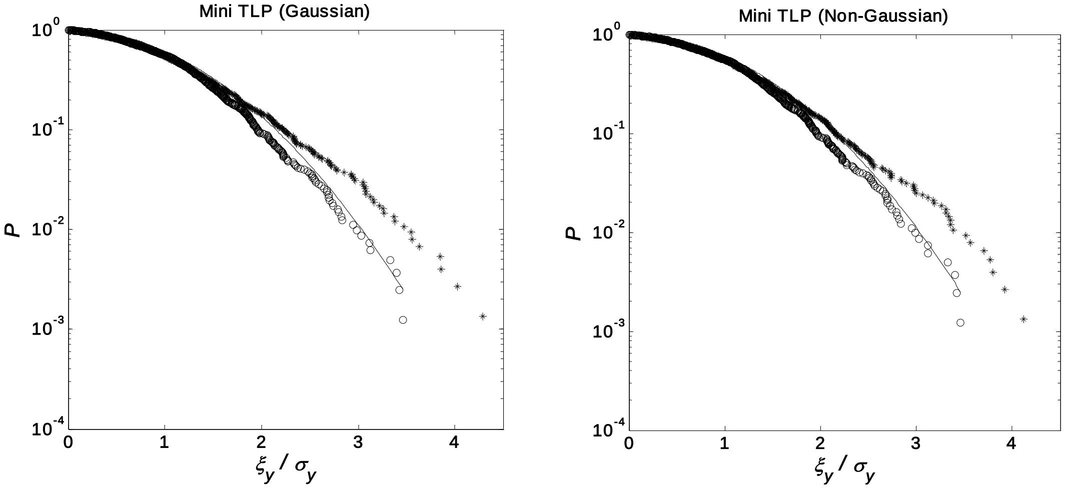

Fig. 4.38 Rayleigh distribution compared with the probability of exceedance of positive peak; measured (○), reconstructed (+)

4.2.14. Compliant mini TLP Conclusion

The LTF and QTF of a complaint mini TLP were estimated by the Gaussian and non-Gaussian methods with 3 hour data at a sea state of Hs=3.9m. The surge motion time series were reconstructed with the estimated LTF and QTF, and the 2nd-order nonlinear surge motion was extracted. The findings are as follows:

1. The low-frequency surge motion was so small that it was hard to extract 2nd-order low-frequency components from measured time series.
2. The coherency functions of reconstructed time series were considerably low in the low-frequency region.
3. The linear coherency held in the broad frequency range of 0.2~0.9 rad/s, and the linear surge motion was dominant in the given data.
5. The estimated mean surge motion by the Gaussian method appeared to be better than the non-Gaussian method at each given sea state.

4.3. A fixed and truncated column

In this case, the Gaussian and non-Gaussian methods will be applied to sea state of Hs=15.4m, which is classified as a phenomenal sea, and the difference of both methods will be compared (Stansberg et al. 1995).

4.3.1. Experimental setup

The surge forces on a vertical truncated cylinder in irregular waves were measured in the wave basin of the MARINTEK. The diameter of the cylinder is 0.626m in model scale of 1:55 (**Fig. 4.39**). The model corresponds to 100 year storm sea where sea state is Hs=15.4m, T_p=17.8sec, and JONSWAP, γ=1.7 in full scale. Wave was run to simulate a 3-hour 100-year storm in scale 1:55. Within this 3-hour duration, several large and steep wave events occurred.

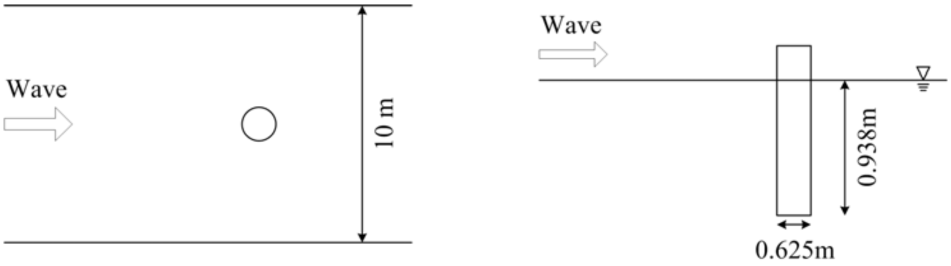

Fig. 4.39 Top view (left) and side view (right)

4.3.2. Time series of wave and surge force on a truncated column

The simultaneously measured wave and surge force time series are shown in **Fig. 4.40**. This time series show the typical aspect that crests of waves lead those of horizontal forces. Comparing the peaks of the waves and forces at the same time instant, wave peaks are leaded by surge force peaks in average about 90 degrees, as seen in general cases.

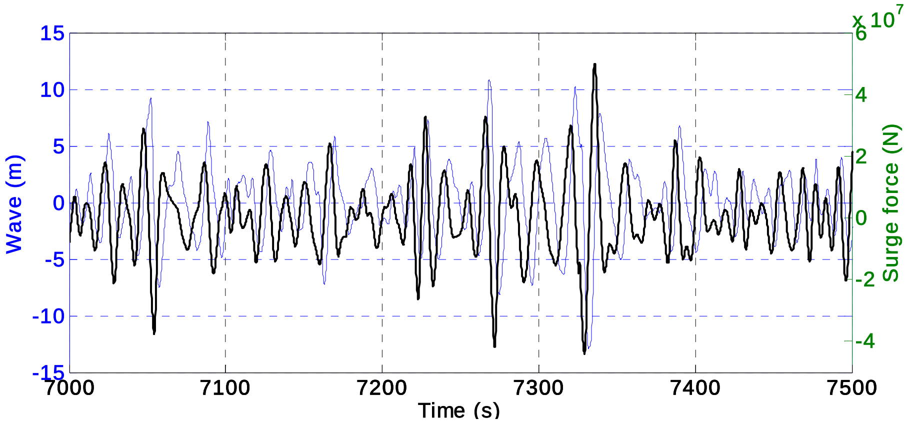

Fig. 4.40 Time series of wave (thin), surge force (thick)

Skewness of the surge forces is smaller than we expected, even though highly non-linear waves are applied (**Table 4.11**). Waves do not seem to be strongly asymmetrical, even though the significant wave height is high. In this case, the mean of wave data is negative because of the contribution of the depression due to the 2^{nd}-nonlinear effect, as seen in a previous case.

Table 4.11 Statistics of wave and surge force

	Mean(m)	Skew ness	Kurtosis
Wave	-0.035	0.157	3.072
Surge force	4.5×10^5	0.003	3.055

4.3.3. Statistics of measured waves and surge force

Fig. 4.41 shows the probability density of waves and surges force compared with the mathematical Gaussian distribution (Appendix). The distributions of crest heights of waves and surge forces are compared with the Rayleigh distribution in **Fig. 4.42**. It is hard to discuss about nonlinearity with these probability density curves, and the probability of exceedence of positive peaks of waves and surge forces should be examined.

Fig. 4.43 illustrates the Rayleigh distribution compared with the probability of exceedence of positive crest heights **(**Appendix**)** of waves and surge forces**.** The degree of the deviation from the mathematical curve indicates the nonlinearity. Waves appear to be nonlinear, but surge forces do not appear to be highly nonlinear, as shown. This agrees with the statistics (**Table 4.1**) in the section.

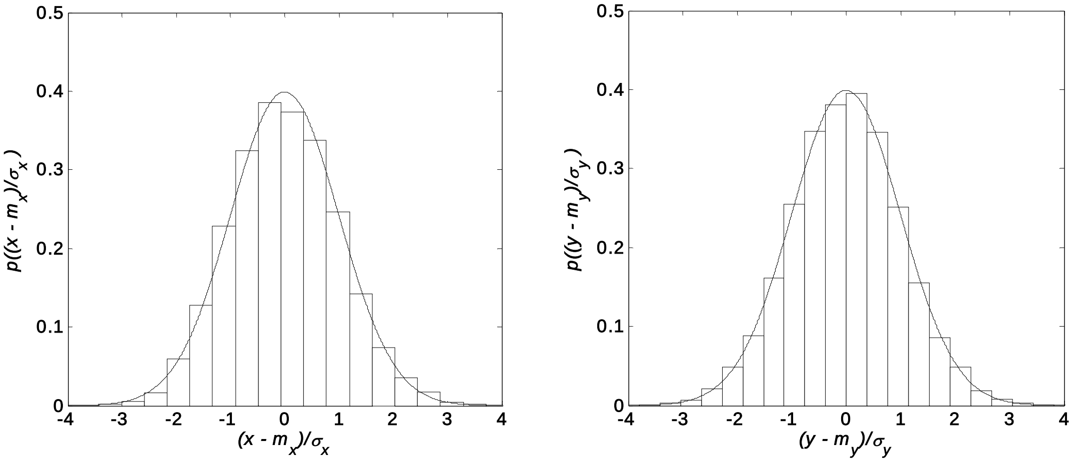

Fig. 4.41 Probability density of wave elevation (left) and surge force (right) with Gaussian distribution (solid line)

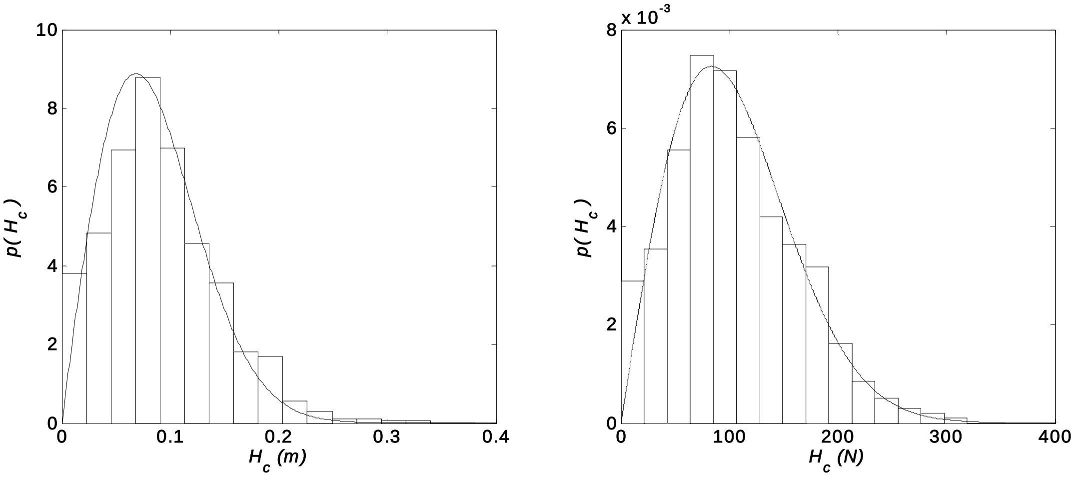

Fig. 4.42 Distribution of crest height (model scale) of waves (left) and surge force (right) compared with Rayleigh distribution (solid line)

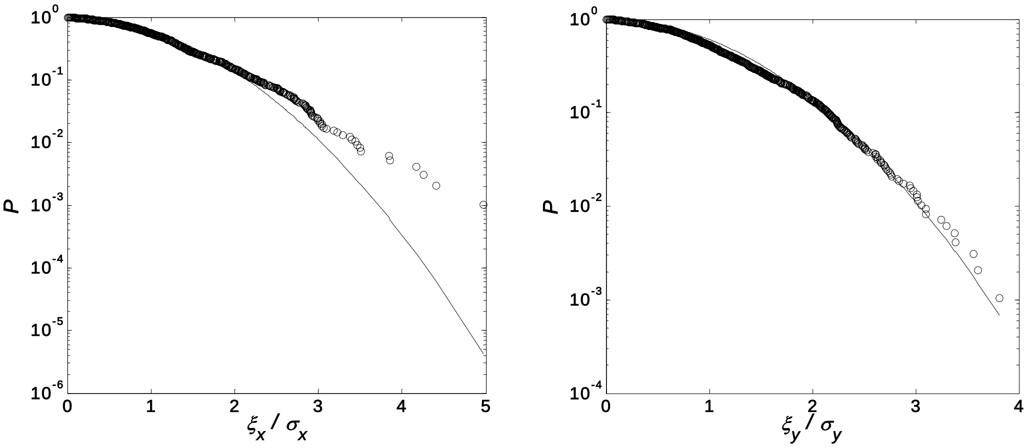

Fig. 4.43 Rayleigh distribution compared with the probability of exceedence of positive peak of wave (left) and surge forces (right)

4.3.4. Convergence of mean surge force

The convergence of the mean 2^{nd}-order forces is examined by mean value averaged with moving scheme or cumulative average defined in Eq. (4.1).

Fig. 4.44 shows that the mean surge force in a simulated 3-hour wave data has not reached a steady value. It is required more time to arrive at unchanging mean value. The given data length for this experiment is much shorter than the data length proposed by Kim and Boo (1990).

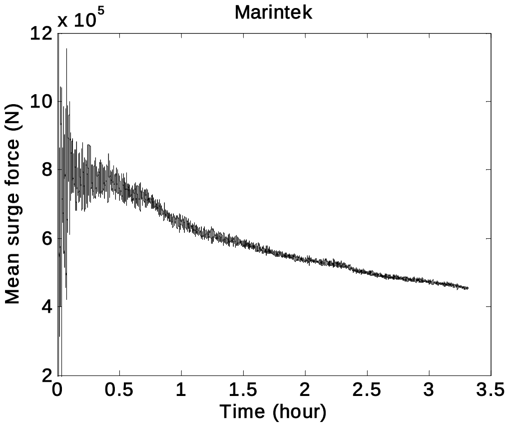

Fig. 4.44 Cumulative mean of surge force

4.3.5. Measured wave and surge force spectrum

The spectra of waves and surge forces are shown in **Fig. 4.45**. The peak of wave target spectrum is higher than that of the measured data, which implies that waves generated in a wave tank include less steep waves than the targeted waves and contain less nonlinearity.

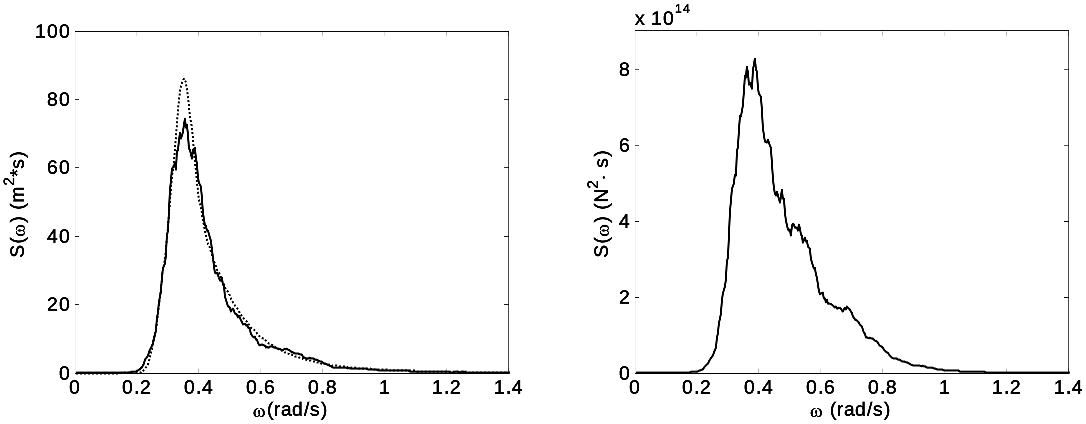

Fig. 4.45 Measured wave spectrum (solid), target spectrum (dotted): JONSWAP, Hs = 15.4m, T_p = 17.8sec, γ= 1.7(left), measured surge force spectrum (right).

4.3.6. Linear transform function and Quadratic transfer function

LTFs are shown in **Fig. 4.46** by employing both the Gaussian and non-Gaussian methods. The LTF of the non-Gaussian method seems to be less smooth than that of the Gaussian method because the given data length is not so long enough to have the smooth LTF. If long enough data is given, the LTF by the non-Gaussian method would be smoother. In the region of 0.2-0.6 rad/s which is effective wave spectrum region, both methods appear to be same tendency, but the estimated LTF by the Gaussian method is slightly bigger than by the non-Gaussian.

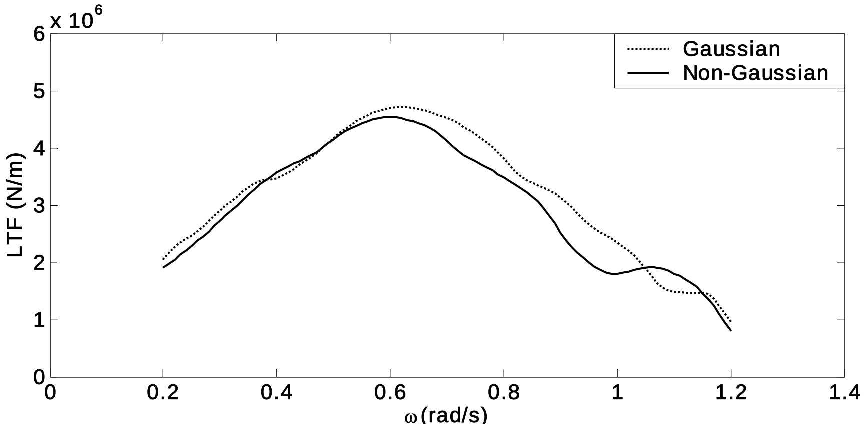

Fig. 4.46 LTF by the Gaussian assumption and non-Gaussian methods

This case deals with only 3-hour data due to the lack of long enough data. In the Gaussian method, each 1-hour data was computed, and ensemble average was made over 3 hours of data to obtain QTF. In this computation, 70 of maximum lag was used. In non-Gaussian input method, both input and output data were decimated by a factor $R = 5$. After the down sampling, the time step becomes 0.742 second. The maximum frequency, $\omega_{\max} = 8.5$ rad/s, is large enough to cover the 2nd-order frequency range associated with input frequency components. The segment length was chosen to be 128 and the number of segments was 109. The non-Gaussian method was modified with principal component analysis (PCA) algorithm as used in the previous cases.

Fig. 4.47 shows QTFs by two methods. The QTF by the non-Gaussian method is smaller in volume than by the Gaussian method like a previous case with 3-hours data. Given a long enough data, a QTF would increase in volume. Two bumps exist along Ω_1 and Ω_2-axis in both QTFs. This implies that there are not only the low-frequency forces, but also the high-frequency forces due to the 2nd order effects.

The waves used here as an input fall in the category of phenomenal sea. However, the volume of the QTF is not so big compared with that of a barge. It may be thought that the nonlinear forces are not so strong, even though the sea state is high. This result is also agrees with the statistics of waves and surge forces.

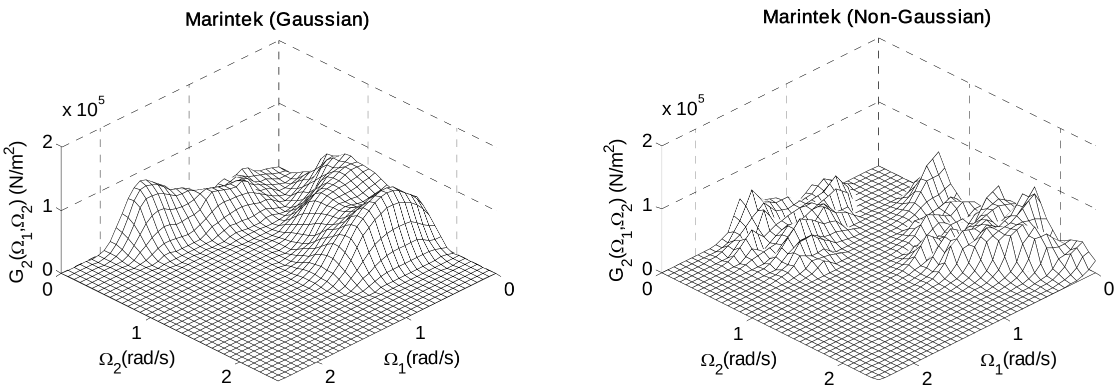

Fig. 4.47 Estimated QTFs by the Gaussian and non-Gaussian methods.

4.3.7. Reconstruction

As a method of evaluation of the quality of the LTF and QTF estimated by the Gaussian and non-Gaussian methods, the reconstruction was employed as previous cases. **Fig. 4.48** illustrates a comparison of the measured and reconstructed time series of output by the Gaussian and non-Gaussian methods. The difference in the reconstructed and measured total time series are small, which is interpreted as the lack of nonlinearity in surge forces even though Hs=15.4m. But the extracted quadratic surge forces shows that Gaussian method gives stronger amplitude than the non-Gaussian method.

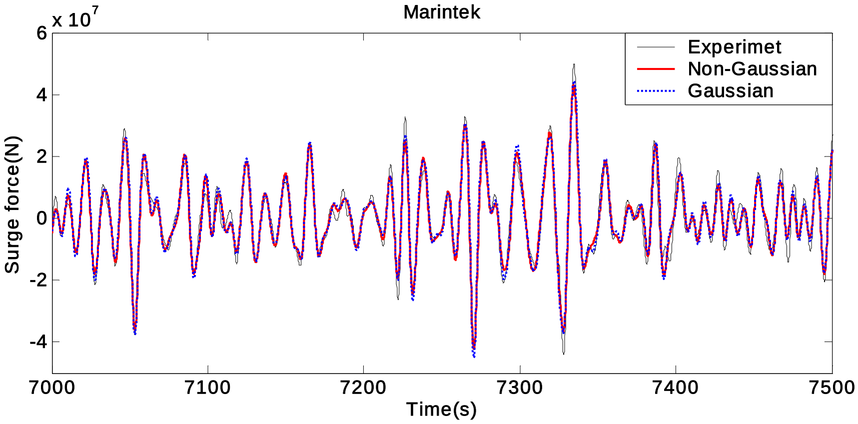

(a)

Fig. 4.48 Reconstruction of surge forces (a) Linear + Quadratic (b) Quadratic

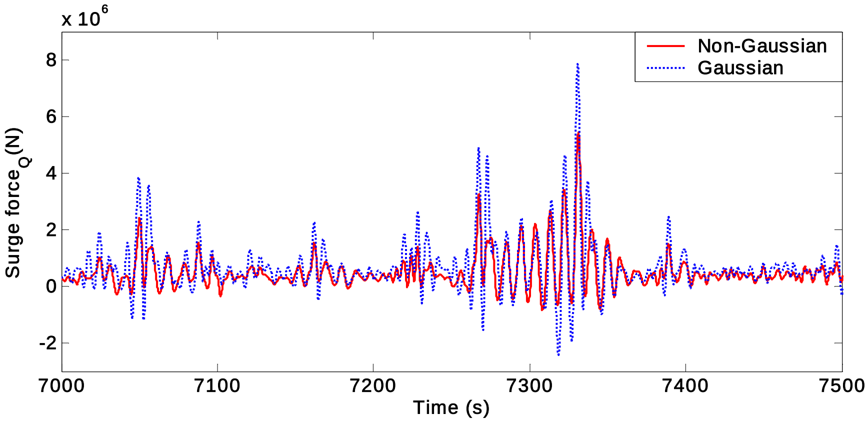

(b)

Fig. 4.48 Continued

4.3.8. Normalized mean square error

To compare the reconstructed and measured time series qualitatively, the normalized mean square error was computed as a statistical comparison Eq. (4.2). The difference of NMSE is negligibly small (**Table 4.12**). Errors are approximate 29% for both methods.

Table 4.12 Normalize mean square error

	Marintek	
	Gaussian method	Non-Gaussian method
3 hour	0.291	0.286

4.3.9. Surge force spectrum and coherency function

The power spectra of the reconstructed surge forces are shown in **Fig. 4.49**. The spectrum by the Gaussian method is slightly larger in 0.2-04 rad/s than the measured spectrum, which is a different result than previous cases.

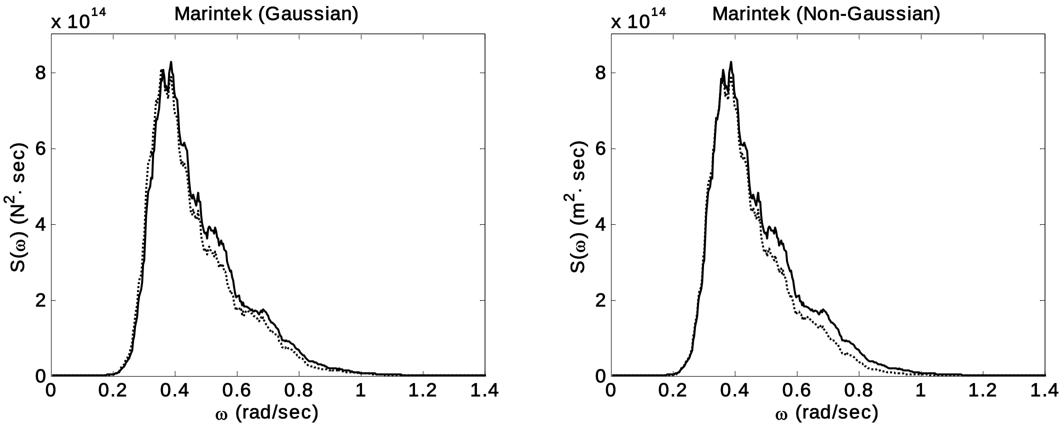

Fig. 4.49 Spectrum of surge forces: measured (solid), reconstructed (dotted)

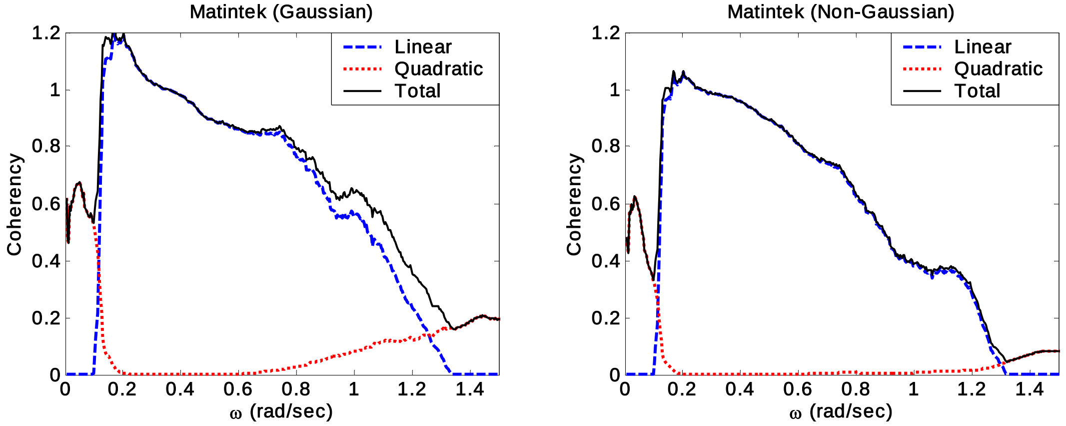

Fig. 4.50 Coherency of reconstructed surge forces

The reconstructed data and measured data were used for the coherency test. The linear and quadratic coherency functions (eq. (4.3) and (4.4)) are shown in **Fig. 4.50**.

In the Gaussian method, the linear coherency is much higher than 1 for some frequencies and the quadratic coherency is slightly higher than that of the non-Gaussian method in the entire frequency region.

It is known that the total coherence function should lie in 0 and 1. But the coherency by the Gaussian method exceeded 1 in the region of 0.2-0.4 rad/s. Even though the non-Gaussian method is in an acceptable range, but the total coherency is considerably low in the entire region. This results may be attributed to the nonlinearity beyond the 2nd-order in the waves. The waves used as an input are highly nonlinear and go over the 2nd-order theory (Kumar and Kim, 2002) as motioned in the Chapter II.

Therefore, the given sea state is considered too high for the Volterra quadratic model, irregardless of the Gaussian and non-Gaussian methods. Moreover, waves are highly nonlinear and surge forces are linear; the input is non-Gaussian, while the output is Gaussian; hence, this system could not be considered an ordinary system, and the Volterra Quadratic model would not be an appropriate model to analyze this system.

4.3.10. Quadratic response spectrum

In order to consider the extracted 2nd-order responses in frequency domain, the quadratic spectra were computed by combination of the estimated QTF and the spectrum of the waves using Eq. (3.45), which was derived under assumption of the Gaussian input but used as approximation here.

Fig. 4.51 shows that the quadratic spectrum obtained from the estimated QTFs and the quadratic spectrum from the surge motion time series are in agreement. The quadratic spectrum by the Gaussian method is lager than by the non-Gaussian method like the previous cases.

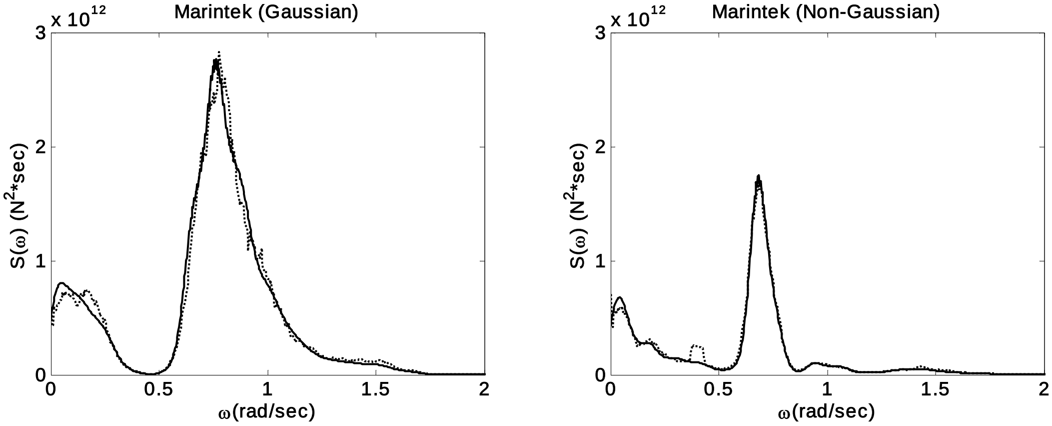

Fig. 4.51 Comparison between the quadratic spectrum of the extracted 2nd-order time series (dotted) and the quadratic spectrum of 2nd-order response by Eq. (3.45) (solid)

4.3.11. Estimated mean surge motion

The mean surge force was estimated from components along the estimated $G_2(\omega,-\omega)$ in the QTF plane combined with a combination of the input wave spectrum by using Eq. (3.39).

The mean value was overestimated with the error of 66.1% and 24.4% by the Gaussian and non-Gaussian method (**Table 4.13**), respectively. In the previous two cases, which are covered by the 2nd-order theory, the error of the Gaussian method is smaller than that of the non-Gaussian. But the non-Gaussian method gave better results at the highly nonlinear sea state beyond the 2nd-order.

Table 4.13 Estimated mean surge forces

Measured	Gaussian method	Non-Gaussian method
4.326×10^5 N	7.185×10^5 N	5.381×10^5 N

4.3.12. Probability exceedance curve

The reconstructed responses lost the energy as shown in spectra (**Fig. 4.49**) so that the amplitudes of reconstructed responses are lower than those of the measured responses; thus, positive peaks of reconstruction are lower than measured peaks.

Fig. 4.52 shows that the difference of probability of exceedance of positive peak between the measured and reconstructed time series and that the non-Gaussian method is better than the Gaussian method.

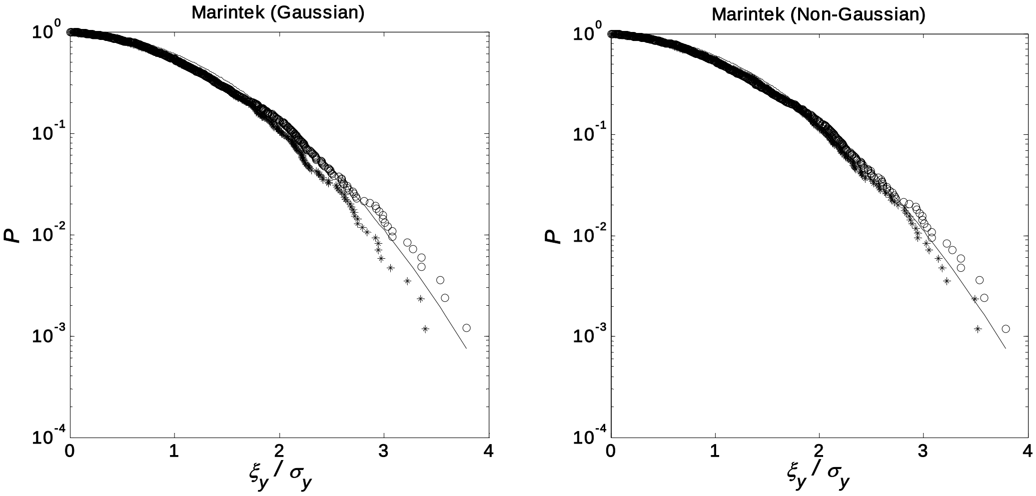

Fig. 4.52 Rayleigh distribution compared with the probability of exceedance of positive peak; measured (○), reconstructed (+)

4.3.13. Fixed and truncated column conclusion

The LTF and QTF of a fixed and truncated column were estimated by the Gaussian and non-Gaussian methods with 3 hour data at a sea state of Hs=15.4m. The surge force time series were reconstructed with the estimated LTF and QTF, and the 2nd-order nonlinear surge forces were extracted. The findings are as follows:

1. Waves used as an input followed the non-Gaussian process, while surge forces closely followed the Gaussian process
2. The linear coherency function held in the narrow frequency region of 0.2~0.5 rad/s, whereas neither the linear nor quadratic coherency functions held in other frequency regions, and the coherency function of the non-Gaussian method seemed better than that of the Gaussian method.
3. The mean surge force estimated by the non-Gaussian method appeared to agree better with the measured mean value than did the Gaussian method estimates at this phenomenal sea state.

CHAPTER V

SUMMARY AND CONCLUSION

The LTFs and QTFs have been estimated, and the quality of them for the input (wave) and output (forces and motion) of ocean structures has been investigated in this dissertation. The estimation has been carried out by employing the Volterra quadratic model with two different methods: the Gaussian and non-Gaussian methods. In addition, the estimations include the effects of sea severity and data length. For the Gaussian method, the algorithm developed by Dalzell was used, and for the non-Gaussian method, the algorithm by Kim and Powers was used in combination with the principal component analysis (PCA). Estimations in this dissertation included all of the frequencies of the QTFs distributed in the entire bi-frequency domain. Past research has been limited to the low-frequency region.

Comparisons between these two methods have been made in both time and frequency domains. In the time domain, the reconstructed time series were compared with measured time series to evaluate the quality of estimated LTFs and QTFs, but the difference between these two methods was not clearly seen in time series. In the frequency domain, the difference was much more distinctive in the comparison of their spectra, coherencies, and estimated mean values. Therefore, the time domain comparisons were relatively insensitive to whether one uses the Gaussian or non-Gaussian methods. On the other hand, the frequency domain comparisons were sensitive to these methods.

For the effects of sea severity on the estimation of the response function, it was found that the LTFs were affected by sea state. It was also confirmed that the QTF is very sensitive and varies with sea state. In regard to the estimated mean values that are crucial for structure designing, the Gaussian method at low sea state and the non-Gaussian method at high sea state were favorable. Therefore, the applicable and proper sea states for two methods exist for the estimation of LTFs and QTFs. Specifically; coherency tests have shown good coherencies over the wider frequency region at low sea state, and considerably low coherencies at high sea states. It was found that it is hard to extract the 2^{nd}-order components from data with significantly weak nonlinear signals.

For the effects of data length on the estimation of the response function, only a barge case was investigated due to lack of available data. Most wave basins produce approximately 3 hour long data; for this study, however, 40-hour data sets for a barge were produced to examine the effects of the data length. It was found that QTFs were affected by the record length, but the effects of data length in LTFs were negligibly small. Among other things, the non-Gaussian method for estimation of QTFs is more affected by the data length than the Gaussian method. This is attributed to the ensemble average technique which involves the number of segments in the given data length. Consequently, this dissertation proposes that data sets long enough to estimate reasonable QTFs should be required.

Finally, this dissertation recommends that the Gaussian method at low sea states and the non-Gaussian method at high sea states should be applied, and the algorithm to remove the unrealistically large QTF occurring in the division process of the Gaussian method and the matrix inversion of the non-Gaussian method may need to be continued as a future research.

REFERENCES

Barrett, N (1963). "The Use of Functionals in the Analysis of Non-linear Physical Systems," *J of Electronics and Control*, Vol. 15, No. 6, pp. 567-615.

Bendat, JS (1990). "Nonlinear System Analysis and Identification from Random Data," John Wiley & Son, New York.

Birkelund, Y., Hanssen, A. and Powers, EJ (2003). "On the Estimation of Nonlinear Volterra Models in Offshore Engineering," *Int J Offshore and Polar Engineering*, Vol 13, No 1, pp 12-20.

Birkelund, Y, and Powers, EJ (2001). "Higher-Order Spectral Estimators and Nonlinear System Identification," *Proc 11th Int Offshore and Polar Eng Conf*, ISOPE, Stavanger, Norway, Vol 3, pp 78-84.

Dalzell, JF (1972). "Application of Cross-Bi-Spectral Analysis to Ship Resistance in Waves," SIT-DL-72-1606, Stevens Institute of Technology, Hoboken, NJ, May.

Dalzell, JF (1974). "Cross-Bispectral Analysis: Application to Ship Resistance in Waves," *J Ship Res*, Vol 18, No 1, pp 62-72.

Dalzell, JF (1976). "Application of the Functional Polynomial Model to the Ship Added Resistance Problem," *11th Symposium on Naval Hydrodynamics*, London.

Dalzell, JF and Kim, CH (1979). "An Analysis of Quadratic Frequency Response for Added Resistance, "*J Ship Res*, Vol 23, No 23, pp 198-208.

Dean, RG and Sharma, JN (1981). "Simulation of Wave Systems Due to Nonlinear Directional Spectra," *Int Symposium Hydrodynamics in Ocean Eng*, The Norwegian Inst of Tech, pp 1211-1222.

Hasselman, K (1966). "On Non-Linear ship Motions in Irregular Waves," *J of Ship Research*, Vol 10, No. 1. pp 64-68.

Hineno, M (1984). "The Calculation of the Statistical Distribution of the Maxima of Nonlinear Response in Irregular Waves," *Proc of annual conference of the society of naval architects of Japan*, pp 216-225.

Kim, CH (2005). "Nonlinear Waves and Offshore Structures," World Scientific Publishing Co, Singapore.

Kim, CH and Boo, SY (1990). "Statistical Analysis of Slow Drift Forces in Random Seas," *Proc 1st Pacific /Asia Offshore Mechanics Symposium*, Seoul, Korea, pp 169-177.

Kim, KI, and Powers, EJ (1988). "A Digital Method of Modeling Quadratically Nonlinear Systems with a General Random Input," *IEEE Trans Acoustics, Speech, and Signal Processing*, Vol 36, pp 1758-1769.

Kim, NS, and Kim, CH (2002). "Cross-Bi-Spectral Estimation of Nonlinear Force on Fixed Structure in Nonlinear Waves," *Proc 12th Int Offshore and Polar Eng Conf*, ISOPE, Kitakyshu, Japan, Vol 3, pp 188-195.

Kim, NS, and Kim, CH (2003). "The Effect of Sea Severity on the Cross-Bi-Spectral Estimate of Quadratic Response Function for Surge Exciting Forces," *Proc 13th Int Offshore and Polar Eng Conf*, ISOPE, Honolulu, HI, Vol 3, pp 413-420.

Kim, NS, and Kim, CH (2004). "Gaussian- and Non-Gaussian-Input Method for Extraction of QTFs from Test Data of Offshore Structures," *Proc 14th Int Offshore and Polar Eng Conf*, ISOPE, Toulon, France, Vol 3, pp 416-423.

Kim, SB, and Powers, EJ (1995). "Estimation of Volterra Kernels via higher-order statistical signal processing," in: Boashash, B, Powers, EJ, and Zoubir, AM, eds, *Higher-Order Statistical Signal Processing*, Wiley, New York, pp 213-239.

Kim, SB, Powers, EJ, Miksad, RW, and Fisher FJ (1992). "Identification of Quadratic Drift Response of TLP's Using Conditioned Orthogonal QFRF's," *Proc 2nd Int Offshore and Polar Eng Conf*, ISOPE, San Francisco, USA, Vol 3, pp 540-544.

Krafft, MJ and Kim, CH (1990). "Experimental Investigation of Quadratic Frequency Response Function for Slow Drift in Bi-Frequency Domain," *Proc 1st Euro Offshore Mech Symp*, ISOPE, Trondheim Paper 193, pp 37-46.

Krafft, MJ and Kim, CH (1992), "Surge Drift Motion of a Moored Vessel in Random Waves," *Int J of Offshore and Polar Engineering*, Vol 2, No 3, September, pp. 168-174.

Kumar, A, Kim, CH, and Zou, J (2002). "Limitation of the 2nd-order Theories for Laboratory High Sea Waves and Forces on Structures," *Int J of Offshore and Polar Engineering*, Vol 12, No 4, pp 243-248.

Liagre, PE (2000). *Mini-TLP 2000* report. Description of experimental setup and data for the model basin at Offshore Technology Research Center, Texas A&M Research Park, College Station, TX.

Maruo, H (1957), "The Excess Resistance of a Ship in Rough Seas", *International Shipping Progress*, Vol 4, No 35, pp 337-345.

Matsui, T, Suzuki, T, and Sakoh, Y (1992). "Second-Order Diffraction Forces on Floating Three-Dimensional Bodies in Regular Waves," *Int J of Offshore and Polar Engineering*, Vol 2, No 3, pp 175-185.

Naess A (1985). "Statistical Analysis of Second-Order Response of Marine Structures," *J of Ship Research*, Vol 29, No 4, pp 270-284.

Newman, JN (1974). "Second-Order, Slowly-Varying Forces on Vessels in Irregular Waves," International Symposium on Marine Vehicles and Structures in Waves, London, 1974, pp 193-197.

Niedzwecki, JM, Liagre, PF, Roesset JM, and Kim MH (2001). " An Experimental Research Study of a Mini-TLP," *Proc 11th Int Offshore and Polar Eng Conf*, ISOPE, Stavanger, Norway, Vol IV, pp 631-633.

Scharf, LL (1991). Statistical Signal Processing, Addison-Wesley, New York.

Schetzen, M (1981). “Nonlinear System Modeling Based on the Wiener Theory,” *Proc. IEEE*, Vol 69, pp 1557-1573.

Stansberg, CT (1992). "On the Estimation of Extreme Mooring Line Forces," *Proc the OMAE 1992 Conf*, Calgary, Canada**,** I-A, pp 291-300.

Stansberg, CT (2001). "Data Interpretation and System Identification in Hydrodynamic Model Testing," *Proc 11th Int Offshore and Polar Eng Conf*, ISOPE, Stavanger, Norway, Vol 3, pp 1-9.

Stansberg, CT, Huse, E, Krogstad, JR, and Lehn, E (1995). "Experimental Study of Non-Linear Loads on Vertical Cylinders in Steep Random Waves," *Proc 5th Int Offshore and Polar Eng Conf*, ISOPE, Hague, Netherlands, Vol 1, pp 75-82.

Tick, LJ (1961). “The Estimation of the Transfer Functions of Quadratic Systems,” *Technometrics*, Vol 3, No 4, pp 563-567.

Tupper, E (1996). *Introduction to Naval Architecture*, 3rd ed, Butterworth-Heinemann, Oxford.

Vassilopoulos, LA (1966). "The Application of Statistical theory of Non-Linear Systems to Ship Motion Performance in Random Seas", *International Shipping Progress*, Vol 14, No 150, pp 54-65.

Vinje, T (1976). “On the Calculation of Maxima of Non-linear Waveforces and Wave Induced Motions,” *International Shipbuilding Progress*, Vol. 23, No. 268, pp 393-400.

Volterra, V (1959). *Theory of Functionals and of Integral and Integro-Differential Equations*, Dover Publications Inc., New York.

APPENDIX A

BASIC STATISTICS

Mean Value, Mean Square Value, Variance, Skewness and Kurtosis

The *mean value* or expected value $E[x]$ is the time average of sample $x(t)$ over the total record length T, or the area under the sample curve divided by the time length T, which are given in the continuous and discrete forms:

$$E[x] = \frac{1}{T}\int_0^T x(t)dt = \frac{1}{N-1}\sum_{j=1}^{N} x_j = \mu_x \tag{A-1}$$

where $T = (N-1)\Delta t$, $x_j = x(j\Delta t)$.

The *mean square value* $E[x^2]$ is the time average of $x^2(t)$, in continuous and discrete forms:

$$E[x^2] = \frac{1}{T}\int_0^T x^2(t)dt = \frac{1}{N-1}\sum_{j=1}^{N} x_j^2 \tag{A-2}$$

The *variance* σ_x^2 of $x(t)$, in continuous and discrete forms:

$$\sigma_x^2 = E[(x-\mu_x)^2] = \frac{1}{T}\int_0^T \left(x-\mu_x\right)^2 dt = \frac{1}{N-1}\sum_{j=1}^{N}\left(x_j-\mu_x\right)^2 \tag{A-3}$$

or, $\sigma_x^2 = E[x^2] - \mu_x^2$.

where σ_x is called standard deviation or *rms* (root mean square) value of the process $x(t)$.

The *skewness* is defined as the time average of $(x-\mu_x)^3$ normalized by σ_x^3 or called non-dimensional third moment:

$$E[\frac{1}{\sigma_x^3}(x-\mu_x)^3] = \frac{1}{T}\int_0^T \frac{\left(x-\mu_x\right)^3}{\sigma_x^3}dt = \frac{1}{N-1}\sum_{j=1}^{N}\frac{\left(x_j-\mu_x\right)^3}{\sigma_x^3} \tag{A-4}$$

The kurtosis is the non-dimensional 4th moment, in the continuous and descrete forms:

$$E[\frac{1}{\sigma_x^4}(x-m_x)^4]=\frac{1}{T}\int_0^T\frac{\left(x-\mu_x\right)^4}{\sigma_x^4}dt=\frac{1}{N-1}\sum_{j=1}^{N}\frac{\left(x_j-\mu_x\right)^4}{\sigma_x^4} \qquad \text{(A-5)}$$

The spectral moment of one-sided spectrum

The n^{th} spectral moment of one-sided spectrum is defined as

$$m_n=\int_0^\infty \omega^n S_{xx}(\omega)d\omega \qquad \text{(A-6)}$$

,where m_0 stands for the area of the spectrum or the variance. The standard deviations of the displacement, velocity and acceleration, are respectively:

Gaussian (normal) distribution

The probability density function of a process may be represented by bell shaped Gaussian (normal) equation:

$$p(x)=\frac{1}{\sqrt{2\pi}\sigma_x}\exp[-\frac{(x-m_x)^2}{2\sigma_x^2}],\ -\infty\le(x-m_x)\le\infty \qquad \text{(A-7)}$$

The above probability density is normalized by standard deviation (**Fig.A.1**):

$$p\left(z\right)=\frac{1}{\sqrt{2\pi}}\exp\left(-\frac{z^2}{2}\right),\quad z=\frac{\left(x-m_x\right)}{\sigma_x},\ -\infty\le z\le\infty \qquad \text{(A-8)}$$

The dimensional expression depends on the standard deviation, σ_x, while the nondimensional presentation is identical to the case of unit standard deviation.

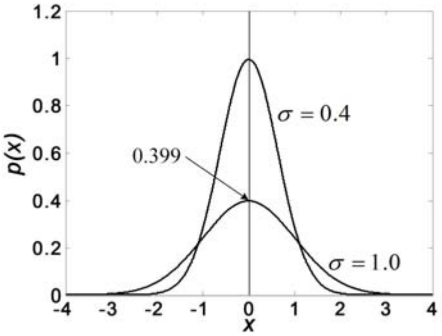

Fig. A.1 Gaussian probability density distribution about zero-mean with various standard deviation, σ=1.0 gives nondimensional presentation.

Rayleigh probability of exceedence

The probability of the peaks exceeding the reference peak *a* is defined in the following form:

$$\Pr\{\text{peaks} \geq a\} = \int_a^\infty p(a)da = \exp\left(-\frac{a^2}{2m_0}\right) \qquad \text{(A-9)}$$

which is called the Rayleigh probability of exceedence, valid for the narrow band Gaussian or linear random process (wave or response motion of structure). Given the variance of a process, one may estimate the probability exceeding the reference peak *a*. The probability that any positive peak value of Gaussian narrow-band process x (t) exceeding $3\sqrt{m_0}$ is 0.011. Another word, on the average about 1 peak in a 100 exceeds $3\sqrt{m_0}$ level.

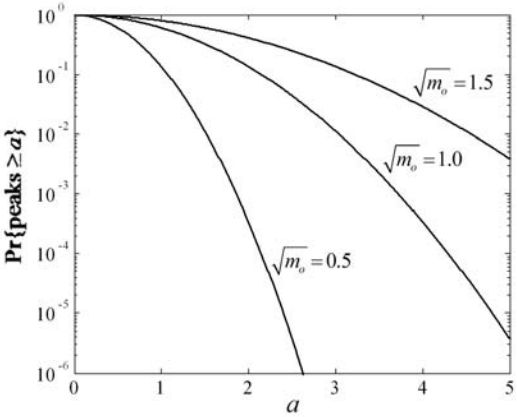

Fig. A.2 Rayleigh probability of exceedence of positive peak *a*

Referring to **Fig. A.2**, *a* illustrates that the peak (crest height) values for a given probability increases with the standard deviation. The curve of unit standard deviation represents the normalized probability by the standard deviation.

Rayleigh probability density of positive peaks

The probability density function of the positive peak *a* is the derivative of the probability of exceedence eq. (A-8) with respect to *a*.

$$p(a) = \frac{a}{m_0}\exp\left(-\frac{a^2}{2m_0}\right) \qquad 0 \leq a \leq \infty \qquad \text{(A-10)}$$

Eq. (A-10) is the *Rayleigh probability density function* of positive peaks of Gaussian narrow-banded process, which is presented in **Fig. A.3**.

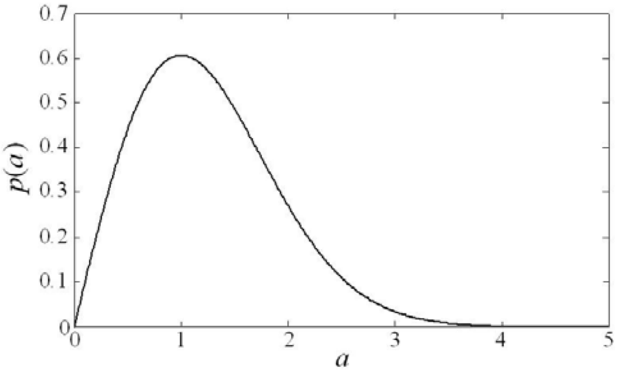

Fig. A.3 Probability density of positive peak

The above probability density function is determined simply knowing the variance or the mean of the process. It can be shown that the maximum value of the probability density is at $a = \sqrt{m_0}$.

APPENDIX B

FOURIER TRANSFORM

Continuous Fourier transform

$$X(f) = \int_{-\infty}^{\infty} x(t) e^{-i2\pi ft} dt$$
$$x(t) = \int_{-\infty}^{\infty} X(f) e^{i2\pi ft} df \qquad \text{(A-11)}$$

Fouruier transform pair in ω- domain:

FT convention A:

$$X(\omega) = \int_{-\infty}^{\infty} x(t) e^{-i\omega t} dt$$
$$x(t) = \frac{1}{2\pi} \int_{-\infty}^{\infty} X(\omega) e^{i\omega t} d\omega \qquad \text{(A-12)}$$

FT convention B:

$$X(\omega) = \frac{1}{2\pi} \int_{-\infty}^{\infty} x(t) e^{-i\omega t} dt$$
$$x(t) = \int_{-\infty}^{\infty} X(\omega) e^{i\omega t} d\omega \qquad \text{(A-13)}$$

Relation between time domain and frequency domain

Fourier transform of convolution of two functions $f_1(x)$ and $f_2(x)$ becomes multiplication of transformed $F_1(\omega)$ and $F_2(\omega)$ in frequency domain.

$$f_1(t) \xrightarrow{fft} F_1(\omega), \; f_2(t) \xrightarrow{fft} F_2(\omega)$$

$$f_1(t) * f_2(t) \xrightarrow{fft} F_1(\omega) \cdot F_2(\omega) \qquad \text{(A-14)}$$

$$f_1(t) \cdot f_2(t) \xrightarrow{fft} \frac{1}{2\pi} F_1(\omega) * F_2(\omega)$$

And Fourier transform of multiplication of two functions $f_1(x)$ and $f_2(x)$ becomes convolution of transformed $F_1(\omega)$ and $F_2(\omega)$ in frequency domain.

APPENDIX C

DIRAC DELTA FUNCTION

Dirac delta function has following properties

$$\delta(x) = 0 \text{ if } x \neq 0$$

$$\int_{-\infty}^{\infty} \delta(x)dx = 1 \qquad \text{(A-15)}$$

$$\int_{-\infty}^{\infty} \delta(x - x_0)s(x)dx = s(x_0)$$

where *x* may be time or frequency in our application.

Definition of Dirac delta functionin time domain

Consider a rectangular impulse (force *A* × time *t* or wave elevation *A* × time *t*):

$$g(t) = \begin{cases} A, & |t| < T/2 \\ 0, & |t| > T/2 \end{cases} \qquad \text{(A-16)}$$

The Fourier transform of impulse *g*(*t*) with convention A gives:

$$G(\omega) = \int_{-\infty}^{\infty} g(t)e^{-i\omega t}dt = AT\frac{\sin\left(\omega\frac{T}{2}\right)}{\omega\frac{T}{2}} \qquad \text{(A-17)}$$

If the area *AT* of the rectangular impulse is kept equal to unity as the breadth of the impulse approaches zero and the height becomes infinite, we will obtain a special unit impulse called Dirac delta function *δ*(*t*). Since

$$G(\omega) = \lim_{T/2\to 0} AT\frac{\sin\left(\frac{\omega T}{2}\right)}{\frac{\omega T}{2}} = 1 \qquad \text{(A-18)}$$

the FT of Dirac delta function *δ*(*t*) is

$$G(\omega) = \int_{-\infty}^{\infty} \delta(t)e^{-i\omega t}dt = 1 \qquad \text{(A-19)}$$

which satisfies the property of Dirac delta function in eq. (A-15). IFT of $G(\omega)$ gives the definition of Dirac delta function $\delta(t)$ in the form

$$\delta(t) = \frac{1}{2\pi}\int_{-\infty}^{\infty} e^{i\omega t}\, d\omega \tag{A-20}$$

If convention B is applied, $G(\omega)=1/2\pi$. However it gives the same definition of Dirac delta function eq. (A-20). The definition of Dirac delta function is independent of the use of conventions A and B.

Definition of Dirac delta function in frequency domain

Consider a sinusoidal wave of amplitude A and frequency ω_n

$$x(t) = Ae^{i\omega_n t} \tag{A-21}$$

Applying the convention B

$$Ae^{i\omega_n t} = \int_{-\infty}^{\infty} X(\omega) e^{i\omega t} d\omega \tag{A-22}$$

If we assume

$$X(\omega) = A\delta(\omega - \omega_n) \tag{A-23}$$

It will satisfy Eq. (A-22). Substituting Eqs. (A-21) and (A-23) in Eq. (A-13), we have

$$\delta(\omega - \omega_n) = \frac{1}{2\pi}\int_{-\infty}^{\infty} e^{-i(\omega-\omega_n)t} dt \tag{A-24}$$

If convention A is applied, we will have the same definition of Dirac delta function Eq. (A-24). The definition of Dirac delta function is independent of the use of conventions A and B.

VITA

Nungsoo Kim, son of Kwang-Ho Kim, was born in Seoul, Korea on October 12, 1970. He graduated from Inha University with a bachelor of science in naval architecture and ocean engineering in February, 1994. He entered the graduate school at Inha University in March, 1996 and received a master of science in mechanical engineering in August, 1997. He entered the graduate program at Texas A&M University in August, 1998 and received a Ph.D. in ocean engineering in December, 2004.

His permanent address is:

Kangnam-gu, Dogok-dong, 963
Youksam Lucky Apt. 102-406
Seoul, Korea, 135-270

E-mail address: nungs@hanmail.net